UNIVERSITY OF COPENHAGEN
FACULTY OF SCIENCE

Optomechanics at the room temperature

Towards classical and quantum applications

PhD thesis

Sampo Saarinen

Advisor: Prof. Albert Schliesser

Submitted: September 30, 2021

This thesis has been submitted to the PhD School of The Faculty of Science, University of Copenhagen

ABSTRACT

The field of optomechanics concerns interaction between mechanical motion and electromagnetic radiation. The interaction allows for exceptionally precise measurement of the motion and control of mechanical motion on the level of a single quantum. In the recent decades, steady progress in fabrication techniques has enabled increasing number of experiments probing fundamental quantum mechanics. On the other hand, the optomechanical interaction promises new applications in force sensing, detection of electromagnetic fields and as a platform for budding quantum networks. In this thesis, we present two room temperature experiments as steps towards such technologies

First, we have developed an integrated opto-electromechanical transducer for use in clinical MRI machines. The device integrates an optical optical cavity and electrodes on a single chip and is fiber coupled. An aluminium membrane forms one half of a parallel plate capacitor and one mirror of a Fabry-Pérot-cavity. The device is connected to a resonant electrical detection circuit and we infer the noise temperature of the transducer device to be 210 K. In a proof of principle experiment, we image an MRI phantom in a commercial 3 T MRI scanner.

Second, we have built an optical cavity consisting of a fiber mirror and a phononic crystal mirror exhibiting low phase noise. Combined with a soft-clamped silicon nitride membrane, the optomechanical system can reach $C_q > 1$. We further feedback cool the resonators mode from room temperature to an occupation of $n = 20$ phonons. The final occupation is limited by poor detection efficiency caused by suboptimal mode matching.

SAMMENFATNING

Forskningsfeltet optomekanik beskæftiger sig med vekselvirkningen mellem mekanisk bevægelse og elektromagnetisk stråling. Denne vekselvirkning tillader exceptionelt nøjagtig måling af bevægelse og kontrol over den mekaniske bevægelse ned til niveauet af enkelte kvanter. Igennem de seneste årtier har støt fremgang i fabrikationsteknikker tilladt flere og flere eksperimenter der tester fundamental kvantefysik. Derudover er den optomekaniske vekselvirkning lovende for anvendelser indenfor kraftsensorer, detektion af elektromagnetiske felter og som en platform for nye kvantenetværk. I denne afhandling præsenterer vi to stue-temperatureksperimenter, som trin på vejen til sådanne teknologier.

For det første har vi udviklet en integreret opto-elektromekanisk transducer til brug i kliniske MRI maskiner. Dette apparat integrerer en optisk kavitet og elektroder på en enkelt chip og er fiberkoblet. En aluminiummembran udgør den ene halvdel af en parallel-plade kapacitor samt et spejl i en Fabry-Pérot kavitet. Dette apparat er forbundet til et resonant elektrisk målekredsløb og vi udleder transducerens støjtemperatur til 210 K. I et princip-bevis eksperiment afbilleder vi en MRI kalibreringsprøve i en kommerciel 3 T MRI scanner.

For det andet har vi bygget en optisk kavitet bestående af et fiberspejl og et fononisk-krystal spejl der besidder lav fasestøj. Kombineret med en blødt fastspændt siliciumnitrid membran, kan det optomekaniske system opnå $C_q > 1$. Vi tilbagekoblingskøler yderligere resonatorens svingning fra stuetemperatur til et gennemsnitligt fononantal på 20. Det endelige fononantal er begrænset af ringe detektionseffektivitet, hvilket skyldes suboptimal tilstandstilpasning.

ACKNOWLEDGEMENTS

After more than four years, I am quite happy to have finished a PhD thesis. The Niels Bohr Institute and the quantum optomechanics lab has been a special place to work at and the journey here was made both possible and much more enjoyable by a number of individuals.

First, I'm very grateful to my wife who moved with me to Copenhagen and without whom life would have been much less meaningful.

I would also like to thank Albert for giving me the opportunity to join his lab, and for being both very knowledgeable and approachable supervisor and of course for having a great eye for talent.

All the people in the group deserve a special mention for being generous with their time and ideas, as do many members of the Quantum photonics lab and members of QUANTOP. I will miss all of you. I would especially like to thank Nenad for the many discussions resolving (and sometimes creating) confusion and crucial assistance with the fiber cavity experiment. I'm also very happy that I had the chance to work on the MRI transducer with Anders.

Finally, taking part in the OMT network has been both educational and good fun mostly due to the other fellows. I hope our paths cross in the future. Antonella Ragnelli deserves a special mention for keeping the network together and running a tight ship!

- *Sensitive optomechanical transduction of electric and magnetic signals to the optical domain* , Anders Simonsen, **Sampo Antero Saarinen**, Juan Diego Sanchez, Jan Henrik Ardenkjær-Larsen, Albert Schliesser, and Eugene Simon Polzik, Optics Express Vol. 27, Issue 13, pp. 18561-18578 (2019)

- *Magnetic resonance imaging with optical preamplification and detection*, A. Simonsen, J. D. Sánchez-Heredia, **S. A. Saarinen**, J. H. Ardenkjær-Larsen, A. Schliesser and E. S. Polzik, Scientific Reports volume 9, Article number: 18173 (2019)

- *Ground State Cooling of an Ultracoherent Electromechanical System*, Yannick Seis, Thibault Capelle, Eric Langman, **Sampo Saarinen**, Eric Planz, Albert Schliesser, arXiv:2107.05552 [quant-ph] (2021)

- *Feedback-cooling a mechanical resonator close to the quantum ground state from room temperature*, **S. A. Saarinen**, N. Kralj, E. C. Langman, Y. Tsaturyan, and A. Schliesser, *In preparation*

CONTENTS

1 INTRODUCTION

RADIATION PRESSURE AND MECHANICAL MOTION

Nowadays optomechanics is starting to be a mature field where simple demonstrations of a platform is no longer sufficient to raise interest. The very core of optomechanics is interaction between light and a mechanical resonator. This interaction is mediated by the radiation pressure force i.e. the fact that despite being massless particles, photons have momentum. As is already a tradition in theses in optomechanics, we would like to first take brief historical look.

The observation that photons apply a force can be traced back to the astronomical records of Johannes Kepler, where he noticed that the tail of a comet points away from the sun and even formulated a hypothesis, that the light of the sun would push the the particles. More accurate measurements, explicitly looking for radiation pressure force predicted by Maxwell's formulation of electromagnetism [1]. were made a the turn of the 20th century by Crooke with a device where a light torsion pendulum was placed in a partial vacuum and a light was shone on one of the arms [2]. However, the first experiment was less than ideal and the motion observed was caused by local pressure change due to temperature gradients. Nevertheless, improved measurements with broadly similar apparatuses were independently made by P.N. Lebedev and Nichols and Hull and the were able to rule out effects other than radiation pressure[3, 4].

While in principle it could be said that these experiments were already a form of optical control of mechanical motion, what we usually have in mind is something finer. One such demonstration of finer control was the invention of optical tweezers where a dielectric particle - later atoms and ions - was trapped using a tightly focused laser beam [5]. Around the same time, it was theoretically and experimentally shown that the radiation pressure force damps or anti-damps the motion of a movable end mirror in a Fabry Perot cavity [6, 7]. Interestingly, such a system also lends itself to an exceptionally accurate measurement of the moving mirrors motion. In fact, modern gravitational wave detectors such as LIGO [8] and the less well known advanced VIRGO [9] consist of two perpendicular multiple kilometre long optical cavities. When the gravitational wave passes, one of the cavities is elongated relative to the other and the length difference is picked up. The position measurement in an optomechanical system is based on the same principle.

OPTOMECHANICS: FROM FUNDAMENTAL SCIENCE TO QUANTUM APPLICATIONS

Advancing nanofabrication techniques enabled engineering ever finer and lighter nanomechanical resonators sensitive to ever smaller forces. Under suitable conditions, measuring the effect of the quantum fluctuations of light, or the so called radiation pressure shot noise, ecame possible [10] and further control of mechanical motion soon followed. Nowadays, preparing a mechanical mechanical at ground state is almost routine and achieved with multiple different configurations [11, 12, 13, 14, 15]. Optomechanical systems have been used to generate squeezed states of light [16], entangling both disparate electromagnetic fields [17, 18], separate mechanical resonators [19, 20] and the field with the mechanical resonator[21]. Most strikingly, the collective degrees of freedom of a very *macroscopic* resonator behave exactly according to a quantum mechanical model. One can imagine pushing for more massive resonators to investigate the quantum to classical transition, investigate state collapse models or measure the effect of gravitation [22, 23].

While many of the phenomena probed in such a system are inherently interesting from the point of view of fundamental quantum mechanics, optomechanics also promises new applications. Low loss mechanical resonators combined with precise position measurement allow for ultralow force sensitivity down to few tens of zeptonewton at moderate cryogenic temperature [24] and a suitably coupled optomechanical device could be used to pick up minute electromagnetic fields. Alternatively, optomechanical systems could provide tools for a budding quantum internet [25]. For this purpose, a tantalizing prospect is converting microwave photons originating from a superconducting qubit to optical photons at telecom wavelengths that are much easier to transport over long distances[1]. Mechanical resonators couple easily to both microwave and optical cavities facilitating such frequency conversion. Recent advances in increasing the mechanical coherence times to ever higher values would also suggest the possibility of using a mechanical element as a quantum memory[27]. Thus, optomechanical devices could play a key role in enabling the budding quantum internet.

1 In fact as of June 2021, there are already startups aiming to commercialize the technology, such as QphoX in Netherlands [26].

The common thread of this thesis is optomechanics at the room temperature. So far, most experiments require a cryogenic environment and a complicated experimental setup. Room temperature operation would not only simplify system design, but enable the use of optomechanical devices in situations, where cooling is impractical or outright impossible. We thus present two experiments demonstrating sufficient performance at the room temperature. First, we have developed an integrated opto-electromechanical transducer that is used in a clinical magnetic resonance imaging scanner to replace the electrical detection circuit. Second, we have built a fiber mirror based cavity and leveraged phononic engineering both in mirrors and in silicon nitride membranes to create a compact, low phase noise optomechanical cavity enabling quantum experiments and cooling to low occupation at the room temperature.

As is the convention, we will start with a theory chapter covering the constituent elements of the optomechanical system and, especially for the following experiments, the most important consequences of the optomechanical interaction. Next, we will cover the integrated transducer where we will focus on the main results since the author joined the project in progress and the development and the results have been covered in detail in a previous thesis[28]. Nevertheless, reading chapter 3 should give an excellent overview on the device and its capabilities.

Finally, we finish with a detailed look at the room temperature quantum experiment that has been the authors main focus in the latter part of the PhD.

2 THEORY

In this chapter we will start with ahoe couple of mathematical conventions and then cover the fundamentals of optomechanics with the focus on aspects necessary to understand the experimental results. As a notational convention throughout this thesis, unless otherwise noted, Greek letters Ω and ω refer to angular frequency. More specifically, capital Ω is reserved for the Fourier frequency and lower case ω typically denotes some frequency of the system.

Much of the discussion will undoubtedly be familiar to many readers. Optomechanics is already starting to be a mature field and there are excellent review articles [29] and even textbooks [30] covering the theoretical model in detail. Nevertheless, the level of detail and the amount of intermediate steps is chosen for completeness sake, to set a consistent notation and to improve the author's understanding. Experienced readers are encouraged to skim, but to some extent, this is also a theory section I would have liked to read when I first started in optomechanics.

2.1 MATHEMATICAL TOOLS

Before diving into the theoretical model in detail, let us introduce two important mathematical tools, the *Fourier transform* and the *power spectral density* (PSD) and define the conventions used in this thesis.

2.1.1 *Fourier transform*

In optomechanics, it is often much more convenient to work in the frequency rather than in the time domain. The link between the domains is of course the Fourier transformation and in this thesis, we use the convention

$$\mathcal{F}[h(t)] = \int h(t)\, e^{i\Omega t} dt, \tag{2.1}$$

where we work with angular frequency $\Omega = 2\pi\nu$. In the following sections, when there is no risk of confusion, we often denote the Fourier transform of a function h simply by replacing time t with frequency Ω, i.e. $\mathcal{F}[h(t)] = h(\Omega)$.

A useful identity for the Fourier transform of a time derivative follows immediately from the definition

$$\mathcal{F}\left[\frac{\partial h(t)}{\partial t}\right] = -i\Omega\mathcal{F}\left[h(t)\right] = -i\Omega h\left(\Omega\right). \tag{2.2}$$

The identity extends to higher derivatives as one would expect

$$\mathcal{F}\left[\frac{\partial^n h(t)}{\partial t^n}\right] = \left(-i\Omega\right)^n h\left(\Omega\right). \tag{2.3}$$

2.1.2 *Power spectral density*

PSD is an important analytical tool, not the least because experimental data is acquired as a spectral density. However, in the theoretical model, we usually solve the equations of motion for the operators of the system in the frequency domain and it is not immediately obvious[1] how to connect the parameter of the system – e.g. position – to the measured spectrum.

It is perhaps easiest to to start by considering a time trace $x(t)$ of the position of a damped driven harmonic oscillator with resonance frequency ω_m. We record the position of the oscillator over time τ such that τ is much longer than any correlation times of the system. The time-gated Fourier transform of such trace is then

$$x(\Omega)_\tau = \frac{1}{\sqrt{\tau}}\int_0^\tau e^{i\Omega t}x(t)\,dt. \tag{2.4}$$

However, the trace $x(t)$ is noisy and if we simply look at the square norm $|x(\Omega)|^2$, we would see a collection of sharp peaks around $\pm\omega_m$. To recover the expected Lorentzian peak, we need to average over many realizations of the trace $x(t)$, looking at $\left\langle|x(\Omega)|^2\right\rangle$ instead. The average norm can then be calculated from the time traces as

$$\left\langle|x(\Omega)|^2\right\rangle = \frac{1}{\tau}\int_0^\tau\int_0^\tau e^{i\Omega(t_1-t_2)}\left\langle x(t_1)x(t_2)\right\rangle dt_1\,dt_2. \tag{2.5}$$

First, the autocorrelation $\langle x(t_1)x(t_2)\rangle$ depends only on the difference between t_1 and t_2. Let us set $t = t_1 - t_2$ and evaluate one of the integrals yielding a factor of τ. We are then left with

$$\left\langle|x(\Omega)|^2\right\rangle = \int_{-\tau}^{\tau} e^{i\Omega t}\left\langle x(t)x(0)\right\rangle dt. \tag{2.6}$$

If the autocorrelation decays in a much shorter time than the integration bounds $\pm\tau$, which we is true for all cases we are interested in this thesis, the integration bounds can be extended to

1 At least to the author.

$\pm\infty$ without introducing significant error. Then, we are left with a Fourier transform of the autocorrelation function. This is the essence of the Wiener-Khinchin theorem connecting the Fourier transform of an autocorrelation function to the power spectral density of said function. Now we have a relatively straightforward way of connecting the solutions of the equations of motion to the measured spectrum. Given the solutions and knowledge of their correlators, it takes only a few algebraic manipulations to find the theoretical power spectral density which is fitted to the measurement data.

For quantum mechanical operators, a bit more care needs to be taken to account for noncommutation. Thus, for an operator $\hat{A}$ and it's frequency domain autocorrelation, the power spectral density is simply

$$S_{AA}(\Omega) = \int_{-\infty}^{\infty} \left\langle \hat{A}^{\dagger}(\Omega')\hat{A}(\Omega) \right\rangle \frac{d\Omega'}{2\pi}. \tag{2.7}$$

It should be noted, that we can also consider *cross spectra densities* S_{AB} with direct substitution of operators.

To make a final remark before moving on, in the experiments we consider *ergodic*[2] systems, essentially meaning that *ensemble* and *time* averages are the same. The consequence is that instead of one impractically long time trace we can acquire multiple shorter ones and average over them, making experiments much more feasible.

2.2 QUALITATIVE PICTURE OF THE OPTOMECHANICAL INTERACTION

Before treating the subject matter with formal mathematics, it is illustrative to consider a conceptual sketch. In the canonical optomechanical scheme, we consider a Fabry-Pérot cavity consisting of two mirrors facing each other. One of the mirrors is free to move but subject to a harmonic potential and as such the cavity length changes as the mirror oscillates while the other is taken to be stationary, as shown in figure 2.1.

Such cavity supports standing waves if the cavity length equals an integer number of half-wavelengths. Each such wavelength λ_n corresponds to a resonance frequency of the cavity. If the cavity is pumped with a laser at one such wavelength,

2 An illustrative example about the difference between ergodic and **non**-ergodic processes comes from Nicholas Nassim Taleb [31]. It's a different thing to have one hundred players play one round of roulette than for one person to play a hundred rounds. In the latter case, the player can go bust and cannot continue playing! Thus ensemble and time averages are not the same and the situation is not ergodic.

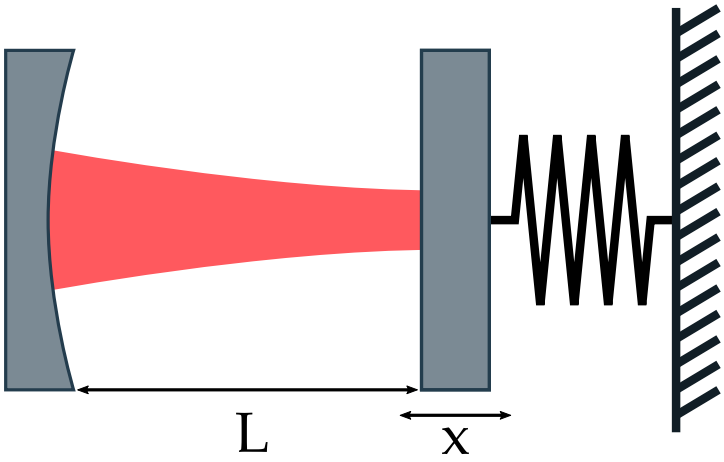

Figure 2.1: The canonical optomechanical system consists of a Fabry-Pèrot cavity where one end mirror is free to move in a harmonic potential, for example we can imagine it is connected to a spring. The resonance frequency depends on the cavity length and thus, the movement of the mirror changes the resonance condition. On the other hand, the intracavity field applies a radiation pressure force on the mirrors and thus changes it's position.

it builds intensity. The magnitude of the intracavity intensity depends on how closely the pump laser frequency matches the resonance frequency of the cavity. Away from resonance, the intracavity field's intensity is reduced.

This formulation already points to the mechanism of the optomechanical interaction - if the cavity length changes, the resonance condition also changes correspondingly. Further, when the cavity field leaves the cavity, this output field then carries information about the length fluctuations allowing very accurate position measurement on the motion of the movable mirror. In fact, this kind of interferometric measurement is the basis of gravitational wave detectors where the passing of the gravitational wave changes the length of a very long optical cavity.

However, photons have momentum and to preserve momentum, when they reflect off the mirror, they apply a 'kick' on it. This force is proportional to the number of photons or, in other words, the intensity of the light beam, in this case, the magnitude of the intracavity field. The light inside the cavity then moves the mirror. This in turn changes the cavity length and thus the resonance condition. Since the pump laser is at a constant wavelength, the changing resonance condition causes the magnitude of the intracavity field to change and thus the force on the mirror changes, changing the length of the cavity again. This interplay between the mirror's motion and the optical resonator is the very core of optomechanics.

Given suitable experimental conditions, such a system can be used to control mechanical motion by preparing a nanomechanical resonator in it's quantum ground state [14, 12, 13], entangling different optical [18] or microwave fields[17] or even distinct mechanical resonators [19]. Given the recent advances in superconducting quantum computing, a particularly timely application is the promise of quantum transduction between microwave qubits and telecom wavelength photons allowing for long distance quantum networks. This kind of frequency conversion is widely investigated with different systems, such as metallized membrane resonators [32, 33], optomechanical crystal resonators coupled to a photonic crystal cavity [34, 35, 36, 37] or whispering gallery mode resonators [38, 39].

With the appetizers out of the way, let us then move on to take deeper look at the optomechanical formalism. Before formalizing the interaction, let us start with the individual ingredients, optical and mechanical resonators.

2.3 OPTICAL RESONATORS

Let us again start by considering a Fabry-Pérot cavity. There are many other geometries for optical resonators, such as photonic crystal cavities or whispering gallery resonators, all of which can be used in optomechanical experiments. Hoever, the venerable Fabry-Pérot configuration is perhaps the most illustrative one and the theory worked out for it describes equally well all the other geometries, some of which are shown in figure 2.2. Most importantly, in this thesis, we employ exclusively Fabry-Pérot cavities.

As already seen in figure 2.1, a Fabry-Pèrot cavity consists of two partially reflective mirrors separated by length L. Such a cavity hosts an infinite number of modes where the cavity length equals an integer number of half-wavelenghts, $L = n\lambda_n/2$, or equivalently, the cavity hosts optical resonances at frequencies

$$\omega_{c,n} = \frac{\pi c n}{L}, \tag{2.8}$$

where $\omega_{c,n}$ is the cavity resonance frequency and c is the speed of light in the chosen medium, in this case, vacuum.

The separation between two optical modes is called the *free spectral range* (FSR)

$$\Delta\omega_{FSR} = \omega_{c,n+1} - \omega_{c,n} = \frac{\pi c}{L}. \tag{2.9}$$

Typically, we consider situations where only one optical mode is relevant and in the following discussion, when referring to

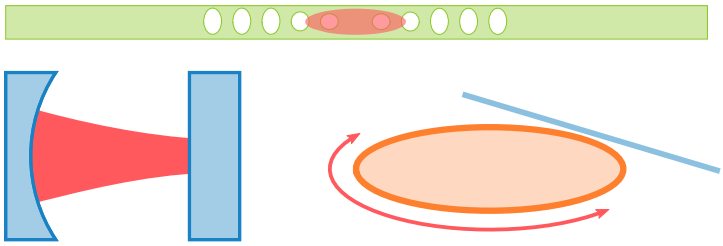

Figure 2.2: Various geometries for optical cavities, each of which can be used in optomechanical experiments. Clockwise from the top: First, the photonic crystal pattern reflects photons in a photonic waveguide creating a cavity. The resonator can be fabricated such that the breathing modes of the beam change the optical resonance frequency. Second, a disc of suitable material supports optical whispering gallery modes. The disc cavity is typically evanescently coupled to a tapered optical fiber. The disc vibrations change the optical path length leading to optical frequency change. Finally, on bottom left, the Fabry-Pérot cavity, where the resonance frequency is determined by the mirror separation. The mirror movement then changes the cavity length and thus the optical frequency.

the optical cavity frequency, we simply write ω_c, dropping the subscript n. In practice, this means, that the FSR should be sufficiently large compared to the linewidth of the resonance, such that there is no interaction between the modes. This is usually the case for the cavities employed in optomechanics.

The cavity mirrors are partially reflective. It is both impossible and experimentally undesirable to have perfectly reflective mirrors - there are always imperfections in the substrates. More importantly without partially transmissive mirrors, there would be no way to access the intracavity field and thus nothing to measure. Each photon is then only confined in the cavity for a finite time, τ_c. However, it is more commonplace to consider its inverse, the decay rate $\kappa = \tau_c^{-1}$. It should be noted, that κ contains all loss channels of the cavity. We typically divide it between input-output loss rates of the mirrors, κ_1 and κ_2 for the cavity mirrors, or κ_R and κ_L for right and left mirrors respectively if we wish to emphasize the spatial ordering of the mirrors. Additionally, we denote the internal loss rate κ_{int} containing channels such as absorption or the photon scattering out of the cavity due to misalignment. Even though we call them loss rates, only photons decaying through κ_{int} are truly lost whereas light leaving the cavity through the measurement ports, in other words the mirrors of the cavity, can be directed to a measurement apparatus and the information is recovered.

Instead of treating the electrical fields themselves, we will consider the evolution of the complex field amplitude $a(t)$. It is

perhaps less intuitive than amplitude and phase of the field, but it is convenient for mathematical treatment and quantization. Its square norm corresponds to the number of photons inside the cavity $|a(t)|^2 = n_{cav}$ and its time evolution is determined by the equation of motion

$$\dot{a}(t) = \left(-\frac{\kappa}{2} - i\omega_c\right) a(t) + \sqrt{\kappa_{in}} a_{in}, \tag{2.10}$$

where we have introduced the driving field a_{in} reaching the cavity through the input port with decay rate κ_{in}. Here, and throughout the thesis, unless it would lead to unclear typography, we have used the 'dot notation' for time derivatives

$$\dot{a}(t) = \frac{da(t)}{dt}. \tag{2.11}$$

The driving field is taken to be a coherent field oscillating at frequency ω_L. Even though we are using terms such as 'optical' or 'laser', most of the discussion is equally valid for electrical resonators. The resonance condition and the cavity field $a(t)$ are defined differently, but the equations of motion are similar.

It is convenient to transform to coordinates oscillating at the drive frequency where the cavity frequency is replaced with detuning $\Delta = \omega_L - \omega_c$ and the equation of motion becomes

$$\dot{a}(t) = \left(-\frac{\kappa}{2} + i\Delta\right) a(t) + \sqrt{\kappa_{in}} \bar{a}_{in}. \tag{2.12}$$

Now the driving field is a constant $\bar{a}_{in}$. We can immediately obtain the steady state solution by setting $\dot{a}(t) = 0$

$$\bar{a}_c = \frac{\sqrt{\kappa_{in}} a_{in}}{\frac{\kappa}{2} - i\Delta}. \tag{2.13}$$

The cavity field amplitude $|\bar{a}_c|^2$ follows a Lorentzian function centred at zero detuning i.e. the point where the drive frequency coincides with the cavity resonance frequency with a maximum value $|\bar{a}_c|^2_{\Delta=0} = 4\kappa_{in}|\bar{a}_{in}|^2/\kappa^2$. When crossing the resonance, the phase of the cavity field shifts by π as seen in figure 2.8.

As mentioned, the cavity field is not directly accessible to measurement, we can only detect light leaving the cavity through the mirrors. In other words, we must either measure the reflected or transmitted light. In the following discussion, we take the cavity to have two ports, left and right with decay rates κ_L and κ_R. The cavity is driven through the left port and that is also the reflection port.

The transmitted light simply consists of the cavity light decaying trough the right port

$$a_T(t) = \sqrt{\kappa_R} a_c(t). \tag{2.14}$$

For the reflected light, the situation is slightly more complicated. The cavity reflection consists of two parts. There is the light from the cavity, but part of the driving beam is also immediately reflected without even entering the cavity, the so called *promptly reflected beam*. On reflection this promptly reflected beam picks up a phase factor $e^{i\pi}$ and thus the total reflected field in the steady state is

$$a_{\text{refl}}(t) = a_{\text{in}}(t)e^{i\pi} + \sqrt{\kappa_R}a_c(t). \tag{2.15}$$

We may substitute in the steady state solution to find

$$\bar{a}_{\text{refl}} = -\bar{a}_{\text{in}} + \frac{\kappa_R \bar{a}_{\text{in}}}{\frac{\kappa}{2} - i\Delta} \tag{2.16}$$

$$= -\left(1 - \frac{\kappa_L}{\frac{\kappa}{2} - i\Delta}\right)\bar{a}_{\text{in}}. \tag{2.17}$$

There are a few remarks to be made. First, under suitable conditions, namely when $\kappa_L = \kappa/2$, the cavity reflection vanishes completely on resonance! In such case, the cavity is said to be *critically coupled*. If the coupling is less than half of the total loss rate, the cavity is said to be *undercoupled* and conversely overcoupled when $\kappa_R > \kappa/2$. It should be noted that 'coupling regime' is determined only for the port in question and it is common that the cavity is undercoupled on one port and overcoupled on another[3].

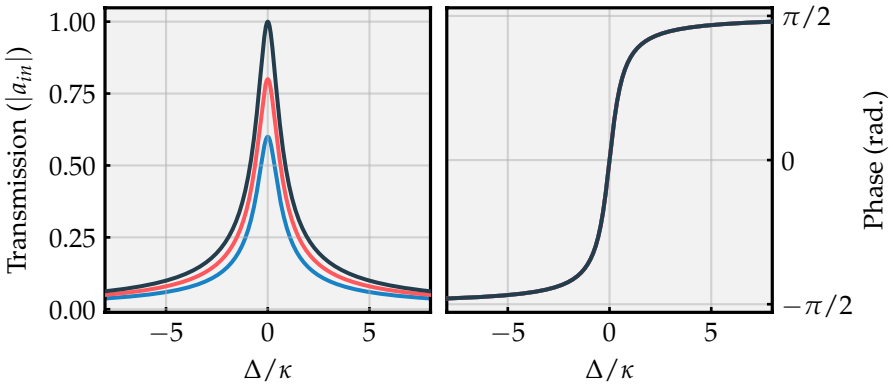

Figure 2.3: The amplitude $|a|$ and phase $a/|a|$ of the cavity transmission with output coupling 0.5κ, 0.2κ and 0.1κ from tallest to lowest amplitude. The transmitted phase response is the same for all output couplings. The

It should be noted that the coupling regime of a cavity cannot be distinguished from a simple measurement of reflected

3 A mathematical necessity unless the loss channels are large.

amplitude – both undercoupled and overcoupled cavities have similar reflected amplitudes. To characterize a cavity without prior knowledge of the relative reflectivities of the the mirrors, we would need to measure both the amplitude and the phase of the reflected beam and reconstruct the resonance in the complex plane. In figure 2.4 we have plotted the reflected power with different cavity outcouplings and the corresponding complex plane representations. In practice, it is much preferred to just know the relative magnitude of the mirror transmissivities such that one knows which port is over- or undercoupled.

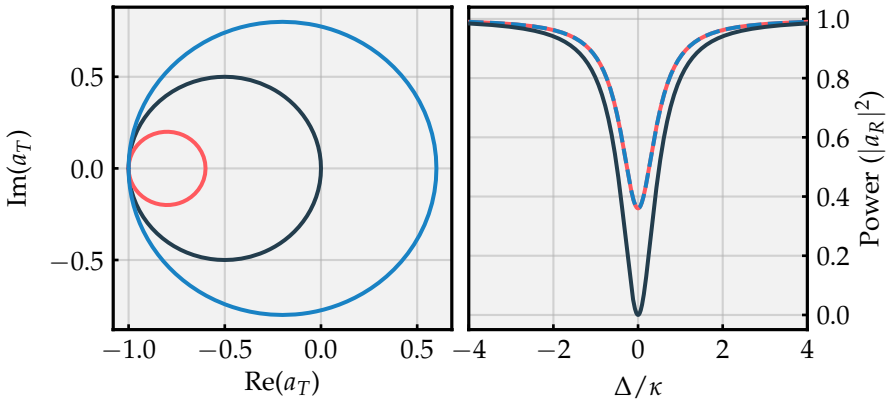

Figure 2.4: The reflected power $|a_R|^2$ and complex plane response of the resonance. The outcoupling is, 0.2κ for the red line, 0.5κ for the grey and 0.8κ for the blue one. When measuring only the reflected power, the under- and overcoupled cavities coincide, but in the imaginary plane, they are very clearly distinct.

As a final remark, we often define coupling efficiency for each port of interest $\eta_{c,i} = \kappa_i/\kappa$ such that $\kappa_i = \eta_{c,i}\kappa$.

2.3.1 *Electrical resonators*

In anticipation of later sections, let us briefly discuss electrical resonators. An electrical circuit consisting of an inductor with inductance L and a capacitor with capacitance C exhibits similar resonance behaviour as the optical cavities presented above. Current I and voltage V in the circuit follow equations of motion $V(t) = L\dot{I}(t)$ and $I(t) = -C\dot{V}(t)$ yielding

$$\ddot{V}(t) = -\frac{1}{LC}V(t)^2. \tag{2.18}$$

If we identify $1/\sqrt{LC}$ as the resonance frequency ω_{LC}, the above equation more clearly describes a harmonic oscillator. We can

use a complex amplitude similar to the optical resonators

$$a(t) = \sqrt{\frac{C}{2V(t)}} + i\sqrt{\frac{L}{2I(t)}}, \tag{2.19}$$

and introduce dissipation to recover the same equation of motion as for the optical cavity and the analysis above remains unchanged.

One approach to facilitate the electromechanical interaction is to make a mechanically compliant capacitor such that displacement modifies the circuit's capacitance. A typical approach would be to either create a fully metallic resonator or functionalize otherwise non-conducting resonator with a conducting layer and use such resonator as one half of a parallel plate capacitor. Less common, but nevertheless possible approach is to instead mediate the coupling via inductance [40].

2.4 MECHANICAL RESONATORS

The second half of an optomechanical system is the mechanical resonator. Let us start by considering the prototypical one dimensional classical harmonic oscillator, a mass on a spring. In fact, even for complicated experimental geometries, there is no need to deviate from the simple model. In most cases, mapping the motional degrees of freedom to one dimension is a relatively straightforward task. The 1D equation of motion is

$$m\ddot{x} = -kx, \tag{2.20}$$

where x is the position, m the mass of the oscillator and k the spring constant. The solution is $x(t) = x_0 \cos(\omega_m t)$, where x_0 is the amplitude of oscillation and $\omega_m = \sqrt{k/m}$ the natural frequency of the oscillator.

However, real oscillators are coupled to the environment and thus lose or gain energy until they are at equilibrium. In the classical 'everyday' regime, thermal fluctuations of mechanical resonators are negligible, and it is quite reasonable to use the word 'decay'[4].

Introducing the mechanical decay rate Γ_m, the resonator's equation of motion becomes

$$m\ddot{x}(t) + m\Gamma_m\dot{x}(t) + m\omega_m^2 x(t) = F(t), \tag{2.21}$$

where we have included any forces affecting the resonator as $F(t)$.

4 However, a low energy quantum state in contact with the environment is heated out to a high energy classical state with a speed proportional to Γ_m.

Assuming that the damping rate is small, specifically $2\Gamma_m < \omega_m$[5], and that there are no forces acting on the resonator, the solution is

$$x(t) = x_0 \exp\left[-\frac{\Gamma_m t}{2}\right] \cos\left(t\omega_m \sqrt{1 - \frac{\Gamma_m^2}{4\omega_m}}\right). \tag{2.22}$$

The solution still oscillates between $\pm x_0$ but now the amplitude decays exponentially in time, or it is also said that the resonator rings down, as seen in figure 2.5. Exiting the resonator to a large amplitude and observing the decay is a very straightforward way to characterize the decay rate of nanomechanical resonators. For particularly low decay rates, the ringdown can last many minutes even at megahertz frequencies.

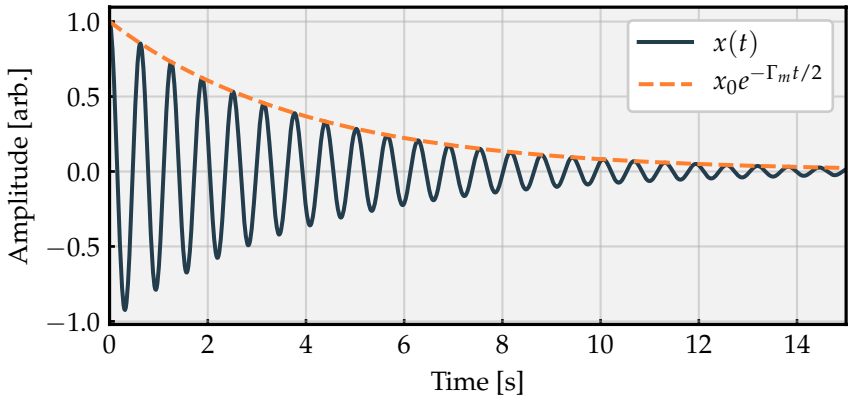

Figure 2.5: The decay of a damped harmonic oscillator with parameters $\Gamma_m = 0.5$ and $\omega_m = 10$.

Instead of decay rates, it is also common to use the mechanical quality factor, a dimensionless quantity defined as $Q = \omega_m/\Gamma_m$[6]. The Q-factor can be interpreted as the number of oscillations the resonator undergoes before losing a fraction $1/e$ of its energy.

Even in the everyday regime, we are often interested in what is the resonator's response to a driving force. For small and light nanomechanical resonators, especially when we want to consider quantum mechanical effects, the thermal force from the environment is significant. For an unspecified force, the

5 This limit is very reasonable for typical, high quality nanomechanical resonators. They often feature megahertz or higher frequencies and the damping rates are often much less than one hertz.

6 If we wish to emphasize that the quality factor is for a mechanical resonator, we can add subscript m, but this is exceedingly rare. Thus, whenever Q is seen in the thesis, it should be understood to refer to the mechanical quality factor.

solution is most easily found in the frequency domain. Fourier transforming equation 2.21, we find

$$-\Omega^2 x(\Omega) - i\Omega\Gamma_m x(\Omega) + \omega_m^2 x(\Omega) = \frac{F(\Omega)}{m}, \tag{2.23}$$

where we have used properties of the Fourier transform for derivatives (see eq. 2.3). After a few algebraic steps, the solution is found to be

$$x(\Omega) = \frac{1}{m\,(\omega_m^2 - \Omega^2 - i\Omega\Gamma_m)} F(\Omega) = \chi_m(\Omega) F(\Omega), \tag{2.24}$$

where we have defined the *mechanical susceptibility* $\chi_m(\Omega)$. As a consistency check, we see that if Ω is very small, $\chi_m(\Omega \approx 0) \approx 1/(m\omega_m^2) = 1/k$, i.e. we have recovered Hooke's law.

Transforming back to time domain is quite frankly rather tedious, especially for the general case. However, we will make a qualitative remark regarding an a drive oscillating at frequency ω_D such that the driving force is $F = F_0 \cos(\omega_D t)$. Previously, we saw that without any forces acting on it, the resonator loses energy and the amplitude decays exponentially. Naturally, we would be curious to know, how the oscillator responds to a drive. Indeed,the oscillator gains energy and there is a corresponding 'ring-up' time before the steady state – i.e. oscillation at the drive frequency – is reached. However, the behaviour in the transient regime can differ greatly depending on how the drive frequency is chosen. So called on resonance driving, that is $\omega_D = \omega_m$ results in an exponential buildud. Far away from the resonance, where the response is proportional to $(\omega_m^2 - \omega_D)^{-2}$, the resulting oscillations are modest.

As already hinted, any real system is always coupled to the environment and is subject to a thermal Brownian force. While this force is often small in magnitude, it is enough to drive a resonator all the from the quantum regime to a high energy state, where the behaviour is fully classical. Recalling the definitions for power spectral densities, the displacement power spectrum of a thermally driven resonator is

$$S_{xx}(\Omega) = |\chi_m(\Omega)|^2 S_{F_{th}F_{th}}(\Omega), \tag{2.25}$$

where we have introduced the PSD of the thermal force $S_{F_{th}F_{th}}$. Knowing the temperature of the environment T and parameters of the resonator, it can be calculated via the *fluctuation-dissipation theorem*

$$S_{F_{th}F_{th}} = 4k_B T \Gamma_m m, \tag{2.26}$$

where k_B is the Boltzmann constant. Given that the *incoherent* thermal force prevents experiments from realizing quantum

experiments, even at cryogenic experiments, it is very desirable to minimize it in favour of coherent interactions. The formula tells us which parameters are of importance. We should engineer devices with mass and dissipation both as low as possible.

The thermal force is spectrally flat, in other words, constant over all frequencies. The spectral shape of the displacement PSD is then solely determined by the square norm of the mechanical susceptibility

$$|\chi_m(\Omega)|^2 = \frac{1}{m\left(\left(\omega_m^2 - \Omega^2\right)^2 + \Omega^2\Gamma_m^2\right)}. \tag{2.27}$$

The response of the resonator is very sharply centred around the natural frequency of the resonator. It makes very good sense to call this frequency the *resonant frequency* of the resonator and that is indeed what we will do in the rest of this thesis.

If the quality factor is high, that is the damping rate is very small compared to the resonant frequency ω_m and we are only interested in the area near the resonance – as is the case for most optomechanical experiments – we can simplify the equation above somewhat

$$|\chi_m(\Omega)|^2 \approx \frac{1}{4\omega_m^2 m}\frac{1}{\left(\omega_m - \Omega\right)^2 + \left(\Gamma_m/2\right)^2}. \tag{2.28}$$

We have approximated $\Omega \approx \omega_m$ such that $\omega_m^2 - \Omega^2 = (\omega_m - \Omega)(\omega_m + \Omega) \approx (\omega_m - \Omega)(2\omega_m)$. The approximated square norm is then a Lorentzian function centred at ω_m with a full width half maximum (FWHM) Γ_m. Besides a ringdown measurement, simply fitting a measured spectrum with the square norm is a simple way to characterize the dissipation of a particular resonator device. However, for very low dissipation rates, that can be as low as millihertz, the resolution bandwidth of the spectrum analyser is typically not sufficient to resolve the peak and hence, the Lorentzian fit is unlikely to yield an accurate result.

A further feature to note is that the integral over the the mechanical spectral density equals the mean square displacement

$$\left\langle x^2 \right\rangle = \int S_{xx}(\Omega)\frac{d\Omega}{2\pi}. \tag{2.29}$$

The mean square displacement can also be calculated via the equipartition theorem

$$\left\langle x^2 \right\rangle = \frac{k_B T}{m\omega_m^2}. \tag{2.30}$$

Therefore, the area under the Lorentzian peak is connected to the temperature – or equivalently the energy – of the resonator.

Then, given a displacement spectrum and knowledge of the temperature, the (effective) mass of the resonator can be determined. Alternatively, and more commonly, since the resonator device's parameters are usually well known, the area can be used to calibrate spectrum from arbitrary units, in practice often (Volts)^2 or dBm, to displacement units.

We can also imagine a resonator coupled to two – or more! – thermal baths, with temperatures T_1 and T_2, each applying thermal Brownian force with dissipation rate γ_i. We can then define an effective temperature

$$T_{eff} = \frac{\gamma_1 T_1 + \gamma_2 T_2}{\gamma_1 + \gamma_2}. \tag{2.31}$$

We can further imagine, that one of these baths is an optical field that can be taken to be at almost zero temperature. Setting $T_1 = T_{env} \equiv T$, $\gamma_1 = \Gamma_m$, $T_2 = T_{opt} \approx 0$ and $\gamma_2 = \Gamma_{opt}$, and the effective temperature becomes

$$T_{eff} = \frac{\Gamma_m T}{\Gamma_m + \Gamma_{opt}}. \tag{2.32}$$

In other words, by tuning the dissipation to optical bath, we can cool the temperature of the mechanical resonator!

2.5 OPTOMECHANICAL INTERACTION

With the constituent systems introduced, it is time to take a formal look at the optomechanical interaction. First, let us remind ourselves of equation 2.8

$$\omega_c(x) = \frac{c\pi n}{L + x}, \tag{2.33}$$

where we have written the length of the optical cavity as $L + x$, where L is the equilibrium cavity length and x the displacement of the mechanical resonator, in this case, the movable end mirror.

As show in figure 2.6, a change in displacement shift the resonance frequency. The motion of the mechanical resonator is very small and we can expand the equation above to first order

$$\omega_c(x) \approx \omega_c(x = 0) + \frac{\partial \omega_c(x)}{\partial x} x \tag{2.34}$$

$$= \omega_{c,0} - Gx, \tag{2.35}$$

where we have identified the unperturbed cavity resonance frequency $\omega_{c,0}$ and, more importantly, the *optomechanical coupling rate* $G = -\partial\omega_c(x)/\partial x$. Its units are frequency over displacement

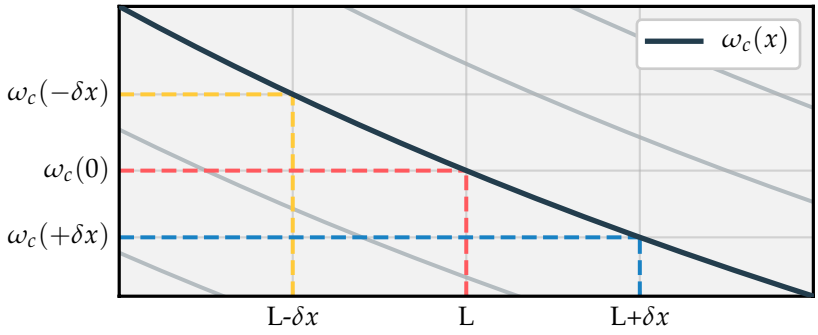

Figure 2.6: The resonance frequency of the optical cavity shifts as the cavity length changes. We have chosen a convention, where positive δx increases the cavity length and thus decreases the resonance frequency. The thinner, gray lines correspond to adjacent resonances one (or more) FSR away.

and it determines how much the cavity frequency shifts per unit of displacement. The equation of motion for the field amplitude 2.10 is also modified

$$\dot{a}(t) = \left(-\frac{\kappa}{2} - i(\omega_{c,0} - Gx)\right) a(t) + \sqrt{\kappa_L} a_{in}, \tag{2.36}$$

where we have replaced the cavity resonance frequency with equation 2.35 and we have chosen the convention where the cavity is driven via the left mirror with decay rate κ_L. The introduction of the optomechanical coupling does not change the dynamics of the cavity much by itself. However, the field inside the cavity applies a radiation pressure force, $F_{rad} = -\hbar G|a(t)|^2$ to the mechanical resonator. The equation of motion for the mechanical resonator is then

$$\ddot{x}(t) + \Gamma_m \dot{x}(t) + \omega_m^2 x(t) = \frac{1}{m}\left(F_{rad} + F_{th}\right). \tag{2.37}$$

Thus, we have two coupled equations of motion

$$\dot{a}(t) = \left(-\frac{\kappa}{2} - i(\omega_{c,0} - Gx(t))\right) a(t) + \sqrt{\kappa_L} a_{in}, \tag{2.38}$$

$$\ddot{x}(t) + \Gamma_m \dot{x}(t) + \omega_m^2 x(t) = \frac{1}{m}\left(-\hbar G|a(t)|^2 + F_{th}\right). \tag{2.39}$$

The pair of differential equations is difficult to solve exactly. Fortunately, in most situations, we can linearize them around small displacement and field fluctuations and solve the simpler, linear pair of equations. The steady state solution, however, is straightforward to find. We set the time derivatives to zero and note that the average of the thermal force is also zero. We thus

find the steady state solution

$$\bar{a} = \frac{\sqrt{\kappa_L}\bar{a}_{in}}{-\frac{\kappa}{2} - i(\omega_{c,0} - G\bar{x})}, \tag{2.40}$$

$$\bar{x} = -\frac{\hbar G|\bar{a}|^2}{\omega_m^2 m}. \tag{2.41}$$

Interestingly, the steady state equations already allow for multiple solutions – a consequence of the optomechanical interaction!

2.5.1 *Dynamical backaction*

While the static bistability is already an optomechanical effect, the more interesting consequence is the so called dynamical backaction, that allows for control of mechanical motion. We begin by linearizing the equations. To that end, we consider small fluctuations around the steady state values

$$x(t) = \bar{x} + \delta x(t) \tag{2.42}$$

$$a(t) = \bar{a} + \delta a(t). \tag{2.43}$$

The fluctuations $\delta x(t)$ and $\delta a(t)$ are small such that any terms proportional to their higher powers are neglected. The steady state part cancels out and we are left with the equations of motion for only the fluctuations

$$\dot{\delta a}(t) = \left(-\frac{\kappa}{2} + i\Delta\right)\delta a(t) - iG\delta x(t)\bar{a} + \sqrt{\kappa_L}\delta a_{in}, \tag{2.44}$$

$$\ddot{\delta x}(t) + \Gamma_m\dot{\delta x}(t) + \omega_m^2\delta x(t) = -\frac{\hbar G|\bar{a} + \delta a(t)|^2 + \delta F}{m}, \tag{2.45}$$

where we have neglected second order terms $\delta x(t)\delta a(t)$ as small. We have also included fluctuations of the input field δa_{in} and those of the thermal force δF. Fort the most parts, equations are straightforward, but the radiation pressure force term requires a little more care. We can choose the steady state field $\bar{a}$ to be real and expand the complex norm

$$|\bar{a} + \delta a(t)|^2 = \bar{a}^2 + \bar{a}\delta a(t) + \bar{a}\delta a^*(t) + \delta a\delta a^*. \tag{2.46}$$

Here $\bar{a}$ only results in static displacement and does not affect the dynamics, $\delta a\delta a^*$ is small and thus neglected, but the complex conjugate $\delta a^*(t)$ needs its own equation of motion when solving the equations via Fourier Transform. To find the correct equation, we can take advantage of a property of Fourier transform

$$h^*(\Omega) = (h(-\Omega))^*. \tag{2.47}$$

To start, we Fourier transform the equation of motion for δa

$$-i\Omega\delta a(\Omega) = \left(-\frac{\kappa}{2} + i\Delta\right)\delta a(\Omega) - iG\bar{a}\delta x(\Omega), \tag{2.48}$$

and take the complex conjugate

$$i\Omega(\delta a(\Omega))^* = \left(-\frac{\kappa}{2} - i\Delta\right)(\delta a(\Omega))^* + iG\bar{a}\delta x(\Omega) \tag{2.49}$$

$$i\Omega\delta a^*(-\Omega) = \left(-\frac{\kappa}{2} - i\Delta\right)\delta a^*(-\Omega) + iG\bar{a}\delta x(-\Omega). \tag{2.50}$$

Given that δx is real, $\delta x(-\Omega) = \delta x(\Omega)$ and as a final step, we set $\Omega \to -\Omega$ to get

$$-i\Omega\delta a^*(\Omega) = \left(-\frac{\kappa}{2} - i\Delta\right)\delta a^*(\Omega) + iG\bar{a}\delta x(\Omega). \tag{2.51}$$

With the equations of motion in the frequency space, we solve for $\delta a(\Omega)$ and $\delta a^*(\Omega)$

$$\delta a(\Omega) = \frac{-iG\bar{a}\delta x(\Omega)}{-i(\Delta+\Omega) + \frac{\kappa}{2}}, \tag{2.52}$$

$$\delta a^*(\Omega) = \frac{+iG\bar{a}\delta x(\Omega)}{i(\Delta-\Omega) + \frac{\kappa}{2}}. \tag{2.53}$$

To simplify the notation, we introduce the cavity susceptibility χ_c

$$\chi_c(\Omega) = \left[\frac{\kappa}{2} - i(\Delta+\Omega)\right]^{-1}, \tag{2.54}$$

such that the solutions can be written as

$$\delta a(\Omega) = -i\chi_c(\Omega)\, G\bar{a}\delta x(\Omega) \tag{2.55}$$

$$\delta a^*(\Omega) = +i\chi_c^*(-\Omega)\, G\bar{a}\delta x(\Omega). \tag{2.56}$$

Similarly, the solution for δx is found in frequency domain

$$-\Omega^2\delta x(\Omega) - i\Omega\Gamma_m\delta x(\Omega) + \omega_m^2\delta x(\Omega) = -\frac{\hbar G\bar{a}}{m}(\delta a(\Omega) + \delta a^*(\Omega)) + \frac{\delta F(\Omega)}{m} \tag{2.57}$$

Substituting in $\delta a(\Omega)$ and $\delta a^*(\Omega)$, we find

$$-\Omega^2\delta x(\Omega) - i\Omega\Gamma_m\delta x(\Omega) + \omega_m^2\delta x(\Omega) = i\frac{\hbar G^2\bar{a}^2}{m}(\chi_c(\Omega) - \chi_c^*(-\Omega))\,\delta x(\Omega) + \frac{\delta F}{m} \tag{2.58}$$

Solving the above for δx

$$\delta x(\Omega) = \frac{\delta F(\Omega)}{m(\omega_m^2 - \Omega^2 - i\Omega\Gamma_m - i\Sigma(\Omega))}, \tag{2.59}$$

where we have defined

$$\Sigma(\Omega) = \frac{\hbar G^2 \bar{a}^2}{m} \left[\chi_c(\Omega) - \chi_c^*(\Omega)\right]. \tag{2.60}$$

The solution resembles the one found for driven harmonic oscillator (cf. equation 2.24), but with an extra term proportional to the optomechanical frequency pull factor G. The optomechanical interaction thus changes both the resonance frequency and the dissipation rate of the mechanical resonator such that $i\Sigma(\Omega) = k_{ba}(\Omega) + i\gamma_{ba}$ where k_{ba} is the optomechanical frequency shift and γ_{ba} the optical spring effect such that

$$k_{ba}(\Omega) = \frac{\hbar G^2 \bar{a}^2}{m} \left(\frac{\Omega - \Delta}{\left(\frac{\kappa}{2}\right)^2 + (\Omega - \Delta)^2} - \frac{\Omega + \Delta}{\left(\frac{\kappa}{2}\right)^2 + (\Omega + \Delta)^2} \right), \tag{2.61}$$

$$\gamma_{ba}(\Omega) = \frac{\hbar G^2 \bar{a}^2}{m} \left(\frac{\kappa/2}{\left(\frac{\kappa}{2}\right)^2 + (\Omega + \Delta)^2} - \frac{\kappa/2}{\left(\frac{\kappa}{2}\right)^2 + (\Omega - \Delta)^2} \right). \tag{2.62}$$

The frequency shift and the optical spring are shown as function of detuning in figure 2.7. With these definitions[7], the *effective mechanical susceptibility* χ_{eff} can be written as

$$\chi_{eff}(\Omega) = \left[m \left(\omega_m^2 - k_{ba}(\Omega) - \Omega^2 - i\Omega \left(\Gamma_m + \frac{\gamma_{ba}(\Omega)}{\Omega} \right) \right) \right]^{-1}. \tag{2.63}$$

In this formulation the shift in resonance frequency and in mechanical linewidth is explicit.

Interestingly, the sign and magnitude of the dynamical backaction depends on how the optical field is detuned from the cavity resonance. When detuning is zero, the optical field has no effect on the mechanical resonator. However, when the field is *red detuned*, that is when detuning Δ is negative, the optomechanical interaction shifts the mechanical resonance frequency down and broadens the mechanical linewidth Γ_m. Conversely, when the detuning is positive or *blue detuned*, the resonance frequency shifts up and the mechanical linewidth is narrowed.

As a final remark, given suitable experimental conditions, dynamical backaction allows for a straightforward way of preparing the mechanical resonator in the quantum ground state. The

7 At this point, we will remark that, like with many other definitions and notations in optomechanics, the council of Elrond has not yet convened, the Narsil remains broken and the signs of the dynamical backaction terms are at the mercy of the author and many have chosen, unwisely of course, the opposite convention.

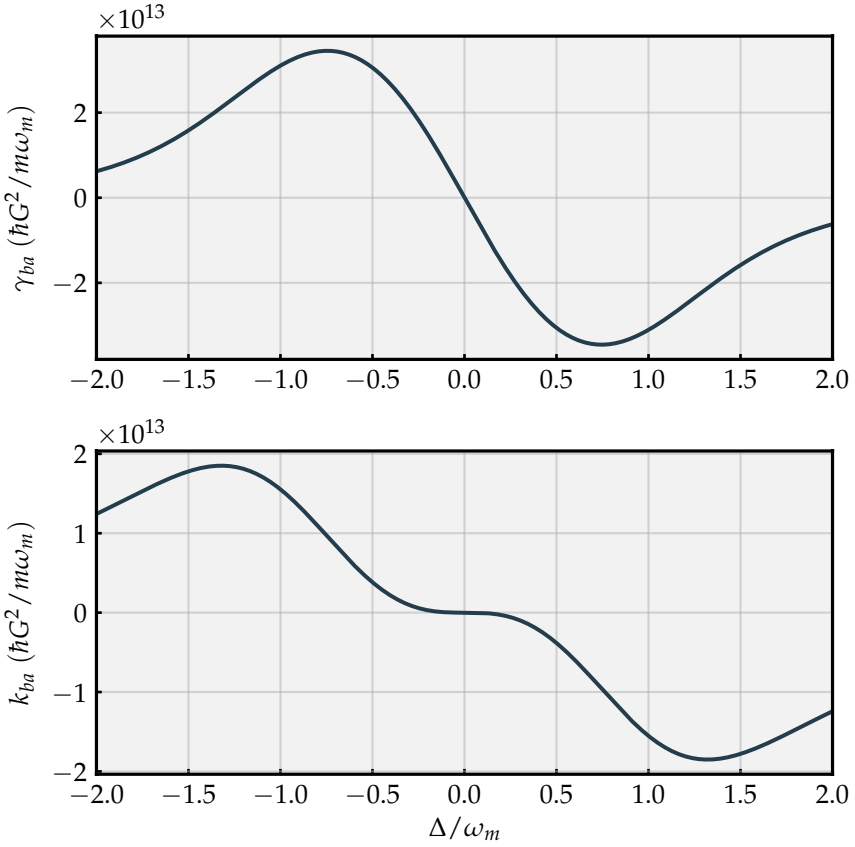

Figure 2.7: Here we show the optical spring and the frequency shift for an optomechanical system where $\kappa = 5\omega_m$. The magnitude and sign of the dynamical backaction depends on the detuning of the drive.

broadened mechanical linewidth corresponds to colder temperature. Given that a typical laser is at zero occupancy, the interaction can cool the resonator at a very high purity mechanical ground state, i.e. to a state where the ground state probability is high.

2.6 QUANTUM OPTOMECHANICS

While the classical treatment of the previous section is enough to describe many experiments and applications, many of the most interesting experiments in optomechanics require the full quantum treatment. We will start with a brief recapitulation of the quantum harmonic oscillator. In the following, symbols with 'hat' refer to quantum mechanical operators and ones without to classical variables. For example, $\hat{x}$ would be the position operator and x the position variable.

2.6.1 *Quantum Harmonic Oscillator*

The quantum harmonic oscillator is one of the first systems fully treated in a quantum mechanics course[8]. It features nonclassical properties, such as quantization of energy levels, but more importantly, it is a very useful model. In fact, the entire field of optomechanics mostly concerns coupled harmonic oscillators. To that end, let use remind ourselves about the harmonic oscillator Hamiltonian

$$H = \frac{\hat{p}}{2m} + m\omega_m^2 \hat{x}, \tag{2.64}$$

where $\hat{p}$ and $\hat{x}$ are momentum and position operators respectively. As opposed to classical variables, their commutator is no longer zero

$$[\hat{x}, \hat{p}] = \hat{x}\hat{p} - \hat{p}\hat{x} = i\hbar. \tag{2.65}$$

As a consequence, the product of the position and momentum standard deviations has a lower bound, also known as the Heisenberg uncertainty relation

$$\sigma_x \sigma_p \geqslant \frac{\hbar}{2}. \tag{2.66}$$

Instead of position and momentum, it is often more convenient to work on the so called number state. The energy of the state is expressed as number of quanta n each corresponding to amount of energy equal to $\hbar\omega_m$ and the state is denoted as ket $|n\rangle$. In the case of mechanical motion, the quantum of energy is called *phonon*. Instead of position and momentum operators, we defined creation and annihilation operators $\hat{b}^\dagger$ and $\hat{b}$ respectively that, as the name suggest, add or subtract an excitation. They relate to position and momentum operators as

$$\hat{x} = x_{zpf}\left(\hat{b} + \hat{b}^\dagger\right), \tag{2.67}$$

$$\hat{p} = ip_{zpf}\left(\hat{b} - \hat{b}^\dagger\right), \tag{2.68}$$

where we have introduced *zero point fluctuations* of position and momentum

$$x_{zpf} = \sqrt{\frac{\hbar}{2m\omega_m}}, \tag{2.69}$$

$$p_{zpf} = \sqrt{\frac{\hbar m\omega_m}{2}}. \tag{2.70}$$

8 Quite literally, any quantum mechanics book will do. The author was first subjected to [41]

The creation and annihilation operators act on number states as

$$\hat{b}|n\rangle = \sqrt{n}|n-1\rangle \tag{2.71}$$

$$\hat{b}^\dagger|n\rangle = \sqrt{n+1}|n+1\rangle. \tag{2.72}$$

With the ladder operators, the Hamiltonian becomes

$$H = \hbar\omega_m\left(\hat{b}^\dagger\hat{b} + \frac{1}{2}\right). \tag{2.73}$$

The operator $\hat{b}^\dagger\hat{b}$ is also known as the number operator $\hat{n}|n\rangle = n|n\rangle$. It should be noted that the ground state $|0\rangle$ has nonzero energy. When we are interested only in the dynamics of the system, we often omit the static $\hbar\omega_m/2$ -part.

Occasionally, it more convenient to work with dimensionless units, and to that end, we define dimensionless position and momentum

$$\hat{Q} = \frac{\hat{x}}{\sqrt{2}x_{zpf}} = \frac{1}{\sqrt{2}}\left(\hat{b} + \hat{b}^\dagger\right) \tag{2.74}$$

$$\hat{P} = \frac{\hat{p}}{\sqrt{2}p_{zpf}} = \frac{i}{\sqrt{2}}\left(\hat{b} - \hat{b}^\dagger\right), \tag{2.75}$$

where we have used capital $\hat{Q}$ for the dimensionless position and capital $\hat{P}$ for the dimensionless momentum.

2.6.2 *Thermal occupation and the ground state*

Before moving on to optomechanical dynamics, there are a couple of remarks that should be made about thermal occupation and the ground state. The ladder operators are defined with regard to the number or *Fock states* $|n\rangle$. However, an oscillator in contact with the environment is in an incoherent superposition of multiple Fock states. The probability weight for each occupation state is

$$p(n) = e^{-\frac{\hbar\omega_m n}{k_B T}}\left(1 - e^{-\frac{\hbar\omega_m}{k_B T}}\right), \tag{2.76}$$

where T is the temperature of the system and k_B the Boltzmann constant. It should be noted that the formula is valid for all harmonic oscillators even though we have used the mechanical resonance frequency. For other oscillators, simply replace ω_m with the correct frequency, e.g. the driving laser frequency. With the probability weight, we can calculate the mean occupancy

$$\bar{n} = \sum_{n=0}^{\infty} p(n)n = \left(e^{\frac{\hbar\omega_m}{k_B T}} - 1\right)^{-1}. \tag{2.77}$$

This formula has important consequences. First, a typical laser at Terahertz frequencies is at practically zero occupancy already at the room temperature and can thus act as a cooling bath for the mechanical resonator. Second, many nanomechanical resonators feature resonance frequencies of at most few tens of megahertz. This means that even when cooled to few milliKelvins inside a dilution refrigerator, these resonators still have an appreciable thermal occupation and thus need further active cooling to reach the ground state. At high temperatures, or when $k_B T \gg \hbar\omega_m$, the mean occupation can be approximated as

$$\bar{n} = \frac{k_B T}{\hbar\omega_m}. \tag{2.78}$$

A typical starting point for many optomechanical quantum protocols and thus an important benchmark for various systems, is the ability to cool he mechanical resonator's motion to the ground state. In optomechanics, the accepted criterion for a ground state mechanical resonator is that the *probability* of finding the resonator in state $|0\rangle$ is greater than half. This translates to mean that the occupation of the mechanical resonator must be less than one.

2.6.3 *Optomechanical Hamiltonian*

Now we are ready to dive into the quantum mechanical treatment of an optomechanical system. As a first simplification, we will only consider a single mechanical and single optical mode. This is a well justified choice if the modes are well separated, meaning that the distance from one optical mode to another is much larger than both the cavity linewidth and the mechanical frequency. Similarly, the mechanical modes of the system should be separated by much more than the mechanical linewidth Γ_m. With the caveats in place, we can write the Hamiltonian of the system as

$$H = H_m + H_o + H_D, \tag{2.79}$$

where H_m is the Hamiltonian for the mechanical oscillator, H_o for the optical and H_D for the drive. Omitting the drive for the moment, we can write the Hamiltonian explicitly as

$$H = \hbar\omega_m \left(\hat{b}^\dagger \hat{b} + \frac{1}{2}\right) + \hbar\omega_c(\hat{x}) \left(\hat{a}^\dagger \hat{a} + \frac{1}{2}\right), \tag{2.80}$$

where we have introduced the creation and annihilation operators $\hat{a}^\dagger$ and $\hat{a}$ for the optical mode. At first glance, we have only two separate harmonic oscillators. However, the optical resonance frequency depends on the position of the mechanical

resonator. As before, we may write $\omega_c(\hat{x}) = \omega_c - G\hat{x}$ where $G = -\partial\omega_c(\hat{x})/\partial\hat{x}$. We have also chosen to denote the *unperturbed* resonance frequency as ω_c for simplicity. Writing the position operator with the appropriate ladder operators, we find

$$H = \hbar\omega_m \hat{b}^\dagger\hat{b} + \hbar\omega_c \hat{a}^\dagger\hat{a} - \hbar G x_{zpf}\left(\hat{b}^\dagger + \hat{b}\right)\left(\hat{a}^\dagger\hat{a}\right), \tag{2.81}$$

where we have neglected the static $\hbar\omega_i/2$-parts. At this stage, it is convenient to introduce the *vacuum optomechanical coupling*

$$g_0 = G x_{zpf}, \tag{2.82}$$

the frequency shift of the cavity associated with the zero point fluctuation of the mechanical oscillator.

At first glance, the Hamiltonian looks simple, but it does contain three operator terms and is thus difficult to solve exactly. The way out is the same as in the classical case, namely we consider field fluctuations around a mean and introduce creation and annihilation operators for the field fluctuation such that $\hat{a}$ becomes

$$\hat{a} = \bar{a} + \delta\hat{a}, \tag{2.83}$$

and similarly for $\hat{a}^\dagger$. We then neglect second (or higher) order terms in $\delta\hat{a}$ and are left with the interaction

$$H_{int} = -\hbar g_0\left(\hat{b}^\dagger + \hat{b}\right)\left(\bar{a}^2 + \bar{a}\delta\hat{a} + \bar{a}\delta\hat{a}^\dagger\right). \tag{2.84}$$

The mean field results only in a static displacement and the 'meat' of the interaction is thus

$$\begin{aligned} H_{int} &= -\hbar g_0\bar{a}\left(\hat{b}^\dagger + \hat{b}\right)\left(\delta\hat{a} + \delta\hat{a}^\dagger\right) \\ &= -\hbar g\left(\hat{b}^\dagger\delta\hat{a} + \hat{b}^\dagger\delta\hat{a}^\dagger + \hat{b}\delta\hat{a} + \hat{b}\delta\hat{a}^\dagger\right), \end{aligned} \tag{2.85}$$

where we have introduced the *field enhanced optomechanical coupling*

$$g = g_0\bar{a} = g_0\sqrt{n_{cav}}, \tag{2.86}$$

where n_{cav} is the number of intracavity photons.

Let's pause for a moment here and qualitatively consider what happens in this interaction. First, the pair $\hat{b}^\dagger\delta\hat{a} + \hat{b}\delta\hat{a}^\dagger$ exchanges excitations between the cavity field and the mechanical resonator and it is sometimes referred to as the *beamsplitter interaction*. The other pair either creates or annihilates an excitation in *both* the mechanical resonator and is called *two mode squeezing*.

More interestingly, depending on the cavity detuning, we can choose to favour one over the other. The mechanism is that in a

frame rotating with the laser frequency, the operators evolve in time as

$$\delta\hat{a}(t) = \delta\hat{a}(0)e^{-i\Delta t}, \tag{2.87}$$

$$\delta\hat{b}(t) = \delta\hat{b}(0)e^{-i\omega_m t}. \tag{2.88}$$

Thus, the beam splitter interaction rotates at $\exp(\pm i(\Delta + \omega_m))$ and the squeezing interaction at $\exp(\pm i(\Delta - \omega_m))$.

If we set detuning at $\Delta = -\omega_m$, that is our drive is red detuned, the beamsplitter interaction is constant in time, but the squeezing terms rotate at $\pm 2\omega_m$. If this rate is much larger than the cavity linewidth, i.e. if the cavity is sideband resolved, the term can be neglected in what is known as the *rotating wave approximation* and the beamsplitter interaction is the dominant one.

2.6.4 *Quantum Langevin equations of motion*

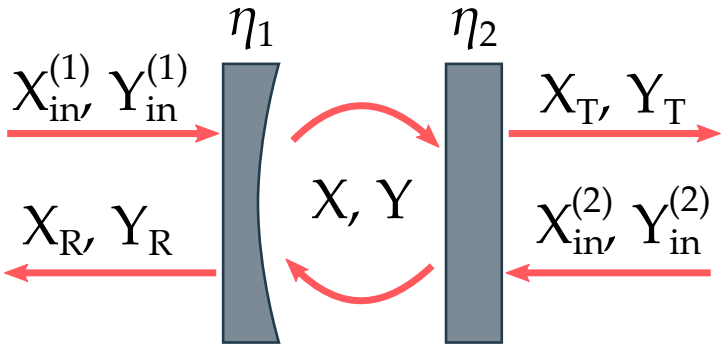

Figure 2.8: The optical fields involved in the quantum model of an optomechanical cavity. Here, we have chosen not to include the mechanical resonator for clarity. The cavity is driven on port 1 with coupling efficiency η_1. The fields $X_{in}^{(1)}$ and $Y_{in}^{(1)}$ contain both the drive and vacuum noise. The circulating cavity fields X and Y exit the cavity via both reflection X_R and Y_R and transmission X_T and Y_T. However, vacuum noise also enters via the transmission port 2, as signified by fields $X_{in}^{(2)}$ and $Y_{in}^{(2)}$

Before writing the Quantum Langevin[9] equations, there are a couple of remarks to make. First, the cavity field operator $\delta\hat{a}$ is not an observable. We only have access to the amplitude and phase quadratures of the light and we need corresponding

9 Sometimes also known as the Heisenberg-Langevin equations.

operators $\hat{X}$ and $\hat{Y}$ respectively, related to the field operators as

$$\hat{X} = \frac{1}{\sqrt{2}}\left(\delta\hat{a} + \delta\hat{a}^\dagger\right) \tag{2.89}$$

$$\hat{Y} = \frac{i}{\sqrt{2}}\left(\delta\hat{a} - \delta\hat{a}^\dagger\right). \tag{2.90}$$

It is a matter of taste whether to solve the systems of equations with the creation and annihilation operators and then calculate the amplitude or phase of the output field or to have equations of motion for the amplitude and phase to begin with. Here, we choose to use optical quadratures from the beginning since the interaction of the mechanics with different quadratures is explicit.

Let us then sketch the system under investigation. We have a two port optical cavity, that is both mirrors are partially transmissive with decay rates κ_1 and κ_2. The losses are negligible such that the total decay rate is simply the sum of these decay rates $\kappa = \kappa_1 + \kappa_2$. We drive the cavity with a large, coherent amplitude through port 1. However, the drive has vacuum correlated noise and vacuum noise also enters through port 2. The mechanical resonator is damped and driven by both coupling to the environment via thermal noise and by the radiation pressure of the cavity field. The end result is the following set of equations of motion for the optical and mechanical fluctuations [**Bowen2016**]

$$\dot{\hat{X}} = -\frac{\kappa}{2}\hat{X} - \Delta\hat{Y} + \sqrt{\kappa_1}\hat{X}_{in}^{(1)} + \sqrt{\kappa_2}\hat{X}_{in}^{(2)}, \tag{2.91}$$

$$\dot{\hat{Y}} = -\frac{\kappa}{2}\hat{Y} + \Delta\hat{X} + 2gQ + \sqrt{\kappa_1}\hat{Y}_{in}^{(1)} + \sqrt{\kappa_2}\hat{Y}_{in}^{(2)}, \tag{2.92}$$

$$\dot{\hat{Q}} = \omega_m\hat{P}, \tag{2.93}$$

$$\dot{\hat{P}} = -\omega_m\hat{Q} - \Gamma_m\hat{P} + \sqrt{2\Gamma_m}F_{th} + 2g\hat{X}. \tag{2.94}$$

For simplified notation, we will write the optical noise terms as

$$\widetilde{X}_{in} = \sqrt{\eta_1}\hat{X}_{in}^{(1)} + \sqrt{\eta_2}\hat{X}_{in}^{(2)}, \tag{2.95}$$

$$\widetilde{Y}_{in} = \sqrt{\eta_1}\hat{Y}_{in}^{(1)} + \sqrt{\eta_2}\hat{Y}_{in}^{(2)}, \tag{2.96}$$

where $\eta_i = \kappa_i/\kappa$ and we have assumed that the losses in the cavity are negligible such that $\eta_1 + \eta_2 = 1$. We can introduce losses by adding another port, κ_{loss} through which vacuum noise would also enter.

The two equations of motion for the position and momentum

are combined leaving us with

$$\dot{\hat{X}} = -\frac{\kappa}{2}\hat{X} - \Delta\hat{Y} + \sqrt{\kappa}\widetilde{X}_{in}, \tag{2.97}$$

$$\dot{\hat{Y}} = -\frac{\kappa}{2}\hat{Y} + \Delta\hat{X} + 2gQ + \sqrt{\kappa}\widetilde{Y}_{in}, \tag{2.98}$$

$$\frac{\ddot{\hat{Q}}}{\omega_m} = -\omega_m\hat{Q} - \Gamma_m\frac{\dot{\hat{Q}}}{\omega_m} + \sqrt{2\Gamma_m}F_{th} + 2g\hat{X}. \tag{2.99}$$

Here we see that the *amplitude* of the field drives the mechanical resonator and the record of the position is imprinted on the *phase* of the field. Thus we need to either directly measure the phase of the output field via e.g. balanced homodyne or have a way of transferring the motion record to the amplitude quadrature. Again, the equations give a good hint on where to look: with nonzero detuning, the phase and amplitude are coupled. Measuring on the side of the cavity, away from the resonance, thus transforms phase fluctuations to amplitude fluctuations.

Again, the solution to this set of equations is most conveniently found in frequency domain. The Fourier transform leaves us with

$$-i\Omega\hat{X}(\Omega) = -\frac{\kappa}{2}\hat{X}(\Omega) - \Delta\hat{Y}(\Omega) + \sqrt{\kappa}\widetilde{X}_{in}, \tag{2.100}$$

$$-i\Omega\hat{Y}(\Omega) = -\frac{\kappa}{2}\hat{Y}(\Omega) + \Delta\hat{X}(\Omega) + 2g\hat{Q}(\Omega) + \sqrt{\kappa}\widetilde{Y}_{in}. \tag{2.101}$$

$$-\Omega^2\hat{Q}(\Omega) = -\omega_m^2\hat{Q}(\Omega) + i\Gamma_m\Omega\hat{Q}(\Omega) + \omega_m\left(\sqrt{2\Gamma_m}F_{th} + 2g\hat{X}(\Omega)\right). \tag{2.102}$$

Again, we can identify the dimensionless mechanical susceptibility

$$\chi_m(\Omega) = \frac{\omega_m}{\omega_m^2 - \Omega^2 - \Gamma_m\Omega}, \tag{2.103}$$

and write the equation for the dimensionless position as

$$\hat{Q}(\Omega) = \chi_m(\Omega)\left(\sqrt{2\Gamma_m}F_{th} + 2g\hat{X}(\Omega)\right). \tag{2.104}$$

If we substitute in $\hat{X}(\Omega)$, interesting things happen. First, we recover the same dynamical backaction as in the classical case modifying the mechanical susceptibility in a similar fashion. However, we also have an extra driving term from the quantum noise that we neglected in the classical limit. To write the contributions more explicitly, let us solve the equations of motion for amplitude and phase

$$\left(\frac{\kappa}{2} - i\Omega\right)\hat{X}(\Omega) = -\Delta\hat{Y}(\Omega) + \sqrt{\kappa}\widetilde{X}_{in}, \tag{2.105}$$

$$\left(\frac{\kappa}{2} - i\Omega\right)\hat{Y}(\Omega) = \Delta\hat{X}(\Omega) + 2g\hat{Q}(\Omega) + \sqrt{\kappa}\widetilde{Y}_{in}. \tag{2.106}$$

We first substitute the phase $\hat{Y}$ in equation 2.105 to find

$$\hat{X}(\Omega) = \frac{-\Delta}{\frac{\kappa}{2} - i\Omega}\left(\frac{1}{\frac{\kappa}{2} - i\Omega}\left(\Delta\hat{X}(\Omega) + 2g\hat{Q}(\Omega) + \sqrt{\kappa}\widetilde{Y}_{in}\right) + \sqrt{\kappa}\widetilde{X}_{in}\right) \tag{2.107}$$

Solving for $\hat{X}(\Omega)$, we are left with

$$\hat{X}(\Omega) = \frac{-\Delta}{\left(\frac{\kappa}{2} - i\Omega\right)^2 + \Delta^2}\left(2g\hat{Q}(\Omega) + \sqrt{\kappa}\widetilde{Y}_{in}\right) + \frac{\frac{\kappa}{2} - i\Omega}{\left(\frac{\kappa}{2} - i\Omega\right)^2 + \Delta^2}\sqrt{\kappa}\widetilde{X}_{in}. \tag{2.108}$$

Again, for notational convenience, we will define two new functions

$$\nu(\Omega) = \frac{-\Delta}{\left(\frac{\kappa}{2} - i\Omega\right)^2 + \Delta^2}, \tag{2.109}$$

$$u(\Omega) = \frac{\frac{\kappa}{2} - i\Omega}{\left(\frac{\kappa}{2} - i\Omega\right)^2 + \Delta^2}. \tag{2.110}$$

With these, we can rewrite $\hat{X}(\Omega)$ and solve for $\hat{Y}(\Omega)$

$$\hat{X}(\Omega) = \nu(\Omega)\left(2g\hat{Q}(\Omega) + \sqrt{\kappa}\widetilde{Y}_{in}\right) + u(\Omega)\sqrt{\kappa}\widetilde{X}_{in}, \tag{2.111}$$

$$\hat{Y}(\Omega) = u(\Omega)\left(2g\hat{Q}(\Omega) + \sqrt{\kappa}\widetilde{Y}_{in}\right) - \nu(\Omega)\sqrt{\kappa}\widetilde{X}_{in}. \tag{2.112}$$

Substituting $\hat{X}$ back into equation 2.104, we find

$$\chi_m^{-1}\hat{Q}(\Omega) = \sqrt{2\Gamma_m}F_{th} + 2g\left(\nu(\Omega)\left(2g\hat{Q}(\Omega) + \sqrt{\kappa}\widetilde{Y}_{in}\right) + u(\Omega)\sqrt{\kappa}\widetilde{X}_{in}\right) \tag{2.113}$$

$$\left(\chi_m^{-1} + \chi_{dba}^{-1}\right)\hat{Q}(\Omega) = \sqrt{2\Gamma_m}F_{th} + 2g\left(\nu(\Omega)\sqrt{\kappa}\widetilde{Y}_{in} + u(\Omega)\sqrt{\kappa}\widetilde{X}_{in}\right), \tag{2.114}$$

where we identified the dynamical backaction susceptibility as

$$\chi_{dba} = 4g^2\nu(\Omega), \tag{2.115}$$

such that the the effective susceptibility is $\chi_{eff}^{-1} = \chi_m^{-1} + \chi_{dba}^{-1}$. At the risk of repeating myself[10], let us write the solution for position once more

$$\hat{Q}(\Omega) = \chi_{eff}\left(\sqrt{2\Gamma_m}F_{th} + 2g\left(\nu(\Omega)\sqrt{\kappa}\widetilde{Y}_{in} + u(\Omega)\sqrt{\kappa}\widetilde{X}_{in}\right)\right). \tag{2.116}$$

10 Repetita iuvant, as the Romans, or perhaps medieval scholars, allegedly said!

Up until the very end, the solution is identical to the the classical one - motion with modified susceptibility driven by thermal motion. But, in the quantum regime, the quantum noise of the light field becomes significant and we have an additional driving term, the so called *quantum backaction* (QBA) due to the so-called radiation pressure shot noise.

2.6.5 *Quantum backaction and the Standard Quantum Limit*

To understand the consequences of the QBA, let us consider resonant probing of the mechanical motion, that is, set $\Delta = 0$. This is a very relevant example as resonant probing nullifies the effect of dynamical backaction allowing us to measure unperturbed mechanical motion. Such measurement is also a starting point of the quantum feedback scheme presented later, making the case highly relevant.

As said, dynamical backaction has no effect and the coupling between optical quadratures vanishes and we are left with

$$\hat{Q}(\Omega) = \chi_m \left(\sqrt{2\Gamma_m} F_{th} + \frac{2g}{\frac{\kappa}{2} - i\Omega} \sqrt{\kappa} \widetilde{X}_{in} \right), \tag{2.117}$$

$$\hat{Y}(\Omega) = \frac{1}{\frac{\kappa}{2} - i\Omega} \left(2g\hat{Q}(\Omega) + \sqrt{\kappa} \widetilde{Y}_{in} \right). \tag{2.118}$$

We do not have direct access to the cavity field. We can only measure the cavity field leaving the cavity from one of the ports. The output field is calculated with the input-output relations as

$$\hat{Y}(\Omega)_{out} = -\hat{Y}^{(1)}_{in} + \sqrt{\eta_1 \kappa} \hat{Y}(\Omega), \tag{2.119}$$

where we have chosen port 1 as the output port. The total output field, is then

$$\hat{Y}_{out} = -Y^{(1)}_{in} + \sqrt{\eta_1 \kappa} \left[\frac{1}{\frac{\kappa}{2} - i\Omega} \left(2g\hat{Q}(\Omega) + \sqrt{\kappa} \widetilde{Y}_{in} \right) \right] \tag{2.120}$$

We can simplify the equation a little by collecting all the phase noise terms under single variable

$$\widetilde{Y}'_{in} = -Y^{(1)}_{in} + \frac{\sqrt{\eta_1}\kappa}{\frac{\kappa}{2} - i\Omega} \left(\sqrt{\eta_1} Y^{(1)}_{in} + \sqrt{1-\eta_1} Y^{(2)}_{in} \right), \tag{2.121}$$

where we use the prime to signify that this noise term is different from the one introduced in equations 2.95 and 2.96 and where we have substituted for $\eta_2 = 1 - \eta_1$. Rearranging, we find

$$\widetilde{Y}'_{in} = \left(\frac{2\sqrt{\eta_1}}{1 - \frac{i2\Omega}{\kappa}} - 1 \right) Y^{(1)}_{in} + \frac{2\sqrt{\eta_1(1-\eta_1)}}{1 - \frac{i2\Omega}{\kappa}} Y^{(2)}_{in}. \tag{2.122}$$

Interestingly, if we calculate the symmetrized power spectrum, assuming no cross correlation between the noises, for this noise operator, we find

$$\bar{S}_{\widetilde{Y}'_{in}\widetilde{Y}'_{in}} = \frac{1}{2}, \tag{2.123}$$

the same we would expect for any of the individual noise terms $Y^{(i)}_{in}$.

The solution for position $\hat{Q}(\Omega)$ can also be rearranged a bit to make the relation between QBA and thermal noise explicit

$$\hat{Q}(\Omega) = \chi_m \left(\sqrt{2\Gamma_m} F_{th} + \frac{\sqrt{2\Gamma_m} 2g\kappa}{\sqrt{2\Gamma_m}\frac{\kappa}{2}\left(1 - \frac{i2\Omega}{\kappa}\right)} \widetilde{X}_{in} \right), \tag{2.124}$$

$$= \chi_m \sqrt{2\Gamma_m} \left(F_{th} + \frac{\sqrt{2}}{1 - \frac{i2\Omega}{\kappa}} \frac{2g}{\sqrt{\kappa\Gamma_m}} \widetilde{X}_{in} \right), \tag{2.125}$$

$$= \chi_m \sqrt{2\Gamma_m} \left(F_{th} + \sqrt{2C_{eff}} \widetilde{X}_{in} \right), \tag{2.126}$$

where we have identified the effective cooperativity

$$C_{eff} = \frac{C}{\left(1 - \frac{i2\Omega}{\kappa}\right)^2} = \frac{4g^2}{\kappa\Gamma_m} \frac{1}{\left(1 - \frac{i2\Omega}{\kappa}\right)^2}, \tag{2.127}$$

where the *cooperativity* C is defined as

$$C = \frac{4g^2}{\kappa\Gamma_m} \tag{2.128}$$

We can think of the cooperativity as the ratio between coupling and loss rates.

With the rearrangement in equation 2.126, the effect of quantum noise becomes even more explicit. The quantum noise drives the mechanical motion in a similar fashion as the thermal noise.

With the digressions out of the way, we can then finally write the output field and calculate the corresponding spectral density. The phase $\hat{Y}_{out}(\Omega)$ is then

$$\hat{Y}_{out}(\Omega) = \widetilde{Y}'_{in} + 2\sqrt{\eta_1 \Gamma_m C_{eff}} \left[\chi_m \sqrt{2\Gamma_m} \left(F_{th} + \sqrt{2C_{eff}} \widetilde{X}_{in} \right) \right]. \tag{2.129}$$

where we have again identified the effective cooperativity

$$\frac{2g\sqrt{\eta_1\kappa}}{\frac{\kappa}{2} - i\Omega} = 2\sqrt{\eta_1 \Gamma_m C_{eff}}. \tag{2.130}$$

Thus, the cooperativity also determines the signal to noise of the position relative to the background! The symmetrized spectral density is then

$$\bar{S}_{\hat{Y}_{out}\hat{Y}_{out}}(\Omega) = \bar{S}_{\widetilde{Y}'_{in}\widetilde{Y}'_{in}} + 4\eta_1 \Gamma_m |C_{eff}| \left[|\chi_m|^2 2\Gamma_m \left(\bar{S}_{FF} + 2|C_{eff}| \bar{S}_{\widetilde{X}_{in}\widetilde{X}_{in}} \right) \right]. \tag{2.131}$$

Both shot noise spectra $\bar{S}_{\tilde{Y}'_{in}\tilde{Y}'_{in}}$ and $\bar{S}_{\tilde{X}_{in}\tilde{X}_{in}}$ are valued at $1/2$ at all frequencies and the thermal noise spectrum is

$$\bar{S}_{F_{th}F_{th}} = n_{th} + \frac{1}{2} \approx n_{th}, \tag{2.132}$$

where we have chosen a regime where n_{th} is much larger than $1/2$. The final spectrum then reads

$$\bar{S}_{\hat{Y}_{out}\hat{Y}_{out}}(\Omega) = \frac{1}{2} + 8\eta_1\Gamma_m^2|C_{eff}||\chi_m^2|\left(n_{th} + |C_{eff}|\right). \tag{2.133}$$

The expression inside the last parenthesis invites a closer look. First, we have the effective cooperativity. In the unresolved sideband limit, where $\kappa \gg \omega_m$, we may simply write $C = C_{eff}$. The total force noise $\bar{S}_{FF}^{tot}$ then consists of the thermal force $\bar{S}_{F_{th}F_{th}}$ and the quantum backaction drive $\bar{S}_{QBA}$

$$\bar{S}_{FF}^{tot} = S_{F_{th}F_{th}} + S_{QBA} = n_{th} + C. \tag{2.134}$$

Let us then take the ratio of the QBA to the thermal force

$$\frac{\bar{S}_{QBA}}{\bar{S}_{FF}} = \frac{C}{n_{th}} = C_q, \tag{2.135}$$

where we have introduced the *quantum cooperativity* that quantifies the ratio between thermal forces and the quantum backation. Let us write it out explicitly

$$C_q = \frac{4g^2}{\kappa n_{th}\Gamma_m} = \frac{4g^2}{\kappa\Gamma_{decoh}}, \tag{2.136}$$

where we have introduced the mechanical decoherence rate $\Gamma_{decoh} = \Gamma_m(n_{th} + 1/2)$. A regime where $C_q > 1$ is especially interesting. This means that the quantum backaction exceeds the incoherent thermal drive in importance.

To give an alternative interpretation, let us introduce the measurement rate

$$\Gamma_{meas} = \frac{4g^2}{\kappa}, \tag{2.137}$$

and rewrite the output spectrum 2.131 with its help. Here, we continue to operate with the unresolved sideband assumption[11] such that $C_{eff} = C$ and we find

$$\bar{S}_{\hat{Y}_{out}\hat{Y}_{out}}(\Omega) = \frac{1}{2} + 4\eta_1\Gamma_{meas}\bar{S}_{QQ}(\Omega), \tag{2.138}$$

where we have chosen not to write the position spectrum $\bar{S}_{QQ}$ explicitly. The measurement rate can then be thought as the rate

11 After all, our experiments operate in this regime.

at which we extract information from the system. Looking back at the quantum cooperativity, we can write it as

$$C_q = \frac{\Gamma_{meas}}{\Gamma_{decoh}}, \tag{2.139}$$

that is, the ratio of the rate at which we extract information against the rate at which the information decoheres meaning that the cooperativity is not only a measure of how important QBA is, but also a measure of our measurement efficiency.

Looking at equation 2.138, it would seem that we can reach arbitrarily good signal to noise or alternatively, arbitrarily small imprecision. The noise floor is constant 1/2 and whatever motion there is, gets multiplied by the measurement rate that is proportional to our probe power[12] where the only limit is the cavity and physical limitations of the equipment.

An alternative way to think about the noise floor is, that we can calculate, how much motion would produce a signal corresponding to the shot noise level[13]. This imprecision is then

$$\bar{S}_{QQ}^{imp} = \frac{1}{4\eta_1\Gamma_{meas}}\bar{S}_{\hat{Y}_{in}\hat{Y}_{in}}. \tag{2.140}$$

As intuited, the smallest motion that can be measured can be improved without limit by cranking up the measurement strength.

Writing the output field with the equivalent position imprecision, we get

$$\bar{S}_{\hat{Y}_{out}\hat{Y}_{out}}(\Omega) = 4\eta_1\Gamma_{meas}\left(\bar{S}_{QQ}^{imp} + \bar{S}_{QQ}^{thermal} + \bar{S}_{QQ}^{QBA}\right), \tag{2.141}$$

where we have separated the position spectrum to thermal and backaction noise. The above expression gives us the *apparent mechanical displacement*. Before going further, let us (once more) write the contributing terms, evaluated at the mechanical frequency ω_m

$$\bar{S}_{QQ}^{imp}(\omega_m) = \frac{1}{8\eta_1\Gamma_{meas}}, \tag{2.142}$$

$$\bar{S}_{QQ}^{thermal}(\omega_m) = 2\Gamma_m|\chi_m(\omega_m)|^2\left(n_{th} + \frac{1}{2}\right), \tag{2.143}$$

$$\bar{S}_{QQ}^{QBA}(\omega_m) = 2\Gamma_m|\chi_m(\omega_m)|^2\frac{\Gamma_{meas}}{\Gamma_m}. \tag{2.144}$$

Here, $|\chi_m(\omega_m)|^2 = 1/\Gamma_m^2$ and, to maintain consistency between the terms, we have used the measurement rate to write the backaction spectrum. Here, the interplay between the contributions

12 $\Gamma_{meas} \propto g^2 = g_0^2 n_{cav}$

13 Strictly speaking, this term can also include classical noise, but for quantum experiments, we want to be as close to the shot noise limit as possible and thus the classical contribution is taken to be insignificant and thus neglected.

is the following: As measurement rate increases, the imprecision decreases, but the backaction rate increases while the thermal force is a constant lower bound on the measurement. The point of lowest total uncertainty is called the *Standard Quantum Limit* (SQL) and it is most clearly demonstrated in figure 2.9.

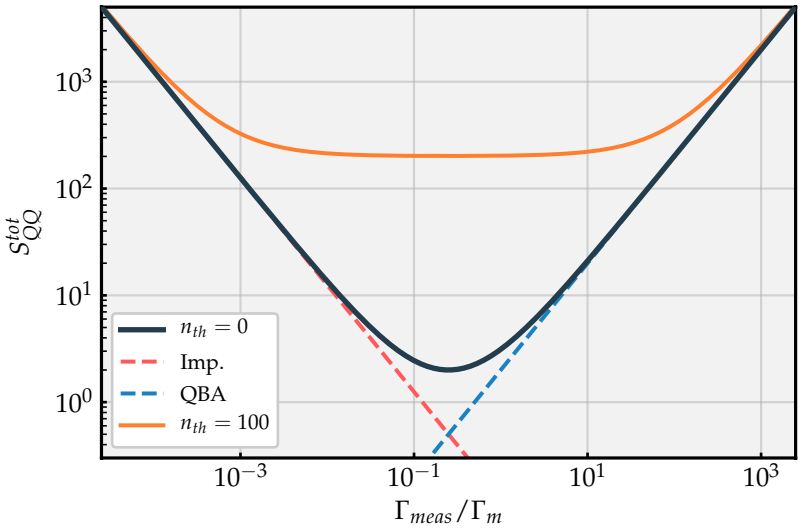

Figure 2.9: The standard quantum limit. The dark gray line corresponds to the ground state SQL, where there are zero thermal phonons and the orange line to such situation, where there are 100 thermal phonons. The dashed red line corresponds to the measurement imprecision and the dashed blue line to the quantum backaction noise. The mechanical linewidth is set to $\Gamma_m = 1$ in the graph. We can read the minimum at $\Gamma_{meas} = \Gamma_m/4$.

We cannot stress enough, that the existence of SQL is **not** due to any practical measurement apparatus or specific optomechanical platform but rather a direct consequence of quantum mechanics. It sets the lower limit on the displacement that can be measured. Remember, that so far, there are no external forces other than those resulting from coupling to the thermal environment and the QBA from the probe. One very salient example is the interferometric detection of gravitational waves, such as is done at LIGO or VIRGO. The passing of a wave causes a displacement in a multi-kilometer long interferometer and this displacement needs to be distinguished from the background given by the SQL.

2.6.6 *Sideband cooling*

In the previous section we reached a startling conclusion. No matter what, there is a fundamental limit in position measurement accuracy. However, under suitable experimental conditions that will be elaborated in a moment, the optomechanical interaction allows for *quantum* control of motion. We already saw in the classical treatment, that the dynamical backaction can broaden the mechanical linewidth and this broadening is interpreted as cooling of the mechanical mode's temperature. As a shot noise limited laser light source can be considered to be a zero thermal phonon bath, in principle this process can prepare the mechanical mode in the ground state. The optomechanical interaction facilitates both cooling and heating of the mechanical resonator. At the same time, without external forces, the resonator would equilibrate with the bath. The *change* in the occupation can thus be written as

$$\dot{n} = (n+1)\left(A^{+} + A^{+}_{th}\right) + n\left(A^{-} + A^{-}_{th}\right), \tag{2.145}$$

where we have introduced the thermal and optical transition rates $A^{\pm}_{th}$ and $A^{\pm}$ respectively. The thermal rates are

$$A^{+}_{th} = n_{th}\Gamma_m, \tag{2.146}$$

$$A^{-}_{th} = (n_{th}+1)\Gamma_m. \tag{2.147}$$

If we turn off the optical interaction, that is $A^{\pm} = 0$, the equation of motion for mean occupation becomes

$$\dot{n} = (n+1)n_{th}\Gamma_m - n(n_{th}+1)\Gamma_m. \tag{2.148}$$

For the equilibrium, we set $\dot{n} = 0$ and we find the steady state occupation $n_{ss} = n_{th}$.

Due to the cavity, the two optical transition rates have different values. Their balance is then the damping – or anti-damping – rate of the mechanical resonator

$$\Gamma_{opt} = A^{-} - A^{+}. \tag{2.149}$$

The steady state, or the final occupation n_f is then

$$n_f = \frac{A^{+} + n_{th}\Gamma_m}{\Gamma_{opt} + \Gamma_m} \approx \frac{A^{+}}{\Gamma_{opt}} + n_{th}\frac{\Gamma_m}{\Gamma_{opt}}, \tag{2.150}$$

where we have approximated $\Gamma_{opt} \gg \Gamma_m$. For quantum experiments, the mechanical linewidth is often less than one hertz whereas Γ_{opt} can be tens of hertz. If $\omega_m \gg \kappa$, $\Gamma_{opt} \approx 4g^2/\kappa$, the final occupation becomes

$$n_f = \frac{A^{+}}{\Gamma_{opt}} + \frac{1}{C_q}. \tag{2.151}$$

Thus, the quantum cooperativity needs to be greater than one, if the final occupation is to be less than one.

The remaining matter is then the form of the optical transition rates, and there Fermi's golden rule can be applied to find

$$A^{\pm} = g_0^2 S_{NN}(\mp\omega_m), \tag{2.152}$$

where the photon number spectrum is

$$S_{NN}(\omega) = n_{cav}\frac{\kappa}{\left(\frac{\kappa}{2}\right)^2 + (\Delta+\omega)^2}, \tag{2.153}$$

is the photon number noise spectrum. It should be reassuring, that the expression for the optomechanical damping obtained this way is the same as the one we found previously by solving the equations of motion. We can immediately identify the first criterion for ground state cooling. The second term in equation 2.150 must be smaller than one. In practice, this is not a very prohibitive obstacle. Quality factors of tens and hundreds of million are commonplace and a moderate cryogenic environment reduces n_{th} such that the thermal contribution to the final occupation is small already at moderate damping Γ_{opt}. However, the first term $A^+/(A^- - A^+)$ is more interesting to analyse. Let us write it out explicitly

$$\frac{A^+}{A^- - A^+} = n_{min}^{SB} = \left[\frac{\left(\frac{\kappa}{2}\right)^2 + (\Delta-\omega_m)^2}{\left(\frac{\kappa}{2}\right)^2 + (\Delta+\omega_m)^2} - 1\right]^{-1}, \tag{2.154}$$

where we have defined the minimum achievable phonon number in sideband cooling n_{min}^{SB}. We have also included superscript 'SB' to underline that this is the limit in *sideband cooling*. As will become evident in later sections, measurement based protocols can surpass this limit.

The limit is a function of optical linewidth, detuning and mechanical resonance frequency. It is instructive to consider two regimes - the resolved and unresolved sideband cavities. The behaviour of n_{min}^{SB} as a function of detuning Δ is shown in figure 2.10. As we see, for a sufficiently unresolved cavity, the final occupation never reaches the ground state[14]. The optimal detuning, that is detuning that allows for lowest occupation, depends on the cavity linewidth and mechanical resonance frequency. Solving for the optimal detuning, we find

$$\Delta_{min} = -\frac{1}{2}\sqrt{\kappa^2 + 4\omega_m^2}. \tag{2.155}$$

As shown in figure 2.11 when $\omega_m \gg \kappa$, we can approximate $\Delta_{min} \approx \omega_m$ and in the opposite regime $\kappa \gg \omega_m$, the optimal detuning is $\Delta_{min} \approx \kappa/2$.

14 As a reminder, the optomechanical ground state is occupation less than one.

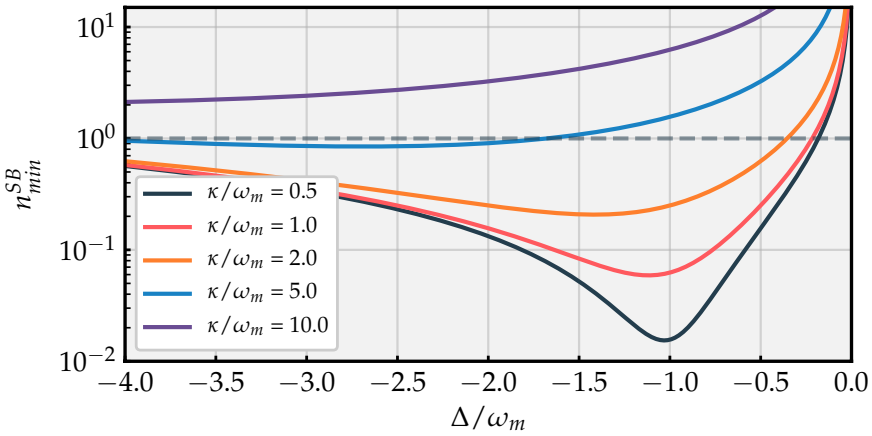

Figure 2.10: The minimum achievable occupation, given negligible thermal occupation. Increasing sideband resolution allows for ever lower occupation. The optical detuning for the minimum changes with the κ/ω_m ratio and too high ratio prohibits ground state cooling altogether.

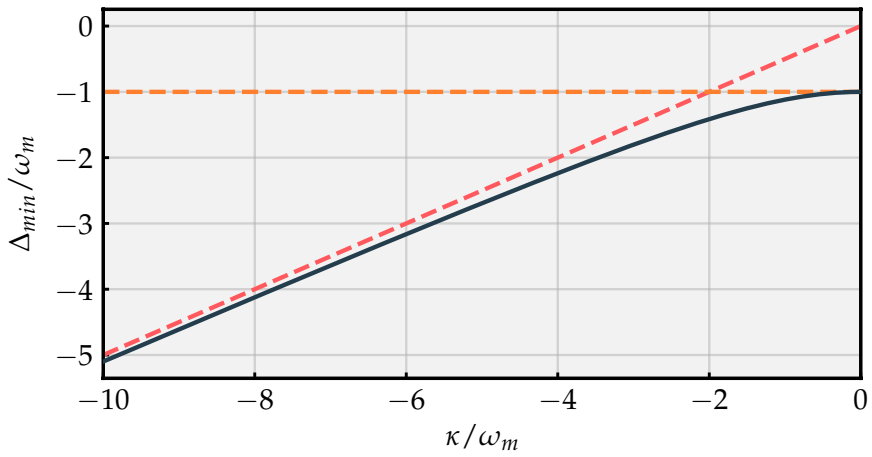

Figure 2.11: The black line shows the optimal detuning (equation 2.155) and the asymptotic behaviour. When $\kappa \gg \omega_m$, the optimal detuning for sideband cooling approaches $\kappa/2$, here marked with the red dashed line. When $\omega_m \gg \kappa$ the optimal detuning is ω_m, marked with dashed orange line.

As a final note, equation 2.154 can be simplified for the resolved and unresolved regimes. When the cavity is resolved, the minimum occupation is $n^{SB}_{min} = (\kappa/4\omega_m)^2$ which is well below one whereas in the unresolved case, the minimum is $n^{SB}_{min} = \kappa/4\omega_m$, this time greater than one.

The conclusion is then, that in order to sideband cool a mechanical resonator to the ground state, the optical cavity needs to

sufficiently resolve the mechanical sideband[15]. In practice, this slightly complicates experimental design[16]. For silicon nitride membrane resonators, the resonance frequency of the mode of interest is typically between 1 and 1.5 megahertz. To reach an optical linewidth below megahertz then requires both very high finesse mirrors and a long cavity. Both of these features increase the difficulty of operating the system. However, an alternative approach, the measurement based quantum control is agnostic to sideband resolution and also, under suitable experimental conditions, allows for preparation of the motional ground state. We will cover this approach in more detail in a later chapter.

2.6.7 *Modelling inefficiencies*

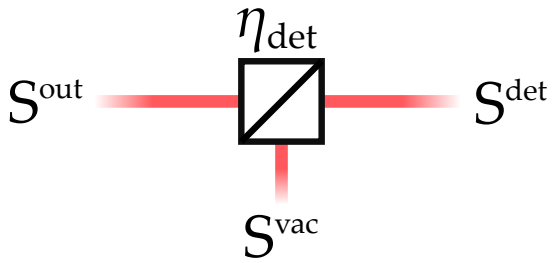

Figure 2.12: Detection inefficiency can be modelled as a beam splitter in the measurement path where part of the measurement signal, here labeled as S^{out}, is replaced by vacuum noise S^{vac} resulting in detected spectrum S^{det}.

As much as we would like, the path from the cavity to detection is not without losses. Imperfections in the optical components along the way scatter and absorb some of the light and the detector has below unity quantum efficiency, essentially meaning that not every photon creates an electron in the photodiode. We can imagined the output light passing through a beamsplitter, where part of the signal is replaced by vacuum noise, as shown in figure 2.12. We will thus introduce *detection efficiency* η_D such that the detected phase is

$$\hat{Y}_{\mathrm{det}} = \sqrt{\eta_D}\hat{Y}_{\mathrm{out}} + \sqrt{1-\eta_D}Y_v, \tag{2.156}$$

where part of the detected signal is replaced by vacuum noise. The vacuum noise is again uncorrelated and can be absorbed to the phase noise operator such that the shot noise background

15 Althought it is possible to use properly squeezed light to surpass this limit [42].

16 Though not that much. Resolved sideband systems are routinely utilized in many experiments.

is still 1/2. The end result is that we simply multiply $\hat{Q}$ in the output field by $\sqrt{\eta_D}$ such that the output field becomes

$$\bar{S}_{\hat{Y}_{out}\hat{Y}_{out}}(\Omega) = \frac{1}{2} + 4\eta_D\eta_1\Gamma_{meas}\bar{S}_{QQ}(\Omega). \tag{2.157}$$

2.7 MEMBRANE IN THE MIDDLE

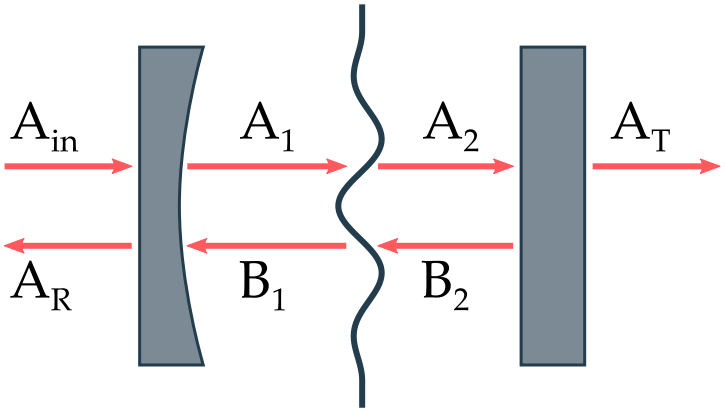

Figure 2.13: The membrane in the middle system can be modelled as a Fabry-Pérot cavity, that is divided into two subcavities by a thin, dielectric membrane. Inside each subcavity, there are left and right travelling fields labelled A_1, A_2, B_1 and B_2. For completeness, we have included the input field A_{in}, the reflected field A_R and the transmitted field A_T.

All of the considerations so far have assumed a Fabry-Pérot cavity with a movable end mirror. However, as we already saw in the introduction, optomechanical systems come in multiple shapes and forms where the common thread is that the motion of the mechanical resonator modifies the cavity resonance.

The chosen approach in Copenhagen quantum optomechanics experiments is the so called *membrane in the middle* (MIM) geometry. Instead of a movable end mirror, we have a static Fabry-Pèrot cavity and introduce a thin, dielectric membrane in the middle of the cavity and, as we will see, this gives rise to exactly the same dispersive coupling as in the case of the movable end mirror. The main advantage of the MIM geometry is that it allows for independent engineering of both the nanomechanical resonator and the cavity mirrors without compromising e.g. the mass of the resonator or the reflectivity of the mirror.

In the following treatment, we follow mostly the analysis presented in [43, 44, 45]. The starting point of the analysis is the the usual Fabry-Pèrot cavity of length L formed by two mirrors with reflectivities $-r_1$ and $-r_2$ and transmissivities t_1 and t_2. In

the cavity, near the center, there is a dielectric membrane at position x dividing the cavity into two subcavities. The membrane is partially reflective with reflection r_m and transmission t_m. In each subcavity, there are two electric fields, the right propagating A_1 and A_2 and the left propagating B_1 and B_2. The cavity fields are presented in figure 2.13.

Since we are mostly interested in how the mechanical motion modifies the cavity parameters, we will make the simplifying assumption, that the cavity end mirrors are perfectly reflective. This is not a very far fetched assumption. Transmissivities as low as few tens of part-per-million (ppm) are commonplace. The equations determining the cavity fields are then

$$\begin{aligned} A_1 &= -B_1 \exp(2ikx), \\ A_2 &= t_m A_1 + r_m B_2, \\ B_1 &= t_m B_2 + r_m A_1, \\ B_2 &= -A_2 \exp(2ik(L-x)), \end{aligned}$$

where $k = 2\pi/\lambda$ is the wavenumber. These equations yield a transcendental equation for the resonant condition that can in principle be solved numerically. The solution can be simplified greatly by assuming that the losses in the membrane are negligible such that $|r_m|^2 + |t_m|^2 \approx 1$. With the approximation, the resonant length of the cavity can be written as

$$L_{res} = \frac{1}{k} \arctan\left(\frac{\cos(\phi_r) + |r_m|\cos(2kx)}{\sin(\phi_r) - |r_m|\sin(2kx)}\right), \tag{2.158}$$

where we have introduced the phase and amplitude of the reflection coefficient, $r_m = |r_m|\exp(i\phi_r)$. In principle, the resonant length is quite simple to connect to the resonance frequency. However, each length can host an infinite number of resonances. Nth such resonant wavenumber is then

$$k_{res} = \frac{N\pi}{L_{res}}. \tag{2.159}$$

Further, it is instructive to consider small correction to the resonant wavenumber such that

$$k_{res}(\delta x) = k_N + \delta k(\delta x), \tag{2.160}$$

and thus, the resonance frequency of the cavity modified by the membrane is

$$\omega_c = N\omega_{FSR} + \frac{\omega_{FSR}}{\pi}\left[\arccos\left((-1)^{N+1}|r_m|\cos(2k_N\delta x)\right) - \phi_r\right], \tag{2.161}$$

where ω_{FSR} is the free spectral range and k_N the *unperturbed* resonant wavenumber. The resulting shift for various membrane reflectivities is shown in figure 2.14.

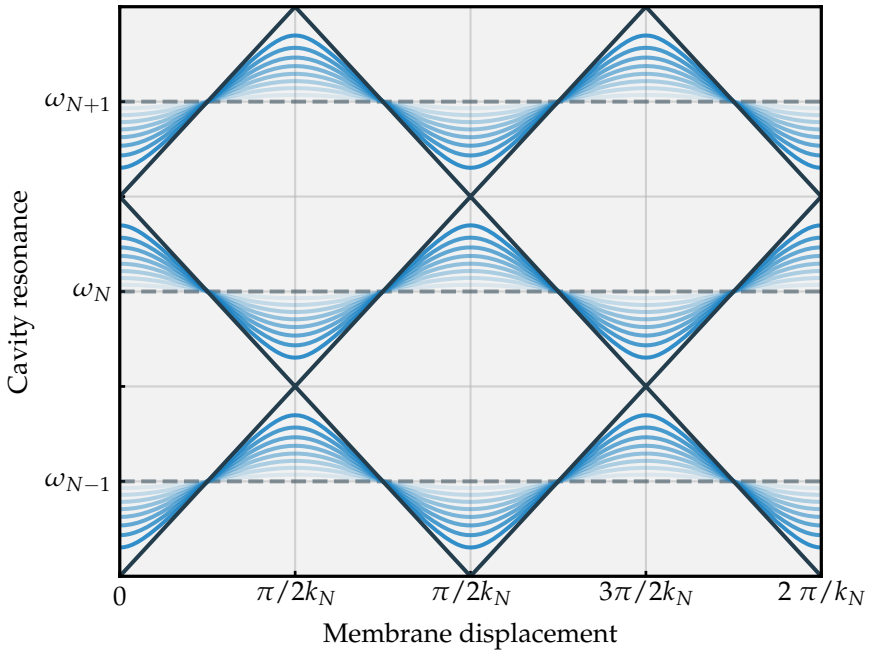

Figure 2.14: The membrane position modulates the cavity resonance frequency. The membrane reflectivity goes from 0 (dashed grey line) to 1 (solid dark gray line) with intermediate values plotted in blue such with reflectivity increasing from light to dark. When reflectivity is zero there is no modulation and when the membrane is perfectly reflective, we recover the usual linear cavity length dependence. For intermediate values, the mechanical motion shifts the frequency and allows for optomechanical coupling.

In the canonical optomechanical system with a movable end mirror, the relation between the cavity resonance and position is linear and thus the coupling strength is the same for all positions. However, for a membrane in the middle, the coupling strength is again proportional to the derivative of the cavity resonance that is no longer constant. Thus, the optomechanical coupling can be tuned by choosing a suitable membrane position. The membrane position also modifies the cavity linewidth and outcoupling. However, as the formal equations do not provide immediate enlightenment, we have chosen to only graph the results in figure 2.15.

2.8 FROM 2D TO 1D MOTION

Both experiments described later in the thesis utilize membrane resonator. Membranes are particularly interesting due to the extreme aspect ratio enabled by modern fabrication techniques. Thicknesses of few tens of nanometers are common and the

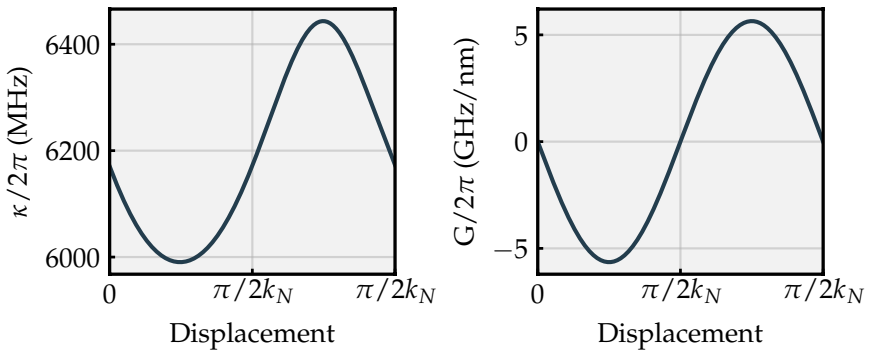

Figure 2.15: The position of the membrane modifies the linewidth of the cavity (left) and the optomechanical coupling (right). The values are calculated with $L \approx 49.3$ µm, $t_1^2 = 0.00034$, $t_2^2 = 0.0017$, $\phi = -\pi/2$, and $r_m^2 \approx 0.0013$.

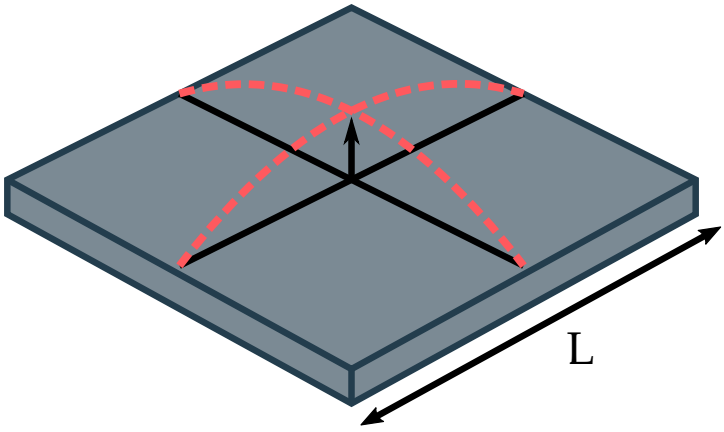

Figure 2.16: The membrane's motion can be modelled as a thin plate, such that the side length L is much larger than the thickness h. The sides are clamped, i.e. the displacement at the edge is zero. The vibration modes thus follow a wave equation.

side length can vary from a few hundred micrometers to a few millimeters. As a consequence, the membranes are light and thus very sensitive to external forces and at the same time, have a large surface area that accommodates easier optical or electrical coupling and offers large space for samples. Further, they can functionalized by e.g. depositing a metal layer on the membrane.

However, the discussion so far has assumed one dimensional motion that is hard to find outside of a textbook. To make use of the simple theoretical foundation of 1D motion, the task in any experimental system is to map the motion of the physical resonator to a one dimensional *effective* resonator with effective mass m_{eff} and effective spring constant k_{eff}.

For a membrane resonator, a good starting point is the eigen-

modes of a vibrating square plate clamped at the edges. We will make a number of simplifying assumptions. First, the plate thickness h is taken to be thin compared to its side length L_m and the in-plane motion is negligible. Neglecting bending losses[17] for the moment, the *out of plane* displacement $w_z(t,x,y)$ follows the wave equation[46]

$$\mathcal{T}\nabla^2 w_z(x,y,t) = \rho\frac{\partial^2}{\partial t^2}w_z(x,y,t), \tag{2.162}$$

where ρ is the density of the plate and $\mathcal{T}$ the in plane tensile stress. The equation is solved by separation of variables, where we look for a solution in the form of $w_z(t,x,y) = u_z(t)\phi(x,y)$. Assuming a square membrane, the spatial part of the solution is found to be

$$\phi_{i,j}(x,y) = \sin\left(\frac{i\pi x}{L_m}\right)\sin\left(\frac{j\pi y}{L_m}\right). \tag{2.163}$$

The main feature of such solution is that the spatial and temporal evolution are separate. Thus, $\phi_{i,j}(x,y)$ gives the shape of the motion and the time evolution of each point in the membrane is given by $u_z(t) = u_0\cos(\omega_m^{(i,j)}t)$, where $\omega_m^{(i,j)}$ is the frequency of the mode (i,j).

For a square membrane, the effective mass is in principle straightforward to find. We may calculate the total potential energy and compare it to a one dimensional resonator and choose the effective mass such that the expressions match. This is done by integrating over the membrane volume

$$U = \frac{\omega_m}{2}\int w_z^2(t,x,y)\,dV = \frac{\omega_m}{2}\frac{\rho L_m^2 h}{4}u_z(t)^2. \tag{2.164}$$

The membrane volume multiplied by density is simply the mass of the physical device $\rho L^2 h = m$ and we can thus map $m_{eff} = m/4$.

However, this becomes increasingly difficult for more complex geometries. As we will see, the typical membranes used in the experiment feature intricate designs. In such a situation, the effective mass is found by integrating over the mode shape using what is known as the Galerkin's method [47]

$$m_{eff} = \rho\int \phi_{i,j}(x,y)\,dV. \tag{2.165}$$

Conveniently, the method is implemented in most common finite element modelling (FEM) packages allowing us to estimate the effective masses of complicated structures already at the simulation stage.

17 The contribution in the equation is proportional to h^2 and thus very small for all membranes we'd like to consider.

2.8.1 *Practical membrane resonators and Dissipation engineering*

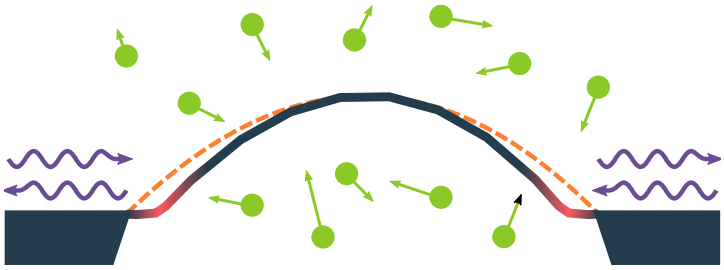

Figure 2.17: The main loss channels in a typical silicon nitride membrane resonator result from air molecule collisions i.e. gas damping, radiation to and from the substrate and bending losses due to sharp curvature near the clamping point. Here, the orange dashed line indicates the ideal displacement solution and the solid line is a more realistic representation of the membrane displacement. The red accents indicate area of sharp curvature.

While full understanding of membrane mechanics is not necessary to understand the following discussion nor is it the focus of the this thesis, we would like to make a couple of remarks about soft clamped silicon nitride membranes, especially on the main sources of loss. We already introduced the quality factor Q_m. More formally, it can be seen as the number of oscillations it takes to dissipate all energy in the resonator

$$Q = 2\pi \frac{W}{\Delta W}, \tag{2.166}$$

where W is to total energy and ΔW the amount of energy lost per oscillation. The losses, or the quality factor is further divided into different processes such that the total Q is the inverse sum of the individual quality factors associated with each loss channel

$$Q_{tot}^{-1} = \sum_i Q_i^{-1}. \tag{2.167}$$

A practical consequence of this formulation is that the dominating loss channel or the lowest quality factor determines the device's final Q[18].

Before exploring some loss mechanisms mechanisms, we would like to make a brief remark about *dissipation dilution*. We can further divide the total stored energy and the loss channels in equation 2.166 [47]

$$Q = 2\pi \frac{W_{tensile} + W_{elongation} + W_{bending}}{\Delta W_{elongation} + \Delta W_{bending}}. \tag{2.168}$$

18 For example, if $Q_1 = 10^4$ while $Q_2 = 10$, the total is $Q \approx 9.999$.

First, we assume that $W_{tensile}$, the energy needed to deflect the membrane against tension, is dominating, that is $W_{tensile} + W_{elongation} + W_{bending} \approx W_{tensile}$ and that the bending losses are equal to the the elongation losses, $Q_e = Q_b = Q_{intrinsic}$. The quality factor is then approximately

$$Q \approx \alpha_D Q_{intrinsic}, \tag{2.169}$$

where α_D is

$$\alpha_D = \left(\frac{W_b}{W_t} + \frac{W_e}{W_t} \right)^{-1}. \tag{2.170}$$

Since W_t dominates, the dilution factor α_D can become very large boosting the quality factor significantly.

In the case of silicon nitride membranes, the most relevant loss rates are the *bending*, *radiation* and *gas damping* losses. Gas damping is perhaps the most straightforward to consider. In atmosphere, gas molecules constantly bombard the membrane damping it. However, simply placing the membrane in a good vacuum, in practice $< 10^{-7}$ millibar for typical membranes in our experiments, renders gas damping negligible.

Second, the resonator must be anchored to some substrate[19]. The substrate also features mechanical modes some of which are near the modes of interest of the membrane and thus the mechanical energy easily propagates between the substrate and the membrane mode increasing the speed at which the membrane reaches equilibrium with the frame, that is the damping rate Γ_m increases. This mechanism is know as radiation loss. One strategy to reduce it is to embed the membrane inside a phononic crystal structure [49, 50]. The crystal then features a bandgap designed such that the membrane modes of interest lie within it. The propagation of vibrational modes within the bandgap is greatly suppressed and as consequence, the membrane modes are isolated from the environment. Such phononic shielding is quite versatile and also works for gigahertz optomechanical crystal resonators with the scaling and redesign of the pattern [51].

Finally, there are losses resulting from bending. At the anchoring point, the supporting structure forces zero displacement and as a consequence, the mode shape features a very sharp bend near the edge. This bending is one of the most significant loss channels in membrane resonators.

Relatively recently developed *soft-clamped* membrane resonators [52] work around this issue by engineering the membrane such that mode of interest decays gently before the clamp-

19 With the notable exception of levitated particles. Nowadays there is considerable interest in the levitated optomechanics and a recent review article provides an overview of the field [48].

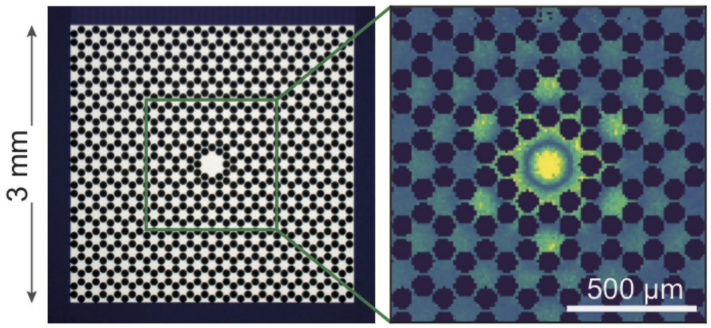

Figure 2.18: A first generation soft clamped silicon nitride membrane resonator. On the left, a photograph of a typical device shows the phononic crystal pattern isolating the mechanical modes localized in the defect. The measured displacement on the right confirms that the defect mode decays very quickly before reaching the frame. Adapter from [52]

ing point and avoids any sharp bends. This is achieved by patterning a phononic crystal pattern on the membrane and introducing a larger pad usually called a defect since it breaks the symmetry of the pattern as shown in figure 2.18. The pattern then plays double duty. On hand it isolates the defect modes from the environment and on the other hand, it localises the motion to the defect. As a consequence, quality factors of hundreds of millions are routinely fabricated at megahertz frequencies. The technique also works in doubly clamped beams localizing motion to the center [53].

2.9 MEASURING MECHANICAL MOTION

In the previous discussion, we simply stated, that we will measure the phase fluctuations of the output field. This however, creates a bit of a practical conundrum. Photodiodes will only measure the power of the incoming laser beam. The power indeed oscillates with the laser frequency, but that is typically in the Terahertz range and thus outside the bandwidth of current photodetectors. However, what we can do, is to beat the output field with a reference beam, usually referred to as the *local oscillator* (LO), such that the beat note between them depends on the relative phase of the two beams. This then transforms any phase fluctuations originating from the cavity to comparatively slow[20] amplitude fluctuations that a typical photodetector can

20 Order of mechanical frequency, typically between 1 and 1.5 MHz in our experiments, so the slowness is indeed only relative.

pick up with ease. This is the idea behind homodyne or heterodyne detection. In the experiments in this thesis, we use either direct detection or homodyne. Let us then explore the latter in more details.

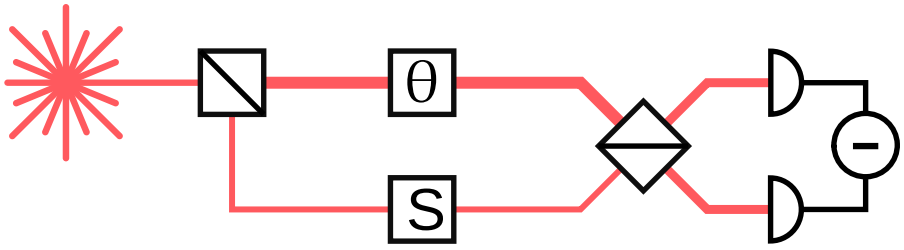

Figure 2.19: A Mach-Zehnder interferometer. The laser source on the left is split into a strong LO travelling on top and a weaker probe beam on the bottom. The probe beam passes through the system of interest S and is recombined with the LO on a 50:50 beamsplitter. The phase θ of the LO is controlled such that quadrature of interest $\hat{X}^{\theta}$ is measured. The outputs of the beamsplitter are measured on two photodiodes (hence the name *balanced homodyne measurement*) and their difference produces the photocurrent of interest.

In a homodyne measurement, we typically split the source into two beams, the LO and the probe beam. The ratio of powers is such that the LO is much stronger than the probe. In a typical interferometer setup, often in our chase in the Mach-Zehnder configuration, the LO travels trough a *reference arm* and the probe beam passes through or reflects from the system of interest in the *probe arm*. The beams are then combined in a 50:50 beam splitter and measured on two photodiodes producing currents I_+ and I_-. In principle, a singled diode detection already has all of the information needed, but measuring the sum of positive and negative photocurrents suppresses classical amplitude noise allowing for a more sensitive measurement. A typical scheme is sketched in figure 2.19.

Mathematically, we introduce another field operator, a_{LO} such that $|a_{LO}| = \alpha_{LO} \gg |a_{out}|$. The large amplitude allows us to treat the field classically. The final field, after interaction of the LO and probe is thus

$$E_{\pm} = \frac{1}{\sqrt{2}}\left((\alpha_{LO} \pm \hat{a}_{out})e^{-i\omega_L t}) + (\alpha^*_{LO} \pm \hat{a}^{\dagger}_{out})e^{-i\omega_L t})\right). \tag{2.171}$$

The measured power and thus, the measured photocurrent is then the square norm of this field. The photodetector has a limited bandwidth and thus we neglect all fast oscillating terms

and are left with

$$I_{\pm} = |\alpha_{LO}|^2 \pm \left(\alpha_{LO}\hat{a}_{out} + \alpha_{LO}^{*}\hat{a}_{out}^{\dagger}\right) + \frac{1}{2}\left(\hat{a}_{out}\hat{a}_{out}^{\dagger} + \hat{a}_{out}^{\dagger}\hat{a}_{out}\right) \tag{2.172}$$

In *balanced homodyne*, where we measured the difference of photocurrents $I_+ - I_-$, the only surviving term is

$$I = 2\alpha_{LO}e^{i\theta}\left(\hat{a}_{out} + \hat{a}\right), \tag{2.173}$$

$$= 2\sqrt{2}\alpha_{LO}\hat{X}_{out}^{\theta}, \tag{2.174}$$

where we have written the LO as $\alpha_{LO} = |\alpha_{LO}|e^{i\theta}$, with θ being the LO phase and have introduced the arbitrary quadrature

$$\hat{X}_{out}^{\theta} = \frac{1}{\sqrt{2}}\left(\hat{a}e^{-i\theta} + \hat{a}^{\dagger}e^{i\theta}\right). \tag{2.175}$$

If we set $\theta = \pi/2$, we recover the phase quadrature. Alternatively, if $\theta = 0$, we measure the amplitude.

The interesting feature to not in equation 2.174 is that we measure only the output signal from the cavity, but the signal strength is multiplied by the LO amplitude! Hence, the homodyne measurement not only allows for measurement of arbitrary quadrature of light, but also increases the signal strength. It should be noted however, that the enhancement applies to the *entire* output field, including the imprecision and QBA terms.

3 MRI

In this chapter, we will cover the effort to create an integrated opto-electromechanical transducer for clinical MRI machines. We start with an overview of conventional MRI technology, make a few remarks about the theoretical background and cover the results for the fabricated devices. The author's involvement was mostly in characterizing and measuring the devices. This chapter will be relatively concise, highlighting only the key measurements and results. For a more in depth treatment, we recommend studying [28] or [54] and [55]

3.1 Overview of optomechanical transduction efforts

As already hinted in earlier sections, many of the optomechanical transduction efforts aim specifically to convert a microwave photon originating from a superconducting qubit to optical frequencies to enable long distance quantum networking. This is perhaps not an unreasonable focus, given the steady progress in superconducting quantum computing exemplified by demonstration of quantum supremacy already two years ago[56][1].

However, there is room for improvement in the classical domain. Measurements based on nuclear magnetic resonance (NMR), the most well known example being magnetic resonance imaging (MRI), rely on being able to detect faint magnetic fields. The typical detection chain is based on electronic amplifiers. However, the electronic circuits and cables are susceptible to magnetic fields and crosstalk. This means using stronger magnetic fields or multiple coils is challenging. In contrast, optical fibers are immune to external magnetic fields, lightweight and do not suffer from cross talk. Further, the losses in fibers are much smaller compared to radio frequency electrical cables. In principle, this would allow placing the analysis unit far away from the scanner and avoid having any signal processing equipment near the strong magnetic field

There have been a few demonstrations of purely optical detection schemes for NMR signals. NV-center-based magnetometry features impressive sensitivity and spatial resolution but is limited to small samples[58, 59]. Similarly, magnetic resonance force microscopy (MRFM) can achieve sub-nanometer resolution but is limited to very small samples[60, 61]. Vapor

1 Though not without some sour grapes from competition[57].

cell magnetometers are low noise, but at higher frequencies, conventional electronics match and exceed their performance[62, 63]. In contrast, optomechanical detection is frequency agnostic, compatible with telecom wavelengths, directly compatible with existing detection coils and, leveraging interferometric readout, very sensitive.

In fact, an experiment based on an earlier proposal[64] from Copenhagen demonstrated optical readout of radio frequency signals and could in principle reach noise temperature down to 4K[65]. Getting much lower noise temperature with an electric amplifier typically requires cooling the device down to cryogenic temperatures. However, despite impressive performance the device was otherwise limited. DC biasing meant that only signals at the mechanical frequency could be picked up and the bandwidth was limited to 4 kHz. Since then, optomechanical transduction has been demonstrated for NMR signals using AC bias[66, 67] although with limited bandwidth and the noise performance was still worse compared to conventional electronic amplifiers. It is possible to boost the detection bandwith by using multiple mechanical modes, but the first proof of principle experiment featured less than ideal sensitivity[68].

All of the aforementioned experiments are comparatively complex and require large amounts of space. Our objective was thus to integrate both the optical cavity and electrodes into a single chip and use as simple and affordable optical setup as possible. Before moving on to the experiment, let us briefly cover the basic principle of MRI.

3.2 BRIEF OVERVIEW OF MAGNETIC RESONANCE IMAGING

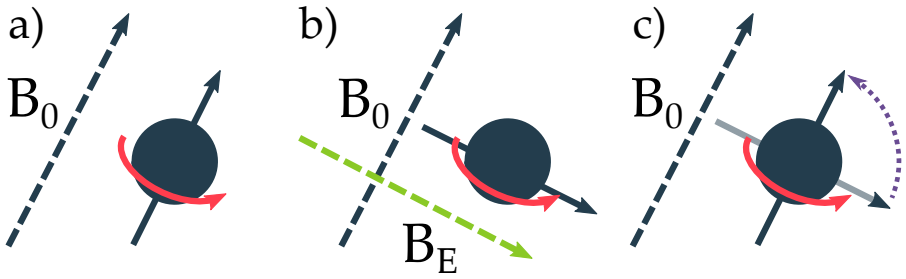

Figure 3.1: The basic sequence of an NMR process. a) The spins of nuclei align along a strong external field B_0. b) A transmit pulse B_E, perpendicular to the main field excites the spins. c) The spins continue to precess around B_0 gradually returning to the ground state. The precession creates a magnetic field perpendicular to B_0 that can be measured. In the figure, the red arrow indicates the spin precession and the dark gray arrow the spin axis.

Magnetic resonance imaging is a well established technology, perhaps most familiar in a medical setting. While it's technical details are somewhat unnecessary for appreciation of the electro-optomechanical device, we nevertheless provide a brief recapitulation of the main principle mostly based on treatment in [69]. The core idea of MRI is to measure a radio frequency signal originating from nuclear magnetic resonance (NRM).

The principle is simple. In a strong external magnetic fields the nuclear spins in the sample align along the field. In a magnetic field, the spins will also precess around the field vector at frequency dependant on the particular nucleus and the strength of the external magnetic field, $\omega_n = \gamma B_0$, where γ is the gyromagnetic ratio[2] and B_0 the magnitude of the magnetic field. The scanner our device is designed for detects the nuclear spin of C^{13} in a 3T field such that the precession frequency is approximately 32 MHz.

An excitation pulse is used to flip the spins perpendicular to the external field B_0. Once the pulse passes, the spins will relax back to the initial, aligned arrangement. The precession of the spins creates an oscillating magnetic field perpendicular to $\vec{B}_0$. As the spins relax the magnitude of this field also drops.

The imaging algorithms are much more complex and don't really add much to the discussion. However, we will make a brief comment about gradient fields. Besides the excitation field and the constant external field, MRI scanners employ spatially changing fields. The purpose of the field is to make sure spins in a specific area of the sample are excited thus distinguishing different layers of the sample. Since the target frequency will change slightly from the one set by the constant field, the amplifier on the pick-up circuit needs to have sufficient bandwidth.

3.3 ELECTRO-OPTOMECHANICAL TRANSDUCTION FOR MRI

Within the field of optomechanics, both electro- and optomechanical experiments are well represented. Given the multitude of technical platforms, one can easily imagine that the mechanical resonator in an electromechanical system could also be part of an optical device. One example would be a membrane resonator acting at the same time as one side of a parallel plate capacitor and the movable end mirror of an optical cavity. In such a system we the radio frequency signal drives the motion of the mechanical resonator and resonator's motion can be read out optically.

2 This is the only time γ is used to refer to the gyromagnetic ratio. Most previous and subsequent uses of γ will refer to decay rates, unless very, very clearly noted.

3.3.1 *Electromechanical system and cavity readout*

In the very beginning, we briefly mentioned that electrical resonators behave identically to optical ones with resonance frequency determined by $\omega_{LC} = 1/\sqrt{LC}$, where subscript LC refers to the the fact that, in a lumped element model, the electrical resonator consists of an inductor and a capacitor.

Before delving into the electromechanical theory, let us sketch the device. First, an aluminium membrane forms the end mirror of an optical cavity. However, the cavity has a very large linewidth owing to the only approximately 90% reflectivity of the membrane. Thus, we omit any dynamical effects arising from the optics. Instead, dynamics are fully determined by the *electro*mechanical interaction and we only consider the motion readout via the cavity. In the following, any variables are understood to include any steady state effects arising from the *opto*mechanical interaction. To remind ourselves of this, we employ subscript om in the variables. For example, ω_{om} is to be understood to include the optical frequency shift $\omega_{om} = \omega_m + \omega_{dba}$. The membrane also forms one side of a parallel plate capacitor. The device is then connected to an LC circuit together with a detection coil. We have further included a tunable capacitor in the circuit to match the electrical resonance frequency to a particular device realization. Without further ado, the equations of motion for charge q and position x can be written as

$$m\ddot{x} = -m\omega_{om}^2 x - m\Gamma_{om}\dot{x} + F_m - \frac{q^2}{m}\frac{\partial C(x)}{\partial x}, \tag{3.1}$$

$$L\ddot{q} = -\frac{q}{C(x)} - L\Gamma_{LC}\dot{q} + F_e, \tag{3.2}$$

where we have already eliminated the conjugate variables momentum p and flux φ via

$$p = m\dot{x}, \tag{3.3}$$

$$\varphi = L\dot{q}. \tag{3.4}$$

Up to the last term, the equation for position looks identical to one found in the earlier section[3] except the optical force is replaced by a term proportional to the square of charge and a derivative of the capacitance $C(x)$, where we have explicitly noted the position dependence. The second equation for charge q should also look familiar. It contains similar terms as the equation for the optical field, but adapted for an electrical resonator. The electromotive force F_e contains all forces acting on

3 up to ultimately meaningless sign convention.

the electrical resonator, namely the drive V_D, the signal V_S and the electrical Johnson noise V_J. In the equations, we have also introduced the inductance L and the electrical decay rate Γ_{LC} of the circuit.

Since the solution of the equations follows similar steps as outlined for optomechanical system in the theory chapter, we will omit most of the intermediate steps and simply state the most relevant conclusions.

To enable the electromechanical coupling, the resonant circuit needs a driving voltage, frequently called bias. In principle, both DC and AC biases work and enable transduction of signals. However, when the system is biased with a DC voltage, it is sensitive only to signals at the mechanical frequency, since this signal needs to to modulate the mechanical motion. Already at very moderate quality factor, the mechanical response away from the resonance decays very fast. An AC bias can work around this issue. The idea is, that instead of the signal itself, the *beat note* between the bias frequency and the signal frequency will drive the membrane. A single device can then be tuned to pick up signals over a large frequency range and the mechanical resonator can be designed more freely, making this kind of scheme much more convenient and versatile.

Here, we only consider the AC bias. The theoretical treatment is broadly similar for both cases with some subtle differences. Simply taking the limit $\omega_D \to 0$ recovers the DC bias result without much trouble.

3.3.2 *Necessity for AC bias*

To enable the beat note modulation of the mechanical resonator, we drive the circuit with a voltage oscillating at frequency chosen such that the sum of the drive ω_D and the mechanical frequency ω_{om} equals the signal frequency[4] $\omega_{LC} = \omega_D + \omega_{om}$.

Let us then write the bias voltage as

$$V_{AC} = V_0 \cos(\omega_D t + \theta), \tag{3.5}$$

where V_0 is the drive amplitude and θ a phase term. The drive frequency is directly translated to the charge such that

$$q = q_0 \cos(\omega_D t) + \delta q, \tag{3.6}$$

where δq is a small charge fluctuation around the steady state value q_0. Similarly, the position is linearized $x = x_0 + \delta x$.

4 We will use the terms signal frequency and LC-resonator frequency somewhat interchangeably. They are distinct, but to detect the signal, they must coincide $\omega_{LC} = \omega_{signal}$

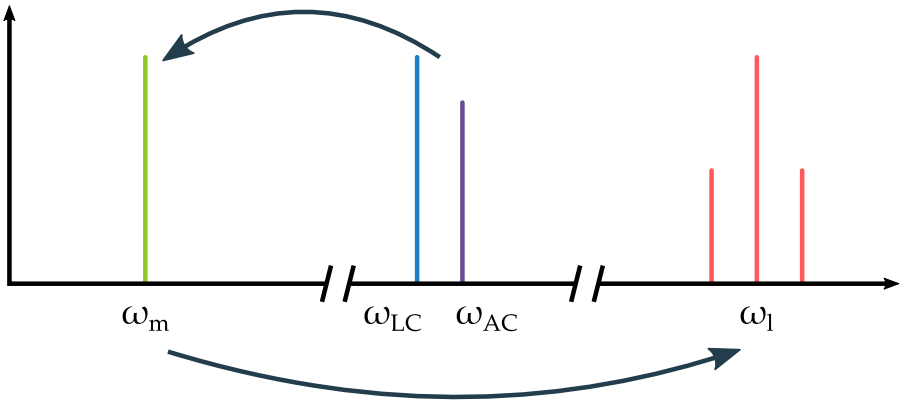

Figure 3.2: A conceptual sketch of transduction between RF and optical frequencies. The beat note between the AC bias at ω_{AC} and the signal at ω_{LC} drives the membrane at ω_m. The mechanical motion then creates sidebands of frequency ω_m on the probe laser at ω_l that can be picked up with a standard photodetector. Without the beat note between the AC bias and the signal, the mechanical frequency would have to coincide with the signal frequency to allow for transduction.

The end result is two equations

$$\chi_e(\Omega)\delta q = F_e + V_{signal} + G_{em}^{AC}\left[\delta x(\Omega+\omega_D) + \delta x(\Omega-\omega_D)\right] \quad (3.7)$$

$$\chi_{om}(\Omega)\delta x = F_m + G_{em}^{AC}\left[\delta q(\Omega+\omega_D) + \delta q(\Omega-\omega_D)\right], \quad (3.8)$$

where we have included the electrical and mechanical susceptibilities χ_e and χ_{om}. The equations look again familiar, but now include troubling terms at frequencies $\Omega \pm \omega_D$.Tto get rid of them, we note the form of the susceptibilities and consider the motion at ω_{om} and charge at ω_{LC}. Mechanical response away from ω_{om} is very modest. Setting $\Omega = \omega_{LC}$ in the first equation the position terms become $\delta x(\omega_{LC}+\omega_{LC}-\omega_{om}) = \delta x(2\Omega_{LC}-\omega_{om})$ and $\delta x(\omega_{LC}-\omega_{LC}+\omega_{om}) = \delta x(\omega_{om})$. The first term is far away from resonance and thus can be safely neglected. Similarly, for the second equation evaluated at $\Omega = \omega_{om}$, only the term $\delta q(\omega_{om}+\omega_{LC}-\omega_{om}) = \delta q(\omega_{LC})$ survives.

In the equations, we have also included the electromechanical coupling

$$G_{em}^{AC} = \frac{\bar{q}_0}{2C}\frac{\partial C(x)}{\partial \delta x}, \quad (3.9)$$

where $\bar{q}_0$ denotes the *average* charge. It is also useful to define the *electromechanical cooperativity* that helps us gauge the strength of the eletromechanical coupling

$$C_e = \frac{G_{em}^2}{mL\omega_m\omega_{LC}\Gamma_m\Gamma_{LC}}. \quad (3.10)$$

The broadened mechanical resonance can then be written as

$$\Gamma_{m,e} = \Gamma_m(1 + C_e), \tag{3.11}$$

and allow us to easily determine the cooperativity by measuring the mechanical linewidth.

3.3.3 *Optimal cooperativity*

With the cooperativity, the total measured optical output spectrum in voltage units is then

$$S_{VV}^{out}(\omega) = S_s(\omega_{LC}) + 4k_b L\Gamma_{LC}\left(T_0 + \frac{T_m\omega_{LC}}{C\omega_m} + \frac{T_o(1+C)^2\omega_{LC}}{C\omega_m}\right), \tag{3.12}$$

where T_0 is the bath or the environment temperature, and we have defined the optical noise as

$$T_o = \frac{m\Gamma_{om}\omega_m^2}{k_B\bar{n}}\left(\frac{R_0}{R_0'}\right)^2, \tag{3.13}$$

with $\bar{n}$ being the photon number, R_0 the reflectivity of the cavity and R_0' the cavity slope, i.e. the derivative of the reflectivity.

In the total noise equation, the first term corresponds to the signal we wish to detect and the second term contains all of the noise terms in the system. Strikingly, there is an optimum operating point, or an *optimal cooperativity* that minimizes the added noise or, equivalently, maximizes the signal to noise in transduction

$$C_{opt} = \sqrt{1 + \frac{T_m}{T_o}} = \sqrt{1 + \frac{S_{xx}(\omega_m)}{S_{xx}^{opt}}}. \tag{3.14}$$

Here, $\bar{S}_{xx}(\omega_m)$ is the peak of the thermally driven mechanical response and $\bar{S}_{xx}^{opt}$ corresponds to the optical shot noise floor as an equivalent displacement spectrum. The optimal cooperativity for a given device can then be easily estimated by simply measuring a thermal spectrum and determining the ratio of the peak mechanical response to the background noise. For most of the integrated devices, we found optimal values between 30 and 40.

3.4 INTEGRATED DEVICE AND MEASUREMENT SCHEME

As one easily imagines, creating a single chip integrating optical cavity, membrane and capacitors is a highly involved nanofabrication project. While the author had no involvement in the

design process, we have included a simplified fabrication flow. For a more detailed exploration of the development and fabrication process, we recommend [28] or [54]. The simplified fabrication flow is also shown in figure 3.3.

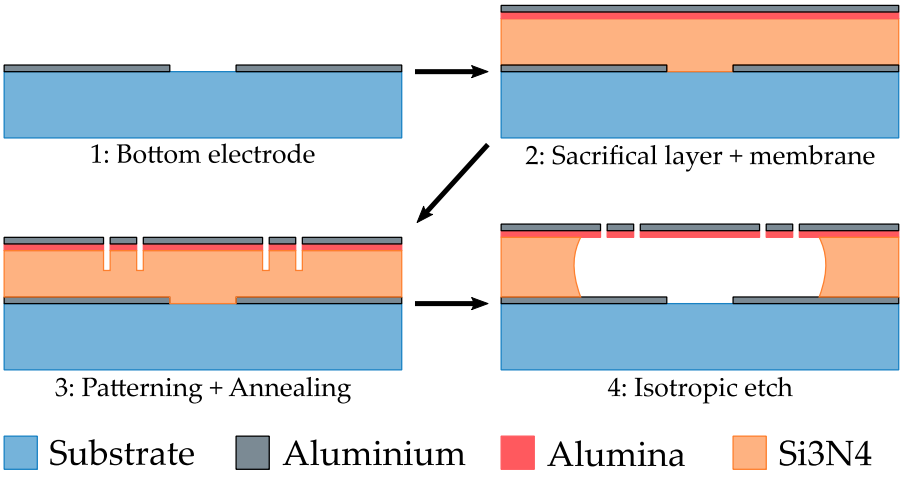

Figure 3.3: A simplified fabrication flow. The steps are elaborated on in the main text.

The entire device was fabricated in a 10-100 class cleanroom[5] using only standard techniques. The starting point of the process is a fused silica wafer with a protective alumina (ALD Al_2O_3) layer deposited on top. Then, the bottom electrodes, that will form one part of the mechanically compliant capacitor are patterned on the wafer with UV lithography and lift-off (step 1). Then, a sacrificial PECVD nitride layer is deposited on top. The layer is approximately 500 nm thick and will set the length of the optical cavity.

The membrane is then deposited on the sacrificial layer in two stages (step 2). First, 50 nm of alumina is deposited followed by 100 nm of Aluminium patterned with lift-off. We then perforate the membrane stack with a dry-etch to define a circular membrane. At this stage, the device is annealed to make sure the membrane has ideal tensile stress (step 3). As the final stage, the sacrificial layer is etched away releasing the membrane and forming the optical cavity. The target length of the optical cavity is approximately one wavelength at 1064 nm (step 4).

The wafer is then diced to 5 by 5 millimetre chips and individual devices are wire bonded into standard IC sockets for ease of use. We added a switch to the socket to short the membrane capacitor when the device was not in use. The device was very sensitive to static charge but shorting the capacitor was very effective in protecting the device. For optical access, we further

5 DTU Danchip

attach a GRIN lens on the device chip to focus the input beam into the optical cavity. The final assembly steps and the compete device is shown in figure 3.4.

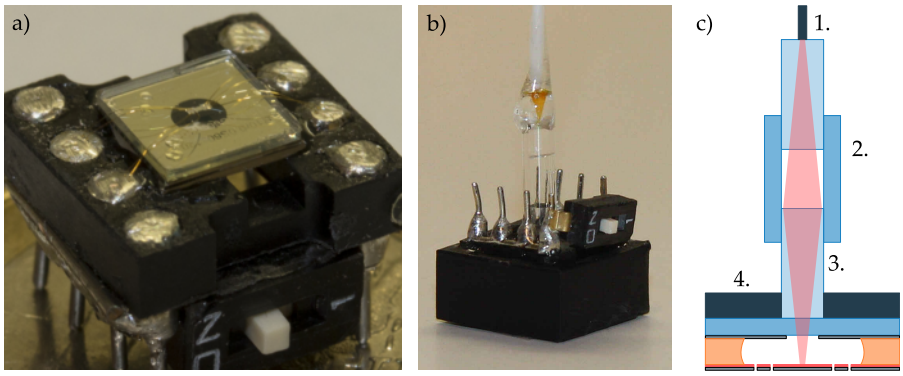

Figure 3.4: a) The diced chip is wire bonded on a standard IC socket for easy connectivity. This photo shows the backside of the cavity and the switch used to short the device when not in use. b) Another view of the device, this time with the fiber already attached. The membrane is protected by a custom made cap on the socket glued in place. The side of the socket is approximately 1 cm. c) A schematic of the coupling mechanism. The light is delivered via a fiber terminated in a ferrule (1.). The ferrule is attached in a guiding tube (2.) with a GRIN lens (3.) on the other end. The GRIN lens is positioned on the cavity with a Silicon guide on the chip. The coupling to the cavity is optimized by tuning the distance between the GRIN lens and the fiber ferrule. Once optimum point is found, the fiber is glued in place.

The measurement scheme is purposefully kept simple and affordable. The probe laser is comparatively cheap diode laser at 1064 nm. The wavelength choice is to some extent arbitrary, but for the first proof of principle devices, we chose a wavelength where large amount of equipment was already available. For example, a telecom wavelength near 1550 nm or 1310 nm would be a prudent choice since there is a good amount amount of affordable components available and the reflectivity of the aluminium membrane would also be higher.

The optical setup consists of an isolator to protect the diode from backscattering and a single circulator. The setup is completely fiber based for ease of handling and adaptability to different environments. For example, the ultimate environment of a clinical MRI scanner does not afford for a complicated optical setup.

The probe light enters the optical cavity via the input fiber aligned to the GRIN lens on the device. The reflected light is collected with the same fiber and the circulator diverts the reflection to a single diode photodetector, where we measure the amplitude fluctuations.

3.5 CHARACTERIZATION

With the devices ready, there are number of characterization checks to be done to make sure that the parameters are suitable and that the behaviour is as expected. Before measuring the transduction performance, we need to measure mechanical properties of the membrane resonator, any dynamical optical effects at the operating power and the effect of the bias voltage.

3.5.1 *Mechanical properties*

The initial mechanical characterization is done with a commercial vibrometer. The measurement is good enough to see if the mechanical frequency lands near the target frequency and if the quality factor is sufficient. We target $\omega_m/2\pi$ between 1 and 1.3 megahertz and quality factor of approximately 10^4.

More accurate measurements are performed in a custom built Michelson interferometer where the probe laser measures the thermal motion of the membrane. The device is placed in a vacuum chamber at pressure below 10^{-5} millibars. The design of the integrated chip enables bypassing the cavity and probing the thermally driven motion of the membrane without dynamical optical effects. The linewidth is found by fitting a Lorentzian function to the measured thermal motion spectrum. The bandwidth of the spectrum analyzer module of the lock in amplifier easily resolves the linewidth[6] and for most devices the vibrometer measurements match the values found in the interferometer.

According to the electromechanical theory, the resonance frequency of the membrane is proportional to the applied bias voltage, $\omega_m \propto V_{DC}^2$ such that both positive and negative voltage shift the frequency down. However, we observe that the highest frequency is offset from zero bias and rather happens at a moderate positive bias. We attribute this shift to trapped charges in the device. The effect is shown in figure 3.5.

We have also observed that the mechanical quality factor and frequency are stable over a period of at least a year. This is particularly important if the device should become a component in a clinical MRI scanner.

6 This is a very important consideration. To accurately measure the linewidth from the spectrum, the bandwidth or the binning of the spectrum analyzer should be significantly smaller than the measured linewidth.

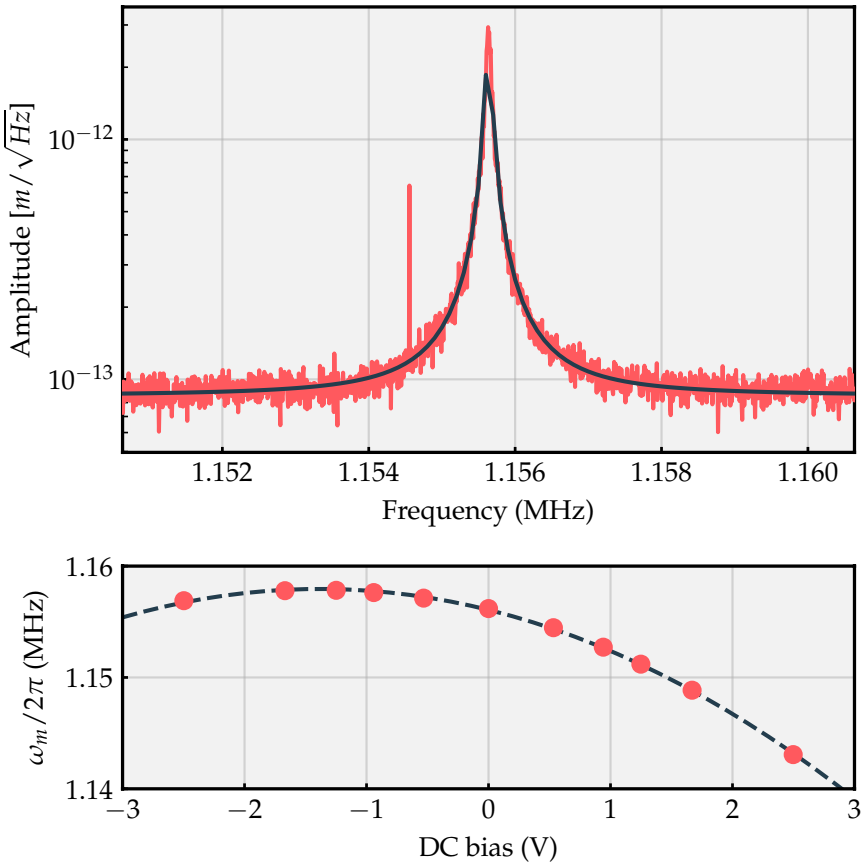

Figure 3.5: A typical mechanical response driven only by the thermal noise (red line) and a Lorentzian fit (gray line). The resonance frequency is proportional to the square of the applied DC bias voltage. However, the maximum is not at 0 volts as expected, but shifted to approximately -1.2 V. This is due to trapped charges in the electrodes or the membrane presumably from the fabrication process.

3.5.2 *Optical effects*

The optical cavity is very low finesse. The reflectivities of the membrane and the end mirrors are approximately 80% at the chosen wavelength. This means, that any dynamical backaction effects should be negligible. However, we observe a linear broadening of the mechanical linewidth with increased probe power[7] The effect is consistent with photothermal backaction. We extrapolate the intrinsic mechanical linewidth $\Gamma_m/2\pi = 124$ Hz without optical or electrical broadening and the optically broadened linewidth at the typical operating power of approximately 700 µW input to the incoupling fiber of $\Gamma_{om}/2\pi = 234$ Hz.

7 On some devices, the probe *decreases* the linewidth. The direction of the effect depends on the exact cavity length.

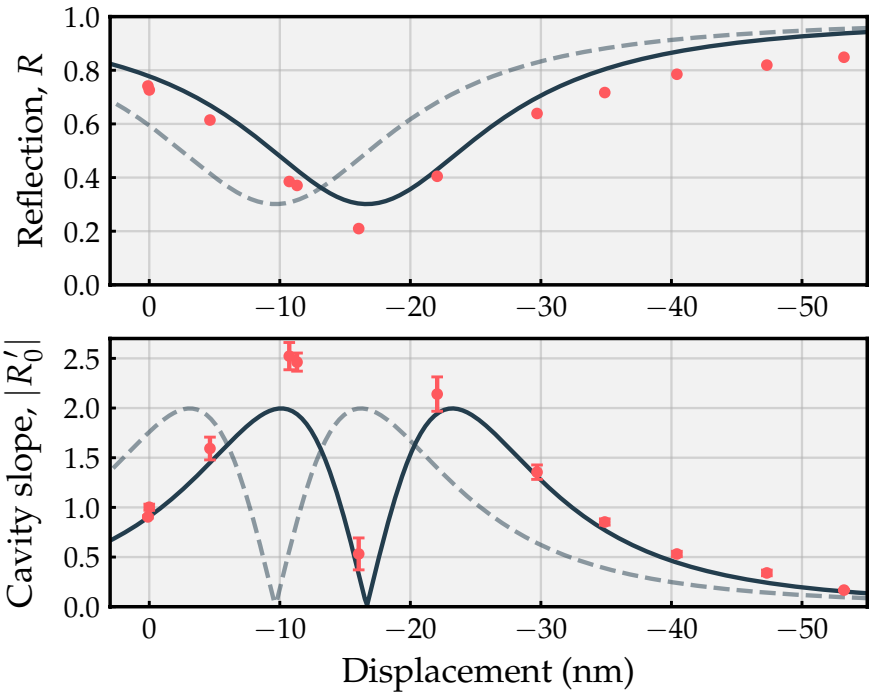

Figure 3.6: The bias causes a static displacement of the membrane that in turn changes the length of the cavity. The voltage bias is converted to displacement of the membrane and the measured reflectivity R of the cavity is fitted against the compared against the predicted cavity reflection (solid lines). The dashed lines indicate values expected from the fabrication parameters. The measurement agrees with the model, but indicates that there is an approximately 10 nm shift compared to the planned cavity.

The bias voltage also causes a static membrane displacement and thus also changes the cavity length. This can be seen as a change in the cavity reflectivity R. Seeing the cavity response also allows us to determine how the probe laser is detuned from the cavity.

3.5.3 *LC circuit*

From an electrical point of view, the device is a simple capacitor and as such must be included in an LC resonant circuit to enable the electromechanical interaction. However, the presence of the AC bias complicates the circuit design. To properly detect a signal, the resonant frequency of the LC circuit must coincide with the signal frequency. However, an AC bias near the LC resonance would load the circuit degrading its quality factor. To preserve the circuit Q, the design mechanical frequency is above 1 MHz such that the drive frequency is sufficiently different

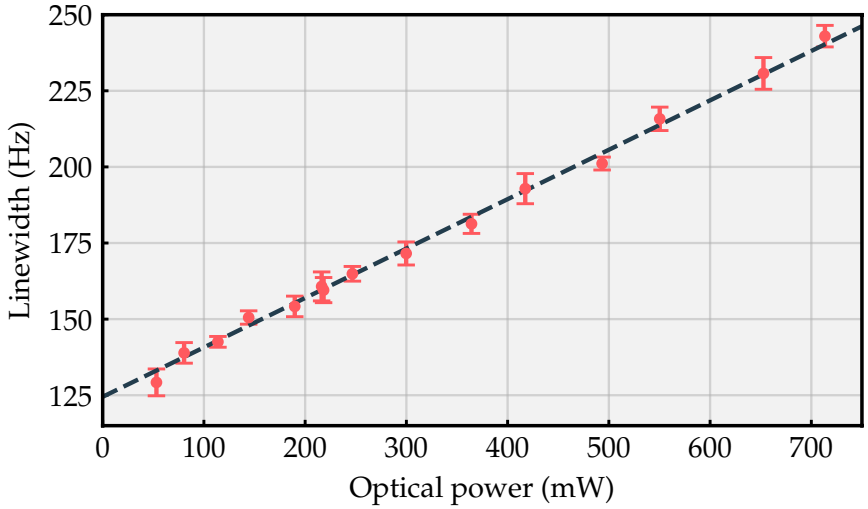

Figure 3.7: The photothermal backaction damps the mechanical oscillator. The broadened linewidth can also be presented as the effective temperature of the mechanical motion. Here, we infer intrinsic linewidth of approximately 124 Hz and the photohermal, backaction cools the resonators effective temperature to approximately 150 K.

from the circuit resonance. We have further included a bandpass filter on the AC drive port to reduce any noise in the drive away from the carrier. In the circuit, there is also a tunable capacitor to match the resonant frequency to the signal.

We construct a full scattering parameter model of the circuit with a Markov Chain Monte Carlo simulation. The agreement between model and measured response is very good and allows us to model the currents in the circuit to a good degree of accuracy.

3.5.4 *AC transduction setup*

Given that the device is planned to detect faint magnetic fields, it is not surprising that it is extremely sensitive to environmental noise. Thus, to measure the transduction noise, the device is shielded by a large aluminium box. The frequency of the LC circuit is high enough, that a thin layer of metal is enough to shield the device and the enclosure is not very sensitive to small gaps in the shielding.

The circuit with the transducer chip is placed in a glass domed vacuum chamber. The glass dome is necessary in order for the signal not to dissipate in the metal structure. The shielding is also chosen such, that there is a good amount of space, approximately 20 cm, around the coils. The probe light is deliv-

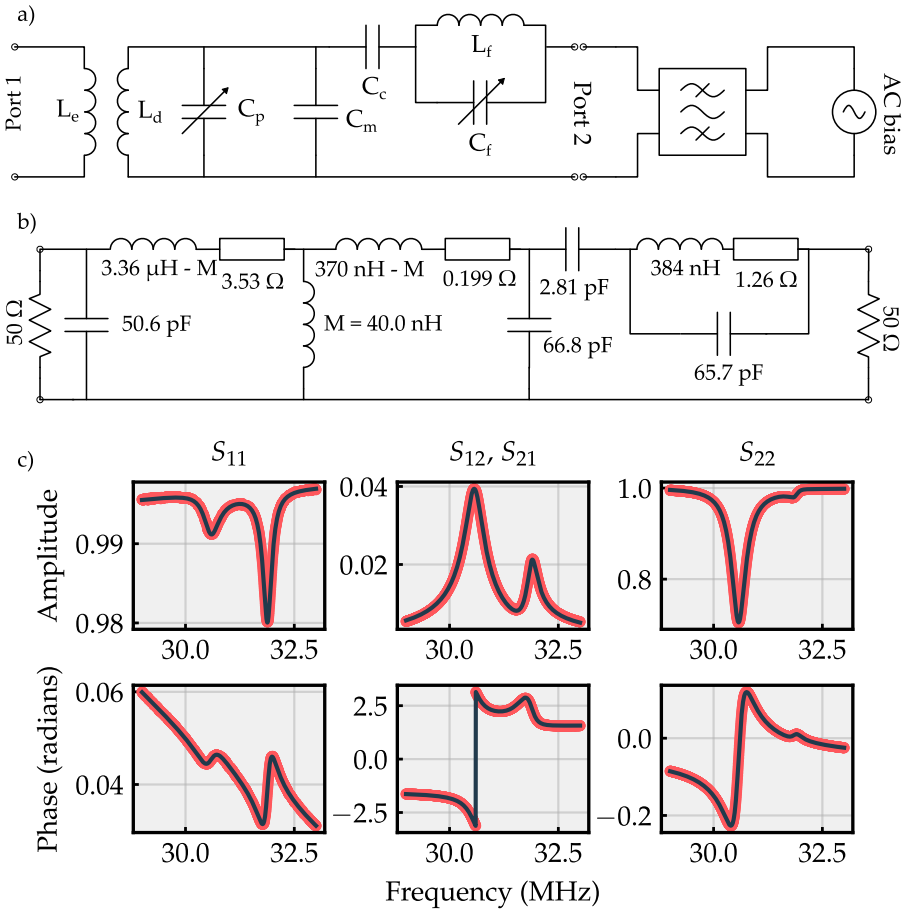

Figure 3.8: a) The circuit diagram of the detection circuit. The AC bias is heavily filtered. There is tunable capacitor C_p in parallel with the membrane C_m to match the frequency of the LC circuit to the detected signal. b) The fitted values for the circuit components. c) There is an excellent agreement between the measured scattering parameters (red poitns) and the fitted model (gray line). Adapted from [54]

ered via a custom fiber feedthrough based on a Teflon ferrule[70]. The AC bias is delivered through a commercial feedtrough. The chamber is kept under pressure of much less than 10^{-3} mbar. The pressure reading is somewhat uncertain, since the vacuum gauge is approximately 1 meter away from the device, connected via KF40 vacuum hose. The gauge reads a much lower pressure, but based on the measured mechanical spectrum and experience with the device, we infer an upper bound for the pressure near the transducer.

To determine the transduction performance, a custom built excitation coil is placed outside of the glass dome, near the detection coil to provide a test signal.

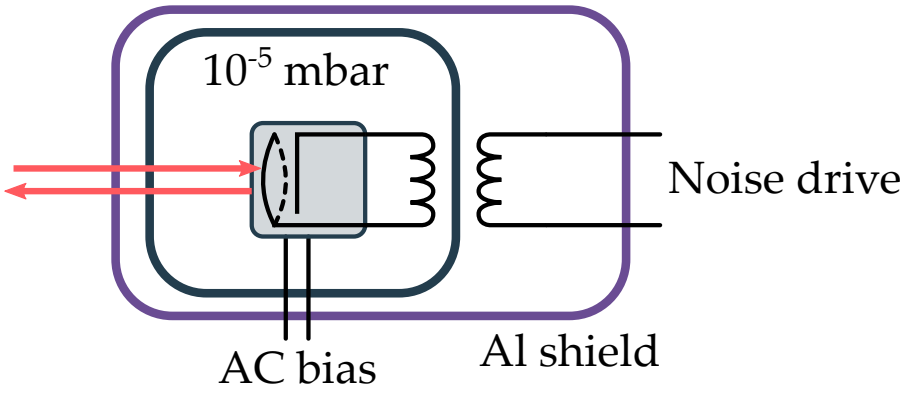

Figure 3.9: A simplified schematic of the noise measurement. The transducer chip together with the LC circuit is inside a vacuum chamber with a glass dome such that the noise drive can be applied via an external coil. The entire vacuum chamber is inside an aluminium box to shield the device from environmental noise.

3.5.5 *Transduction noise*

The most crucial question for the transduction performance is of course the added noise, or the noise temperature of the device. However, in a transduction measurement, we only have access to the driven mechanical spectrum that contains both the intrinsic noise of the device and the noise in the driving field. To separate the noise sources, we perform a Y-factor like measurement. In the typical Y-factor measurement, an amplifier is fed Johnson noise originating from a resistor at different temperatures. Since the amplifier noise is constant, the source noise can be extrapolated away and the amplifier noise temperature extracted[71].

In a similar fashion, we inject varying levels of voltage noise to the circuit. The driven response of the mechanical response is then proportional to this noise and contains the constant, device term. Very loosely, $T_N = T_D + P_{in}T_J$, where T_D is the intrinsic transducer noise and T_J the Johnson noise proportional to the input power P_{in}. Once the Johnson noise is extrapolated away, the remaining transducer noise is easily separated into optical noise and mechanical noise due to different spectral shapes - flat and Lorentzian respectively.

The measurement procedure is simple. First, we find the AC bias such that the cooperativity is at or close to the optimal value determined in previous stages of characterisation. Then, we apply white noise with a waveform generator to the excitation coil and measure the mechanical spectrum.

In this kind of measurement, it is important to be able to convert the injected noise to Johnson noise in the circuit. To this end, we use the circuit model to calculate the full circuit

impedance in parallel with the transducer and the equivalent Johnson noise in the circuit. Similarly, we find the current in the detection coil due to the noise drive and convert this to units of room temperature Johnson noise found in the first step. The results are shown in figures 3.10 and 3.11.

The displacement spectrum grows linearly with increasing Johnson noise temperature and it is a straightforward exercise to find the intrinsic noise of the device. Based on the measurement, we find $T_D = 210 \pm 16$ K. The noise temperature can be further divided into optical and mechanical noises and we find $T_m = 112$ K.

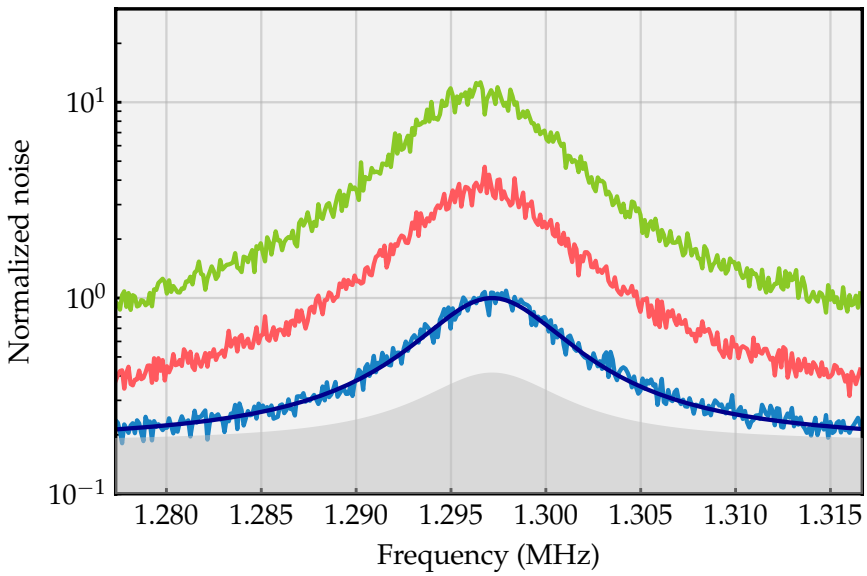

Figure 3.10: The device noise is extrapolated in a Y-factor like measurement. White noise drives the membrane motion. The blue, red and green spectra correspond to different levels of noise drive. The shaded gray area is the extrapolated device noise.

3.5.6 *Device summary*

To summarize, the intrinsic noise temperature of the transducer was found to be approximately 210 K consisting of mechanical noise 120 ± 6 K and optical noise 90 ± 15 K. Based on the measured cooperativity, we would expect mechanical noise temperature of 112 ± 3 K, close to the extrapolated value. In practice, we found the system most convenient to operate with cooperativity $C = 33.0$, determined from the broadened linewidth of $\Gamma_{em} = 8.260 \pm 130$ kHz, away from the optimal cooperativity as is evident from the difference beween optical and mechanical noise.

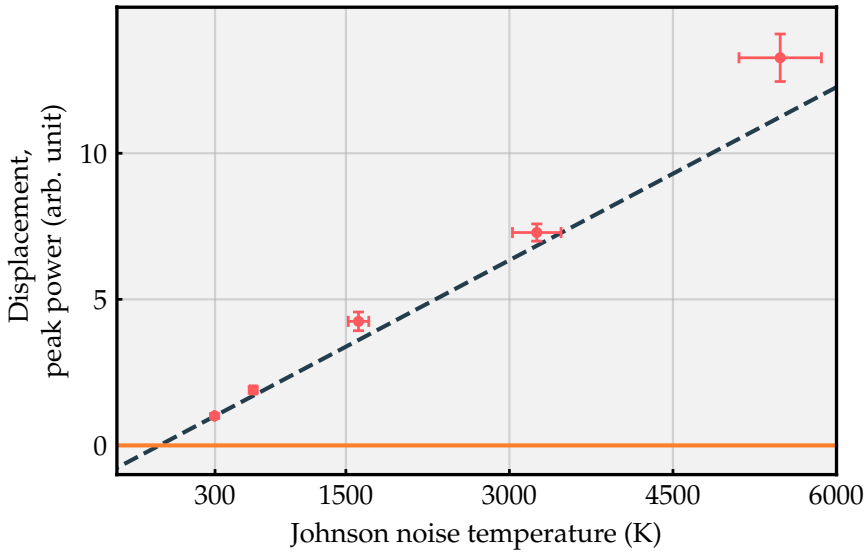

Figure 3.11: The extrapolated noise temperature of the integrated transducer is approximately 210 K. The data points correspond to different levels of injected noise in the Y-factor inspired measurement. The orange line is a guide for the eye to locate the zero level where the intersect with the fitted line determines the noise temperature.

Based on the circuit model, this can be equivalently stated as voltage noise of 99 $\mathrm{pV}/\sqrt{\mathrm{Hz}}$ or magnetic field sensitivity 8 $\mathrm{fT}/\sqrt{\mathrm{Hz}}$. The noise temperature can also be expressed as a noise figure $\mathrm{NF} = 2.33 \pm 14$ dB. The practical signal-to-noise bandwidth is wider than the broadened mechanical response and it is found to be $BW = 12.3 \pm 7$ kHz.

However, the state of the art MRI amplifiers boast noise temperatures of approximately 55K and thus, the first generation device falls short of the current best electrical amplifiers. Nevertheless, the devices compares favourably to other optomechanical transduction schemes in a similar regime. For example, the noise is lower and the bandwidth larger than in [66] or [67]. While a previous experiment in Copenhagen did achieve significantly lower noise it was based on a DC bias and the device and required measurement setup was not very portable [65].

3.6 MAGNETIC RESONANCE IMAGING

As mentioned repeatedly, the ultimate goal of the project is to replace the electrical amplification circuit in a commercial MRI scanner. We had access to a clinical 3T scanner[8] and targeted the $^{13}\mathrm{C}$ resonance at approximately 32 MHz.

8 GE MR750

As a proof of principle, we image an MRI phantom in a clinical setting. Imaging phantoms are a typical calibration technique for various imaging technologies. They should have a good contrast and feature distinct spectral shape. In our case, the phantom is a simple plastic[9] bottle of ehtylene glycole that has an easily recognisable triplet spectrum.

While the device was similar[10], the experimental setup was slightly different. The most significant changes were limited to the LC-circuit.

3.6.1 *Circuit modifications*

The very first tests at the scanner proved disappointing. During the MRI sequence, the devices simply broke. On closer inspection, the membrane collapsed on the capacitor. The cause was ultimately found to be the excitation pulse used to flip the spins. The so called transmit pulse is strong, at the resonance frequency of the LC circuit, and thus causes a large voltage in the circuit and this collapses the membrane.

We take two protective steps in the circuit to prevent the collapse. First, during the excitation pulse, the resonance frequency of the LC circuit is tuned away from the pulse frequency and then switched back once the pulse has passed to pick up the desired NMR signal. It goes without saying, that the shift must be reversed, and the resonance frequency returned to the original value quickly, before the spins have relaxed to their initial state and the NMR signal has passed.

To facilitate the shift, we split the detection coil and added a so-called trap circuit in the coil [72]. When a trigger voltage activates the circuit, the frequency shifts and the circuit is insensitive to the magnetic field at the excitation frequency. The trigger signal is derived from the MRI machine itself and it follows the pulse.

Second, we add cross diodes in the main circuit. The purpose of the diodes is to prevent too large voltage across the membrane capacitor. The modifications are highlighted in figure 3.12 showing a photo of the circuit and the circuit diagram.

9 Due to the strong magnetic fields, all material near the scanner should be nonconductive.

10 The particular transducer chip was different than the one explored in the previous section, but with broadly similar performance.

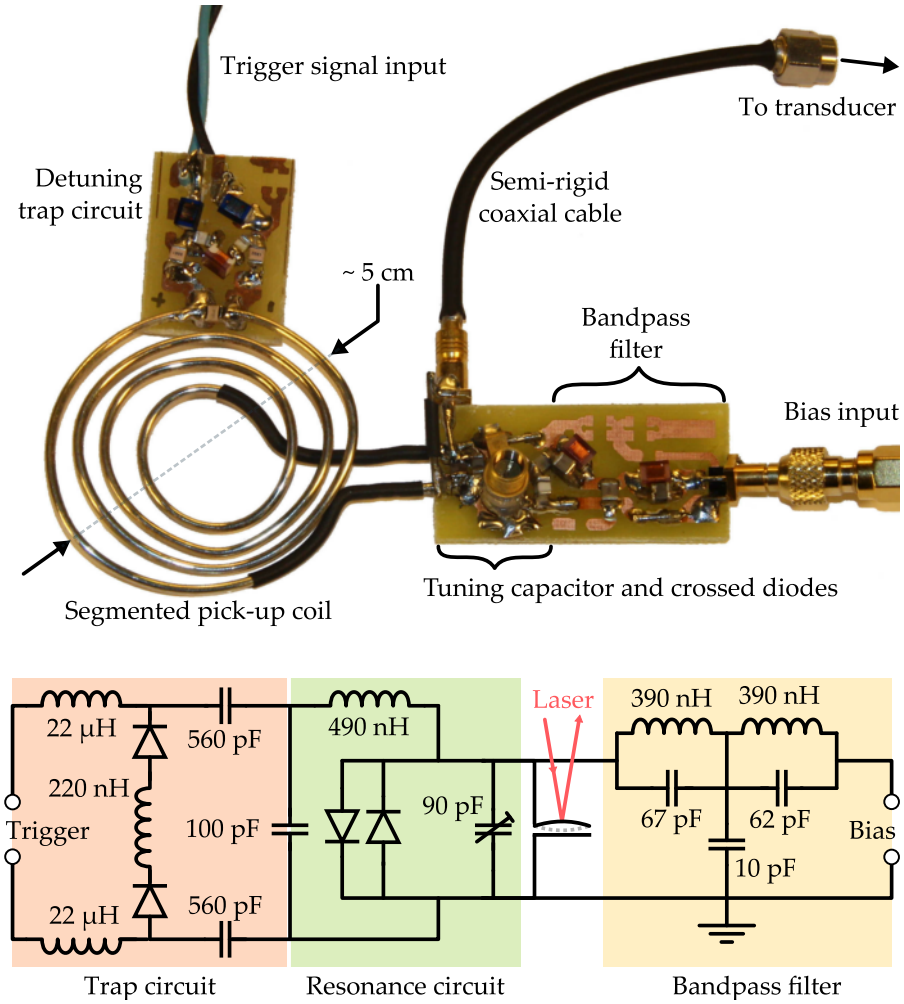

Figure 3.12: The modified detection circuit. Compared to the previous circuit, we have added a detuning circuit and crossed diodes to protect the transducer during the imaging pulse sequence. Adapted from [55]

3.6.2 *Imaging setup*

Operating the transducer in the scanner creates its own set of problems in addition to the membrane collapse. As mentioned, the strong magnetic fields mean, that all components near the scanner have to be immune to them. Most prominently, we replace the metal vacuum chamber with a fiber glass one[11]. The vacuum pump is evacuated with a molecular sieve instead of the usual turbo pump.

Further, the scanner is inside a shielded room and the amount of equipment that can be placed there is very limited. Most of the equipment, such as the laser, detector and bias generator had to be in the adjacent operating room. In principle, long fibers

11 The chamber was provided by our collaborators at DTU Hypermag group.

should prove no trouble and with proper shielding, electrical connections are likewise possible.

However, the circulator is based on a local magnetic field and thus, cannot be placed in the room with the scanner. Furthermore, we found that with the circulator in the adjacent rooms with 10 m fiber between it and the transducer, additional noise appeared in the optical readout. We suspect, that the long fiber allowed interference between the propagating fields and part of the field reflects back to the laser source. The source is a comparatively cheap diode laser without built in protection and it is hence susceptible to the backscattered light causing mode hops in the output.

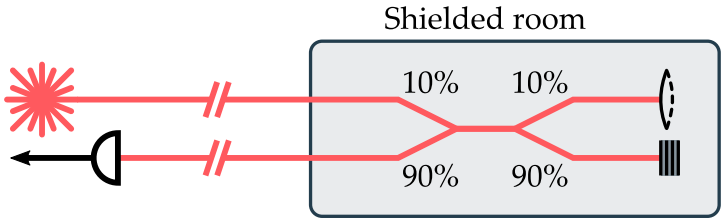

Figure 3.13: The modified optical setup to account for the shield MRI scanner room. The circulator is replaced with 90-10 beamsplitter. The laser is connected to the 10% input. 10% of the output goes to the transducer and 90% is terminated in a beam dump. Then 90% of the reflection is routed to a detector.

We replaced the circulator with a 90-10 fiber coupler. The coupler is a passive component based on two fiber cores in close proximity and thus could be placed next to the scanner. The schematic is shown in figure 3.13. With the splitter, the optical noise disappeared and the performance was similar to characterization setups in our local laboratory.

3.6.3 *Imaging with optical amplification*

Setting up the electrical connections required a few more steps. The connections are shown in detail in figure 3.14 and elaborated in the caption. For now it suffices to say that we chose, for simplicity, to use the analysis and imaging software of the scanner. In practice, this means that the output of the photodetector is at the mechanical frequency but the machinery of the scanner expects an input at the NMR frequency. Thus, the signal needs to be upconverted from ω_m to $\omega_{LC} \approx \omega_{NMR}$. This conversion is most conveniently done by deriving the demodulation signal from the same signal generator that provides the AC-bias.

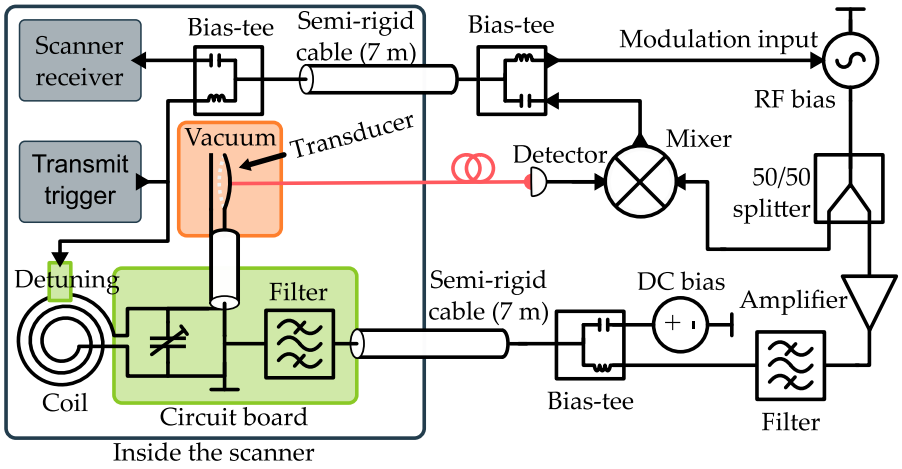

Figure 3.14: The complete connections of the imaging setup. The trigger signal is derived from the scanner itself and the output of the photodetector is upconverted to the NMR frequency and directed to the MRI scanner's receiver. Since the trigger signal and the MRI signal are at very distinct frequencies, we use the same cable to route both signals and a bias-tee to separate them. Adapted from [55]

Phantom spectrum

Instead of reconstructing an image, it is instructive to look at the spectrum of the signal. As hinted before, the chosen phantom, ethylene glycol has a very distinct triplet spectrum. Compared to the conventional detection circuit, the amplifier recovers the the same spectral shape with comparable signal to noise as shown in figure 3.15.

Image reconstruction

While the spectrum is already proof enough that the transducer picks up the correct signal, the most salient feature of the MRI scanner is imaging[12]. To that end, we run the imaging routine and construct the image using the scanner's reconstruction algorithm. The end result is shown in figure 3.16. The transducer can indeed be used in the scanner to record an image verified against the image acquired with the conventional circuit. The images are not directly comparable due to a difference in receiver coils between them.

12 There is a hint in the name of the technology.

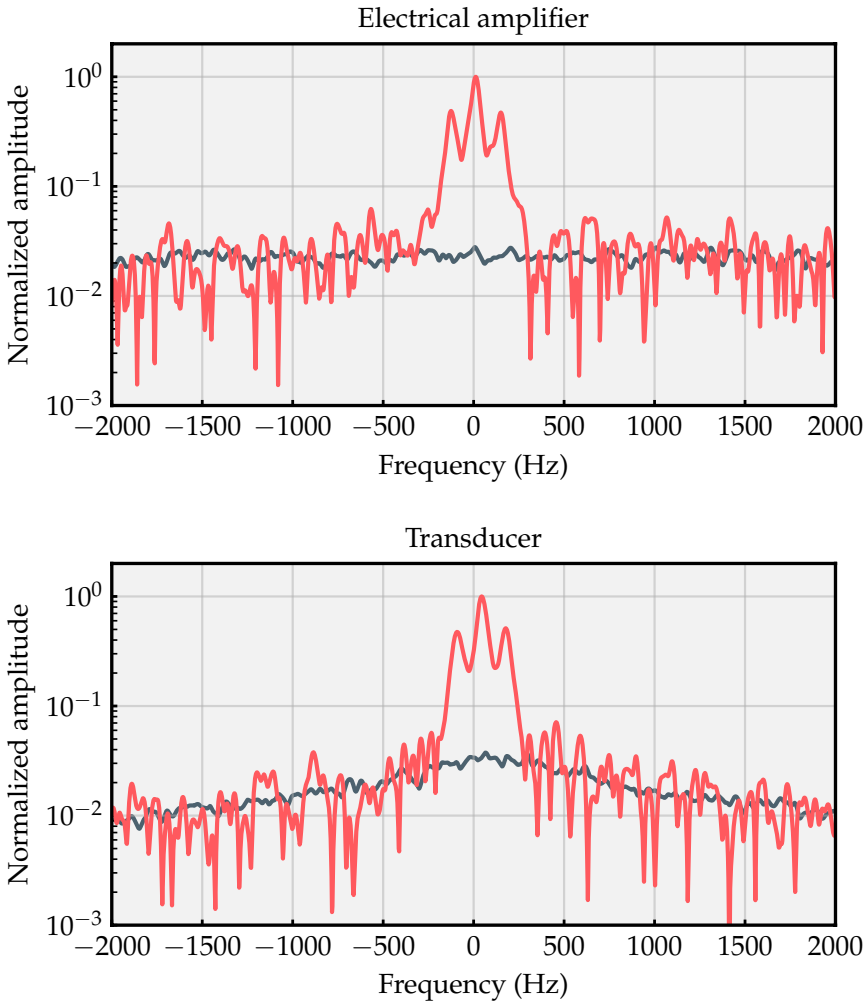

Figure 3.15: The transducer circuit recovers the same spectrum with comparable signal to noise as the standard electrical detection circuit. Adapter from [55].

3.7 FUTURE DEVELOPMENT

As it is, the integrated transducer is a very useful device. While the current noise performance is still worse than state of the art electric amplifiers, straightforward improvements such as increasing the reflectivity of the cavity mirrors could help bridge the gap. On the other hand, the device is compact and lightweight and compatible with commercial MRI scanners. Thus, even with the current performance, it could offer benefit in a strong magnetic field or in a situations where a larger number of coils is required. As an example, we can imagine using the transducer chip in a 96 coil receiver ”helmet” to significantly reduce the weight and size of the array[73].

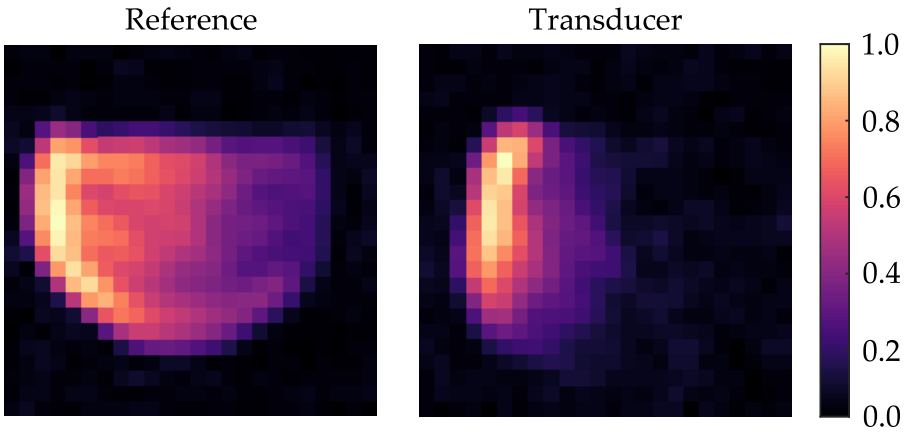

Figure 3.16: The acquired image with commercial electronic amplifier (left) and the transducer (right). The orientation between the measurements is slightly different and the standard detection used a different coil with improved depth penetration. However, the curvature of the bottle is clearly seen.

The most significant drawback of the current device is that it still requires an external vacuum chamber. However, the vacuum requirement is not particularly stringent. The mechanical quality factor is relatively low and hence a relatively low vacuum is not an issue and individual vacuum packaging is possible. Another venue of development would be to remove the need for the AC bias cable. One possibility would be wireless delivery of the bias such that the only physical connection needed would be the optical fiber[74].

4 ROOM TEMPERATURE QUANTUM EXPERIMENTS

Most optomechanical experiments in the quantum regime operate at the very least at moderate cryogenic temperatures from liquid Helium flow cryostats all the way down to millikelvin temperatures routinely enabled by dilution refrigerators. The reason for this becomes very apparent as we take a look at quantum cooperativity. As we may recall from chapter 2, the quantum cooperativity is defined as

$$C_q = \frac{4g^2}{\kappa\Gamma_m\left(n_{th} + \frac{1}{2}\right)}, \tag{4.1}$$

where we have written the mechanical decoherence rate explicitly. Again, as we may recall, to a very good approximation, the thermal occupation of the bath at the mechanical frequency is

$$n_{th} = \frac{k_B T}{\hbar\omega_m}. \tag{4.2}$$

For a megahertz resonator, we would expect more than six million thermal phonons at the room temperature. The consequently larger thermal coherence rate places very stringent requirements on the other parameters g, κ and Γ_m to reach the quantum regime of $C_q > 1$.

A typical demonstration of 'quantum operation' and a starting point for more advanced optomechanical protocols is the preparation of the motional ground state. In a cryogenic environment, such experiment can be described as almost routine and the motional ground state has been prepared in numerous systems [12, 13, 11, 14, 15].

Despite already quite remarkable progress in exploring and developing ever finer optomechanical systems, the goal remains challenging at the room temperature. Only four years ago[1], the best effort was generating quantum correlations in the output field of a room temperature optomechanical system [75]. Even today, to the author's best knowledge, only levitated nanoparticles have been successfully cooled to the ground state from the room temperature[76, 77]. For nanomechanical resonators, the closest approach is 26 phonons for a 950 kHz nanobeam coupled to an optical crystal cavity [78]. More recently, the LIGO collaboration has shown cooling of a 10 kg mirror's center of mass motion down to just above 10 phonons [79].

1 As of 2021

Our approach is based on leveraging the exceptionally low mechanical decay rate of soft-clamped silicon nitride membranes and the local expertise in their fabrication. In a relatively recent experiment, such membrane's mode was feedback cooled down to the ground state [14]. The particular assembly could be operated at $C_q > 100$ at bath temperature of approximately 10K. In our experience, the cryogenic temperature increases the mechanical quality factor by roughly a factor of three. Thus, *without any modifications*, the particular assembly should already enable $C_q > 1$ and thus ground state cooling alread at the room temperature of 300K! But, as the reader perhaps already senses, the situation is more complicated.

4.1 MIRROR NOISE AND MITIGATION

The typical optomecahnical cavity in our laboratory, is couple millimeters long and formed by two cylindrical mirrors, a flat and curved one, both 7.75 mm in diameter and 4 mm long. Like all objects, the mirror substrate supports mechanical mode and this motion causes fluctuations in the cavity length. These cavity length fluctuations translate into phase with exactly the same mechanism as in the canonical optomechanical system. The excess phase noise, most often called *mirror noise* due to its origin, if at too high level, will prevent cooling the mechanical resonator to its quantum ground state. The motion of the mirrors causes incoherent frequency fluctuations that prevent coherent control of the mechanical motion.

The lowest occupation for a given level of phase noise can be calculated as [29]

$$\bar{n}_{min} = \sqrt{\frac{n_{th}\Gamma_m}{g_0^2} S_{\omega\omega}(\omega_m)}, \tag{4.3}$$

where $S_{\omega\omega}(\omega_m)$ is the phase level at the mechanical frequency. Settin $n_{min} < 1$, the expression can be recast as

$$S_{\omega\omega}(\omega_m) < g_0^2 \frac{\hbar Q}{k_B T} = \frac{g_0^2}{n_{th}\Gamma_m} \tag{4.4}$$

With this expression, the 'knobs' that can be turned are clear. Lowering the temperature reduces the number of thermal phonons and at the same time, damps the motion of the cavity end mirrors reducing the amount of mirror noise. However, for obvious reasons, for a room temperature experiment, cooling is not an option.

That leaves three options, increase the coupling, increase the mechanical quality factor or reduce the mirror noise. To some

extend, we employ all three strategies. Let us start with ways to engineer the mirror noise.

4.1.1 *Fiber mirrors*

To the best of our understanding, the mirror noise results from vibrational modes of the substrate itself and as such, frequencies of the modes are dependant on the bulk properties of the mirrors. Furthermore, excess phase noise is only a problem *near the mechanical frequency* and can in principle be just avoided. Unfortunately, our usual cavity mirrors do not have a quiet enough region around feasible membrane frequencies[2].

Instead of membrane frequency, our aim is then to engineer the vibrational spectrum of the mirror modes. To that end, we have chosen to investigate fiber based mirrors[80, 81]. A typical optical fiber has diameter of only 125 µm, a reduction by more than a factor of 60 compared to our typical mirror. The smaller size of the fibers should move the mirror modes to much higher frequencies leaving the region around the membrane mode of interest relatively quiet.

The first use cases for a fiber cavity[3] was to demonstrate strong-coupling cavity QED with Bose-Einstein condensates[82]. For most experiments, the main attractive features of fiber cavities were compactness, direct cavity-fiber coupling and tiny beam waist compared to cavities with macroscopic mirrors.

It should also be noted, that fiber cavities are not without precedent in optomechanics, though typically not for mirror noise reasons. They have been used in a membrane in the middle setup [83], carbon nanotubes [84], single clamped rods [85] even for optomechanics with liquid helium [86].

To fabricate our fibers, we collaborated with professor Eva Weig's group in University of Konstanz[4] with whom we prepared the fibers for the subsequent fabrication steps. The fabrication or 'shooting' - the descriptiveness of the term will be apparent very soon - was done at the Karlsruhe Institute of Technology, where professor David Hunger provided access to a shooting setup and offered fabrication expertise.

2 In principle, there is great freedom to choose where the membrane frequency lies. In practice, values between 1 to 1.5 megahertz have been found to yield highest quality factors. Venturing beyond this regime has proven counterproductive even when taking into account the other benefits of higher frequency.

3 We'll simply write fiber cavity instead of other, more cumbersome terms such as Fiber based Fabry Perot cavity or something equally contrived.

4 At the time of writing, professor Weig has moved to the Technical University München, whereas during the fiber mirror fabrication, her group was still at University of Konstanz.

Fabrication of fiber mirrors is in principle simple, but requires dedicated equipment and special fibers. The steps are shown in figure 4.1. Typical fibers have their glass core surrounded by a thin polymer layer and depending on configuration, there are usually additional protective layers. The bare fiber is very fragile and thus at least the innermost protection is needed. However, the typical polymer used to protect the fiber will not withstand the temperatures the fiber would be exposed to during the deposition of the high quality mirror coating. Instead, we choose to use copper coated fibers[5] that are otherwise identical to usual ones.

The initial step in the fabrication is removing all protective coatings and cleaving the fiber face. Ideally, the fiber face should be perpendicular to the fiber core, such that the cavity axis coincides with it. Any angle between the core and axis would cause additional losses. It is equally important, the cleave is as clean and that there are no imperfections that would scatter light and once again, cause extra losses.

In the fabrication setup, we have access to a conventional microscope view and a white light interferometer (WLI). The WLI in particular is essential in ensuring the quality of the cleave. As one can imagine, the quality of the fiber cleaver is of paramount importance. Good results have been achieved with both automatic and manual cleavers.

The next step in fabrication is the actual shooting. In order to build a stable cavity in practice[6], at least one of the mirrors needs to be curved and for fibers mirros, curved-curved configuration is often most convenient to work with. The curvature is created by shooting the substrate with a strong[7] CO_2 laser pulse. The pulse is short enough, that the fiber does not melt and form a *convex* shape, but rather the pulse evaporates part of the fiber in proportion to the intensity. The pulse shape is Gaussian and the successfully fabricated fiber follows the intensity profile of the pulse. After the shot, the result is again confirmed with the WLI. As a final step, the radius of curvature is fitted with a homebuilt analysis and control program.

As a final step, the fibers are sent to a specialized coating company[8] for the mirror coating. We separated the fibers to two batches such that one batch would be more transmissive at the chosen wavelength. To maximize the detection efficiency, it advantageous to operate a highly one sided cavity such that

5 IVG fiber CU-1300, 125 µm diameter.
6 In theory world, flat-flat cavity is perfectly possible.
7 While it poses no risk for Alderaan, the laser is powerful enough to burn skin and clothing, so very careful operation of the setup is recommended.
8 Laseroptick GmbH

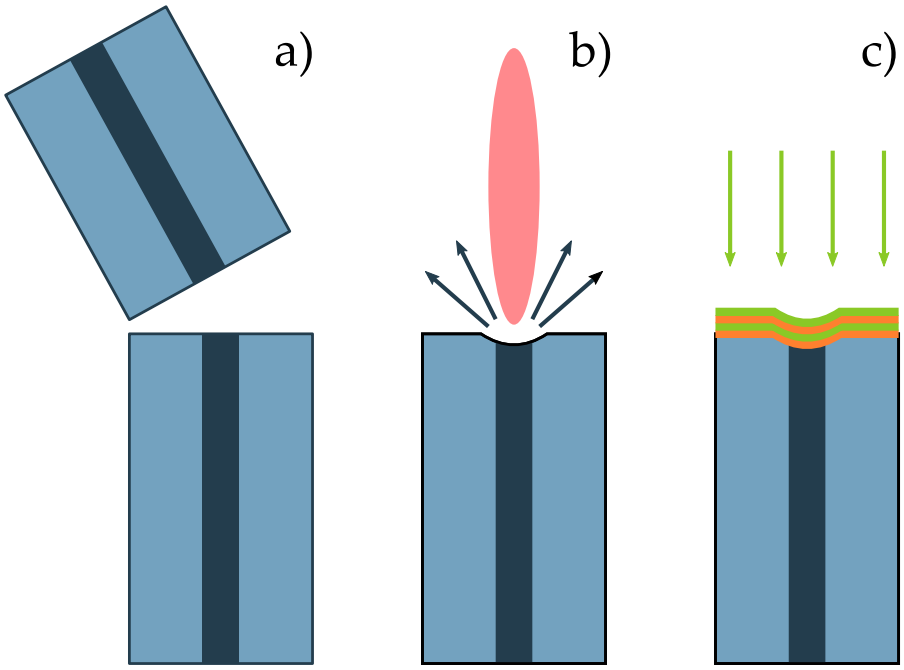

Figure 4.1: The fabrication process of a single fiber mirror. The fiber is first cleaved to create a smooth, perpendicular surface. Then a CO_2 laser pulse is used to evaporate part of the material to create a concave mirror surface. Finally, a high quality mirror coating is deposited on top.

most intracavity light carrying information leaves through one port.

Coupling efficciency and cavity design

Before we glossed over the fact that the cavity mode shape is not necessarily the same as the fiber mode and the coupling between them is not perfect. This is typically modelled as *mode matching* ε that signifies the fraction of light coupling to the desired mode. From the perspective of the detector, the rest of the light is lost as it couples to some other modes. When considering the entire experiment, mode matching is part of the total detection efficiency, $\eta_D \propto \varepsilon$.

Given the radius of curvature, the length of the optical cavity and the parameters of the incoming light field, mode matching can be estimated with a relatively simple formula [80]

$$\varepsilon = 4\left[\left(\frac{w_f}{w_m}+\frac{w_m}{w_f}\right)^2+\left(\frac{\pi n_f w_f w_m}{\lambda R}\right)^2\right]^{-1}, \tag{4.5}$$

where w_f is the fiber mode field radius, w_m the cavity mode radius *at the mirror of interest*, n_f the refractive index of the fiber

and R the radius of curvature of the mirror. From the formulation, we immediately see that much of the mismatch is due to the difference in mode size. w_f is given by the properties of the particular fiber and for the cavity mode radius at the mirror, the mode radius at mirror 1 is found to be

$$w_m^{(1)} = \sqrt{\frac{2L}{k}} \left(\frac{g_2}{g_1(1-g_1g_2)} \right)^{\frac{1}{4}}, \tag{4.6}$$

where λ is the resonant wavelength, L the length of the cavity and where we have introduced notation $g_i = 1 - L/R_i$. In the experiment, we are interested in two special cases. First, the case where both mirror curvatures are the same $R_1 \approx R_2 = R$ where

$$w_m^{(R_1=R_2)} = \sqrt{\frac{2L}{k}} \left(\frac{1}{1-g^2} \right)^{\frac{1}{4}}. \tag{4.7}$$

Second, one of the curved mirrors is replaced with a flat one. In that case, the cavity mode radius is given by

$$w_m^{(R_2=\infty)} = \sqrt{\frac{2L}{k}} \left(\frac{1}{g-g^2} \right)^{\frac{1}{4}}. \tag{4.8}$$

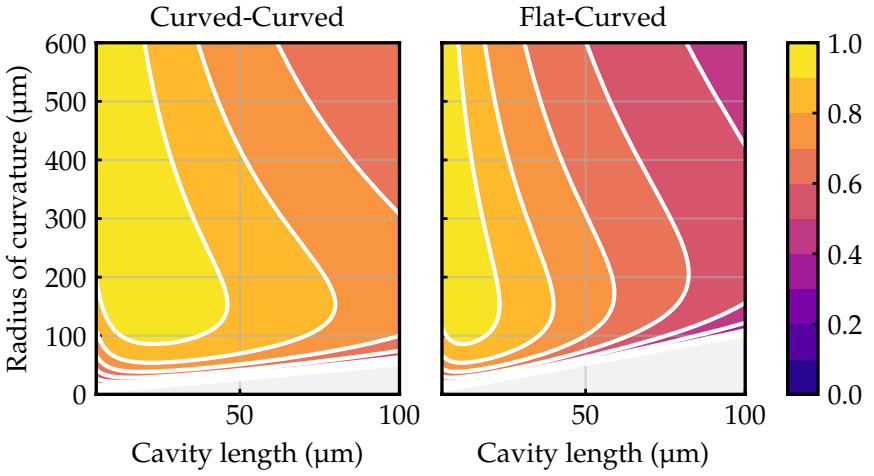

Figure 4.2: Mode matching efficiency shown against mirror curvature and cavity length. On left, we have a cavity consisting of two curved mirrors and on the right, similar graph but for a cavity where one mirror is flat and the in- and outcoupling is via the curved mirror.

Aggregate data about the final fibers is shown in figure 4.3. Some shooting results, good and bad, are shown in figure 4.4.

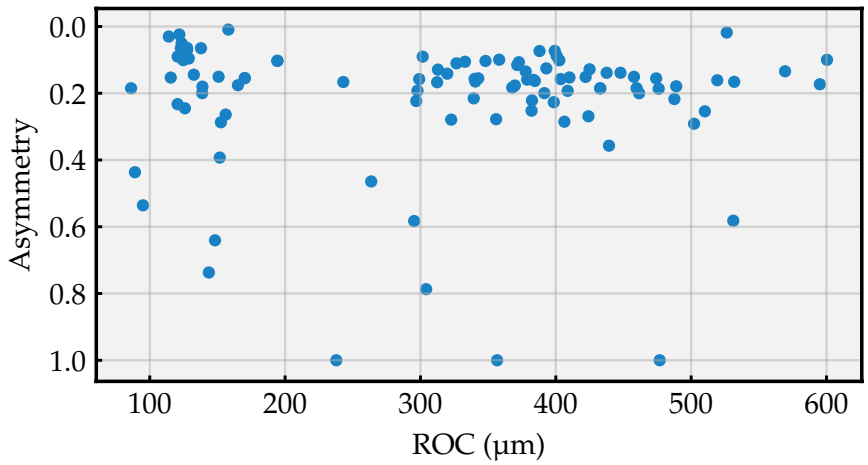

Figure 4.3: The fiber mirror curvature and asymmetry. Most fibers had a decent, less than 0.2 asymmetry calculated from the difference between x- and y-direction curvatures.

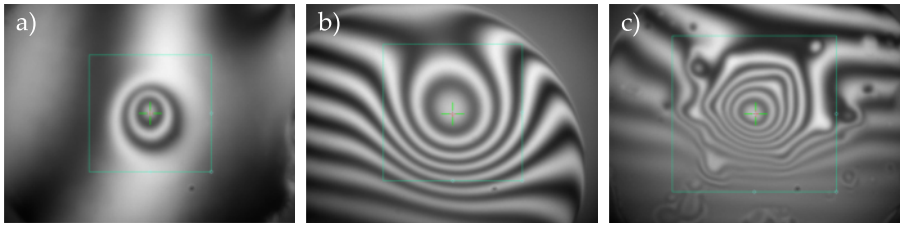

Figure 4.4: Some examples of shot fiber faces taken with a white light interferometer. The green box indicates the fitting area of the characterization algorithm. a) There are only few interference fringes across the face meaning it is perpendicular to the imaging axis. The indentation is also very close to the center of the fiber. b) The fiber face is clearly angled and the indentation is towards the edge. c) This fiber probably had some dust before the shot that caused the 'splattered' look.

1

4.1.2 *Fiber-fiber cavities*

Our initial focus was on building fiber-fiber cavities and measuring their noise performance. The initial 'test bench' was made without any consideration for membrane integration. We pre-aligned two 145 µm bore ceramic ferrules[9] with a spare piece of fiber and glued them in place with either UV curable glue[10] or Stycast 2850FT. The base of the assembly was a simple alu-

9 Off the shelf models from OZ-optics
10 Norland Optical Adhesives 81, custom built UV source

minium piece with milled space for a shear piezo and a 200 µm thick 'bumper' to set the distance between the ferrules. One of the fibers is glued or taped on a shear piezo to tune the cavity length and the other one is fixed on a fiber rotator to find the optimal angle between the fibers. While in principle, the fibers mirrors would be symmetric around their core, there are a number of fabrication imperfections that will break the symmetry such as the indentation being off center of significant asymmetry in the pulse shape. Some examples are shown in figure 4.4. If the chosen fibers were 'good', that is, the indentation was relatively symmetric and placed over the fiber core, finding and optimizing the cavity was typically fast. In practice, we found shorter cavities performing better than longer ones.

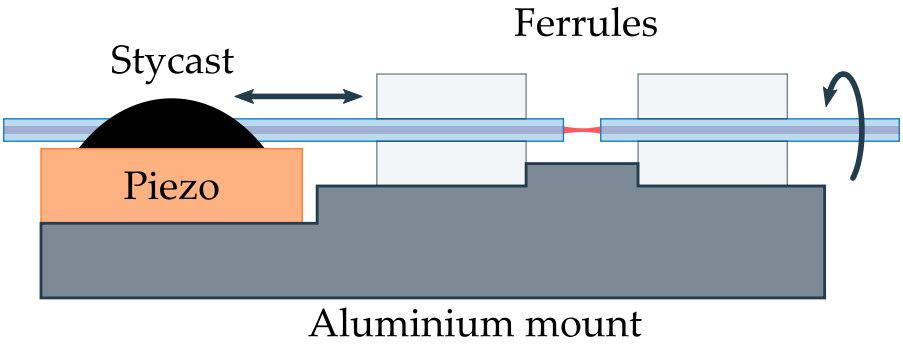

Figure 4.5: A simplified, not to scale, schematic of the first generation fiber cavity. Pre-aligned ferrules set the 'xy-position', where z is chosen to be along the cavity axis. The left fiber was glued on a shear piezo with Stycast to scan the cavity length and lock the cavity. The other fiber was free to move and attached to a fiber rotator. In principle, the fibers should be radially symmetric, but in practice, there are some asymmetric features.

4.1.3 *Exoskeleton mirrors*

While the fiber cavity seemed to function, we had not yet developed a satisfactory way to integrate a membrane in the cavity. As we had seen, both in theory and in practice best performing cavities were very short, much less than 100 micrometers and the test bench was quite stable. Membrane frame however, is 500 µm thick. In order to insert the membrane into the cavity, the the separation between the mirrors would need to be increased by nearly a millimeter and brought back to 100 µm once the membrane Alternatively, the cavity could be assembled and aligned with the membrane already in place. In principle, longer fiber cavities are possible and lengths up to 1.5 mm have been

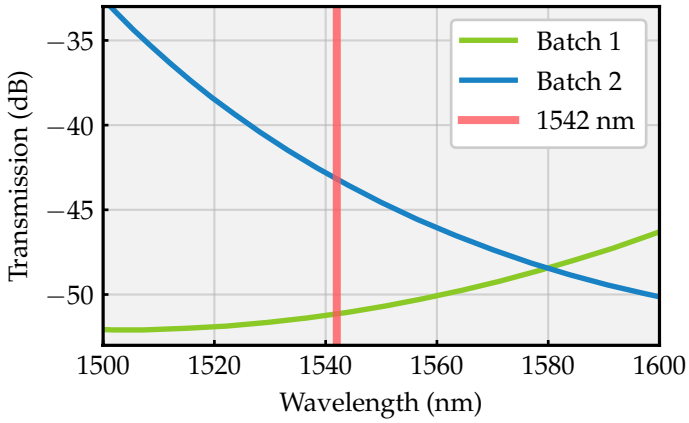

Figure 4.6: The planned transmissivities of the fiber mirrors. The red vertical line indicates the wavelength of the laser. At the target wavelength, the coatings should allow an 8 dB difference between the cavity mirror transmissivities translating into XX % overcoupled cavity.

demonstrated [87]. However, the radii of curvature of our fiber mirrors precludes the possibility in our experiment. Thus ultimately, neither option is very desirable. Pulling back the fibers risk instability and doing so could degrate the cavity alignment. On the other hand building the cavity around the membraned adds complexity to the alignment process and makes sample exchange difficult.

Fortunately, in parallel with the fabrication of the fiber mirrors, Yeghishe Tsaturyan had thought about extending the phononic engineering to mirrors. Before the advent of soft clamping, the silicon nitride membrane was embedded in a phononic crystal shield to reduce radiation losses to the environment. In a similar fashion, the strategy is to bond a thin pyrex glass wafer on a silicon phononic crystal exoskeleton structure [88]. Based on finite element simulations, the combined structure would feature a bandgap and thus reduced motion near the center of the mirror.

The pyrex wafer is however only 100 µm thick and simply handling it is not a trivial task. However, we managed to fabricate six mirrors that were coated with a broadly similar coating as the fibers, but slightly shifted in wavelength. However, on some devices, the bonding was not uniform leaving part of the mirror disconnected from the silicon structure. When using such mirror with the 'bubble' in a particularly unfortunate place, we observed significant noise both in the cavity resonance and in the phase of the output light.

The main advantage of the so called exoskeleton mirrors is that they allow very simple and stable integration of membranes

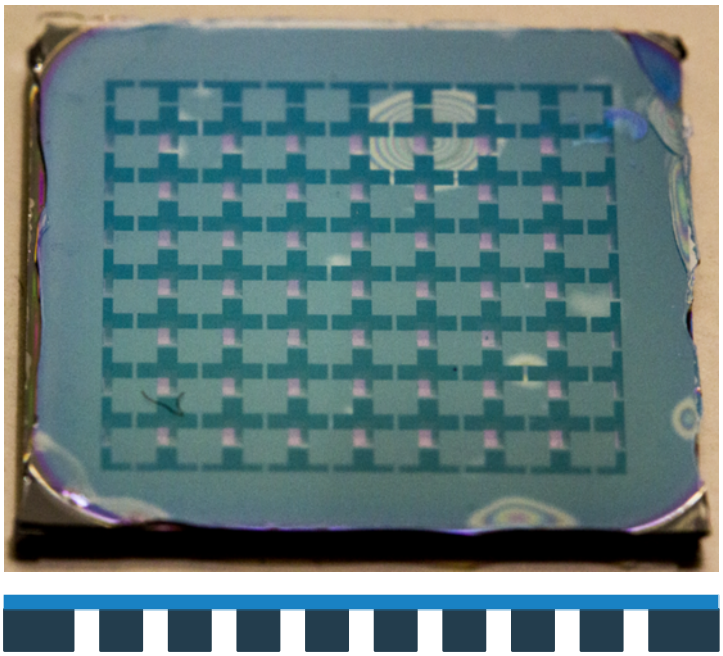

Figure 4.7: A photograph of an exoskeleton mirror. The mirror consists of a silicon exoskeleton structure patterned with a phononic crystal and a thin pyrex glass bonded on it. The combined structure has a bandgap suppressing mirror noise around 1.5 MHz. Interference rings indicate areas where the bonding was not successful. The cross sectional schematic at bottom shows the structure. The silicon is indeed patterned through.

in the optical cavity. Assuming that both the membrane frame and the mirror surface are clean, when the membrane chip is clamped on top of the exoskeleton mirror, they can be taken to be very parallel. Such arrangement ensures that the cavity axis is perpendicular to the membrane surface and thus there are no scattering losses nor is the coupling reduced due to off axis motion.

4.1.4 *Fiber-Exoskeleton Cavity assembly*

As a first try, the exoskeleton mirror was placed on a mirror mount and the fiber was brought close to it on a three axis translation stage. The configuration gave full control of the cavity alignment. The fiber position was monitored with an infrared microscope and, if the fiber mirror was good, a cavity was typically found almost instantaneously. However, during the initial setups, achieving a stable lock proved challenging. Ultimately, we moved to a monolithic cavity design with no degrees of free-

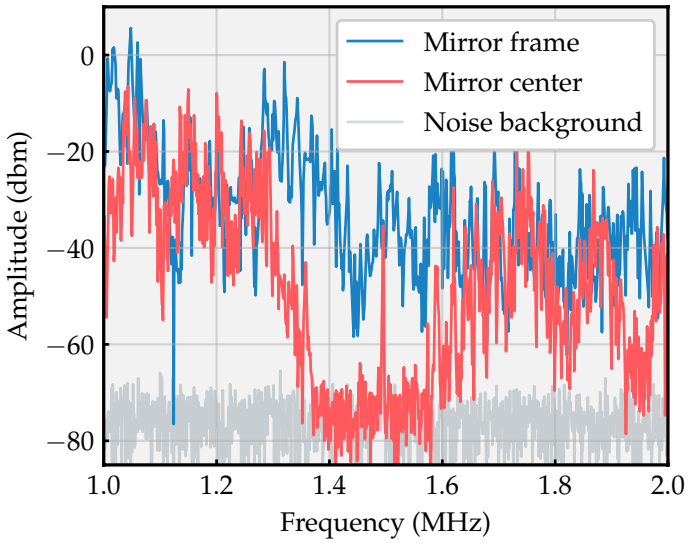

Figure 4.8: The driven response of the exoskeleton mirror measured near the edge, where the phononic crystal has no effect and at the center where noise is suppressed. We see that the bandgap opens as predicted between 1.4 and 1.6 MHz. The sharp peak at 1.5 MHz is a calibration tone.

dom except for a single shear piezo to tune and lock the cavity length.

The cavity assembly consists of an aluminium base that had a threaded through hole for lens to focus transmission and vented screwholes to clamp the mirror on the base. The second half held the fiber mirror that was glued on the piezo with UV curable glue and it was clamped on the exoskeleton side with four M4 screws. To form the cavity, the exoskeleton mirror was clamped on one half and the mount was assembled without the fiber but with the piezo already in place. The fiber was then brought in on a separate 5-axis stage and once good cavity was found, the fiber was glued on the piezo with a UV curing glue and the 5-axis stage was removed. Once in place, the cavity alignment proved robust to gentle shaking and tapping with various light tools. Happily enough, the halves could be taken apart and brought back together without degradation of the cavity alignment. This, and the fact that the 'in plane' fiber position could be adjusted by approximately ± 100 µm, proved invaluable features when we started assembling optomechanical cavities with membranes. The cavity could then be take apart, the membrane exchanged and the fiber position optimised in rapid succession. A cross sectional sketch of the mount, already with a membrane, and a photograph of a finished assembly are shown in figure 4.9.

Based on the planned coating curves, we expected to realize

cavities with finesse up to 40000. However, most of the cavities we built featured finesses between 4000 to 20000. The reduction could in part be explained by misalignment, but a direct measurement of the transmitted power placed an upper bound on the reflectivity at a much lower value than expected. To establish a crude upper bound on the reflectivity, we simply measured the transmitted light through the mirrors. Based on the measurement, the following transmissivities were established $T_{exo} \geqslant 250$ ppm and $T_f \geqslant 2140$ ppm, considerably higher than the expected values. The measured transmissivities would also indicate, that the fiber is more transmissive by about a factor of four. In the end, the fiber mirror being more transmissive proved advantageous. Collimating and collecting the transmitted, now free space, beam would have considerable increased the experimental complexity and fragility compared to the already integrated fiber mirror.

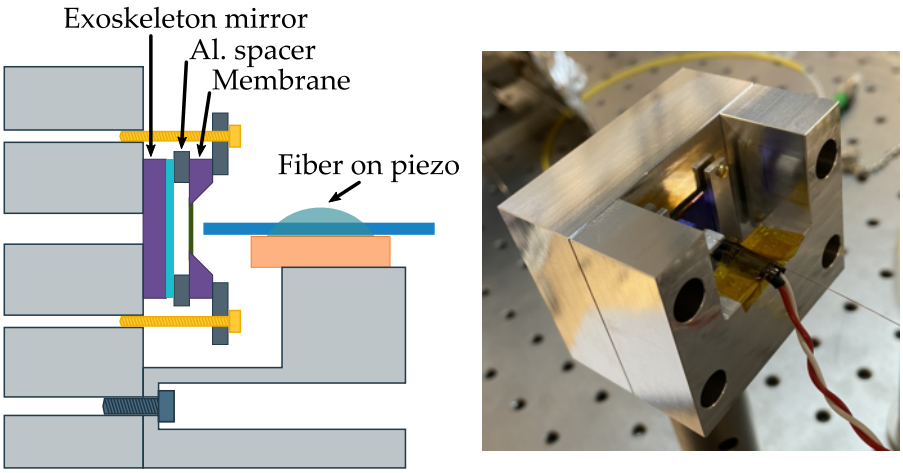

Figure 4.9: On the left, a cross sectional, not to scale, schematic of the monolithic fiber-exoskeleton cavity mount with a membrane. We have omitted to show the top screw for clarity. All screw holes are vented to avoid pockets of air for the eventual use in ultra high vacuum of less than 10^{-7} mbar. We have also included a through-hole for transmitted light from the cavity, but ultimately, given that the cavity is very overcoupled in reflection, decided against using it, that is the transmitted light is allowed to disperse. On the right, a photograph of a complete assembly.

4.1.5 *Cavity performance*

Keeping in mind the criteria presented in earlier section, the critical question regarding the cavity is of course the spectral shape and the level of the mirror noise. Measuring the amount

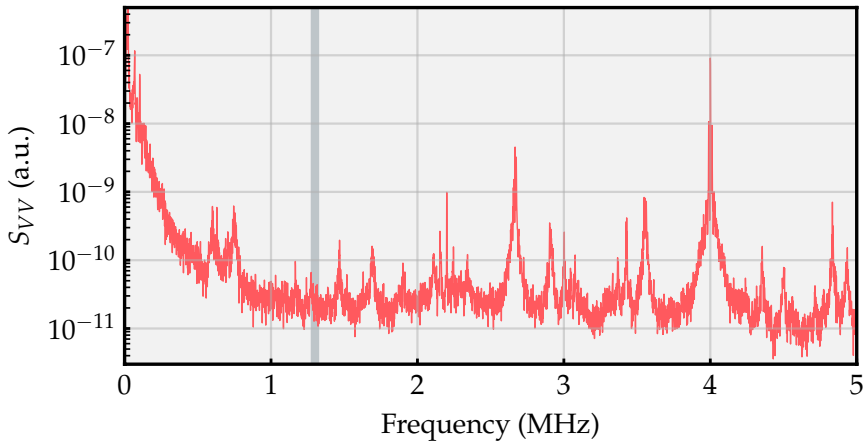

Figure 4.10: The mirror noise spectrum in arbitrary units. The region between 1 and 2 MHz is reasonably clean without large peaks. The gray line indicates the frequency of the membrane mode of interest.

of mirror noise in the cavity is in principle a straightforward task and already an example of an optomechanical position measurement. We place a laser probe on resonance with the cavity and measure phase, on which the mirror motion is imprinted with a balanced homodyme interferometer in Mach-Zehnder configuration. Such spectrum is shown in figure 4.10.

However, we were unable to use the phase modulation calibration tone common in optomechanics [89] due to residual amplitude modulation (AM) in the phase modulator. Alternative calibration methods require very precise knowledge of all system parameters beyond the level we were able to estimate.

4.2 THEORY OF FEEDBACK COOLING

Now that it indeed looks like the cavity performs is at a sufficient level, we can start looking how to prepare the mechanical resonator at the ground state, or look into strategies for quantum control. A very simple way to reduce the thermal occupation is to just cool the environment to a low temperature. For gigahertz resonators, such as many optomechanical crystal devices, this is a straightforward way to obtain the ground state 'for free'. The device is cooled to 10 millikelvin where the thermal occupation is only 0.2 phonons for 1 gigahertz resonator. This is incidentally a way to initialize superconducting qubits in the ground state. With a megahertz resonator at the room temperature however, another technique is needed.

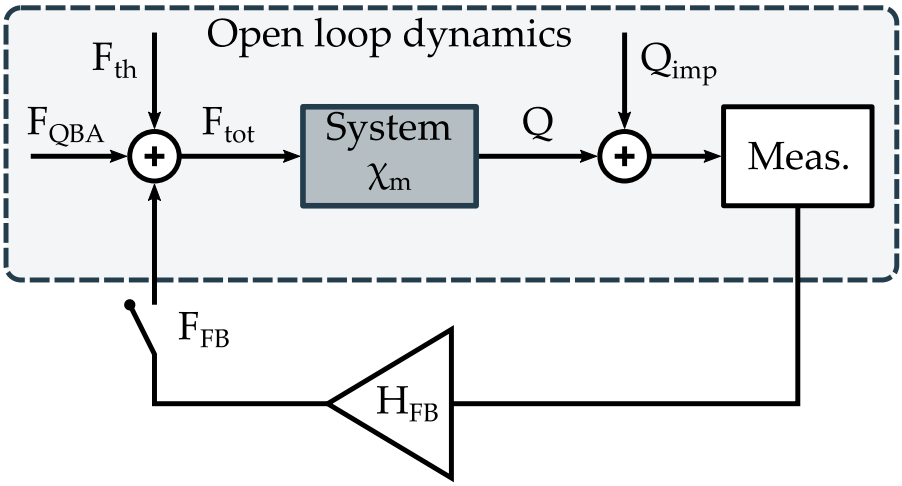

Figure 4.11: A block schematic of feedback in an optomechanical system. The open loop dynamics are determined by the total input force consisting of thermal force and quantum backaction and the mechanical response χ_m. When the loop is closed, feedback adds another force F_{FB} and the system evolves to a different equilibrium determined by the *closed loop* dynamics.

Alternative to passive cooling is the so called coherent quantum control. To step back for a moment, any measurement must inevitably perturb the system. Incidentally, this kind of measurement perturbation was analyzed already in the very early days of quantum mechanics by Heisenberg in a thought experiment that came to be known as the Heisenberg's microscope[90]. In coherent control, there is no measurement and hence no perturbation but rather the coupling between the system and the controller is engineered such that the system evolves to the desired quantum state at the expense of the controller system.

In chapter 2, we looked into sideband cooling that is example of such coherent control scheme[11]. The system of interest, in this case, the mechanical resonator, is contact with a zero temperature optical bath. Under suitable conditions, that is with $C_q > 1$ and when the cavity resolves the mechanical sideband, the mechanical resonator is prepared in the ground state. However, the linewidth of the fiber cavity is typically between 250 and 500 MHz and thus the cavity is very unresolved and sideband cooling will not be sufficient.

Alternative paradigm to coherent control is the *measurement* based quantum control, sometimes, especially in the context of mechanical motion, also known as feedback cooling. The core

11 Alternative way to think about sideband cooling is to consider it as *open loop* control where the measured output is determined by the input, in this case a red detuned drive.

idea is very simple and largely analogous to the principle of noise cancelling headphones. We make a careful measurement of the mechanical resonators position. Then, the measurement record is used to apply a damping force via amplitude modulated light. The motion of the resonator then changes and this change again changes the damping force and the loop continues until an equilibrium position is reached. Most remarkably, a well chosen feedback force counters the effect of quantum backaction!

The name of the technique already gives a good hint at what to look for as figures of merit. In order to apply feedback, the current state of the resonator needs to be known. This necessitates a measurement, and as we already mentioned, the measurement disturbs the system. Then, measurement should extract as much information as possible and disturb the system as little as possible. The ratio between information and decoherence is quantified by the total measurement efficiency η and the total measurement efficiency determines how low occupation the feedback control can reach.

4.2.1 *Feedback control of a mechanical resonator*

While dynamical backation is an immediate consequence of the optomechanical interaction, feedback control is less obvious. Nevertheless, First proposals and experiments are already well over two decades old [91, 92]. Since then, feedback control has been successfully applied in cooling multiple systems ranging from atoms, ions, nanoparticles and nanomechanical resonators all the way to multi kilogram scale gravitational wave detector test masses [93, 94, 95, 96, 97, 98].

In an optomechanical system, the feedback is most conveniently introduced by adding another force term in the mechanical equation of motion

$$\ddot{Q} = -\omega_m^2 Q - \Gamma_m \dot{Q} + (F_{th} + F_{rad} + F_{FB}), \tag{4.9}$$

where we have the usual equation of motion for a weakly damped harmonic oscillator with the motion driven by the radiation pressure force F_{rad} and the thermal force F_{th}. Additionally, there is a new feedback force term F_{FB}.

Without the feedback force, the actual position Q is found to be

$$Q(\Omega) = \chi_m(\Omega) F_{tot}, \tag{4.10}$$

and the *measured* or inferred position $y(\Omega)$ is

$$y(\Omega) = Q(\Omega) + Q_{imp}, \tag{4.11}$$

where $\chi_m(\Omega)$ is the familiar mechanical susceptibility[12] and we have combined the quantum backaction force and the thermal force in a single term F_{tot}. The important feature to note, as we already saw in the treatment of quantum backaction and the standard quantum limit, is that we have no access to the actual position but are limited to finding the measured position $y(\Omega)$ that also a has a contribution from the measurement imprecision.

Feedback force is base on the measured position y such that the feedback force is simply the position multiplied bye a filter function h_{FB}. The equation of motion becomes

$$Q(\Omega) = \chi_m(\Omega)\left(F_{tot} + h_{FB}\, y(\Omega)\right). \tag{4.12}$$

The position Q is solved easily and we can write both it and the measured position when the feedback loop is closed

$$Q(\Omega) = \frac{\chi_m(\Omega)}{1 - h_{FB}(\Omega)\chi_m(\Omega)}\left(F_{tot} + h_{FB}(\Omega)Q_{imp}\right), \tag{4.13}$$

$$y(\Omega) = \frac{\chi_m(\Omega)F_{tot} + Q_{imp}}{1 - h_{FB}(\Omega)\chi_m(\Omega)}. \tag{4.14}$$

There are a couple of features to note. First, solution looks very similar to the one found previously without the feedback. The position is simply force multiplied by a susceptibility, but the susceptibility is modified by the chosen filter and if the filter is chosen carefully, the feedback will lead to similar cooling as we found in the case of sideband cooling.

Second, the driving force has a peculiar form, $F_{tot} + h_{FB}(\Omega)Q_{imp}$ i.e. the resonator is driven by the bath but also by the measurement imprecision. In order to cool the resonator, the filter setting must be such that the filtered imprecision noise is insignificant compared to the total force noise, that is $F_{tot} \gg h_{FB}(\Omega)Q_{imp}$. If this is not the case, the noise heats the mechanical mode.

The symmetrized spectra are then found to be

$$\bar{S}_{QQ}(\Omega) = |\chi_{eff}^{FB}(\Omega)|^2\left(S_{FF}^{tot} + |h_{FB}|^2\bar{S}_{imp}(\Omega)\right), \tag{4.15}$$

$$\bar{S}_{yy}(\Omega) = |\chi_{eff}^{FB}(\Omega)|^2\left(S_{FF}^{tot} + |\chi_m(\Omega)|^{-2}\bar{S}_{imp}(\Omega)\right), \tag{4.16}$$

where we have introduced the feedback-effective susceptibility[13]

$$\chi_{eff}^{FB}(\Omega) = \frac{\chi_m(\Omega)}{1 - h_{FB}(\Omega)\chi_m(\Omega)}. \tag{4.17}$$

12 For simplicity, we have chosen to write χ_m but the treatment is no different if we consider the effective susceptibility containing dynamical backaction terms.

13 Different from the effective susceptibility modified by the dynamical backaction.

In the experiment, we only have access to $\bar{S}_{yy}(\Omega)$. We must then fit equation 4.16 against the measured spectrum, and calculate the actual motional spectrum $\bar{S}_{QQ}(\Omega)$ and the resonator occupation based on the fitted parameters.

An illustrative example of the feedback control is the so called *cold damping* where the filter is $h_{FB}(\Omega) = i\Gamma_m g_{FB}\Omega/\omega_m$ where g_{FB} is the feedback gain proportional to the amount of electrical amplification on the measured photocurrent. With the filter choise, the effective susceptibility becomes

$$\chi_{FB}(\Omega) = \frac{\omega_m}{\omega_m^2 - \Omega^2 - i\Gamma_m(1+g_{FB})\Omega}, \tag{4.18}$$

that is, the mechanical linewidth is broadened and the occupation reduced. An important feature to note, is that the feedback force is chosen to be purely imaginary and thus, the only effect is that it broadens the mechanical linewidth. Any real part of the force, for example due to unideal phase, translates into a frequency shift of the mechanical resonator.

With the cold damping filter, the minimum occupation as a function of the bath and imprecision can be written as

$$n_{min}^{cold} = \frac{n_{bath} + g_{FB}^2 n_{imp}}{1 + g_{FB}}, \tag{4.19}$$

where n_{imp} is the measurement imprecision level represented as an equivalent phonon occupation. The most interesting feature of the minimum occupation is, that it has a minimum achieved at optical gain. Thus, in order to reach $n_{min}^{cold} < 1$, the measurement efficiency must be sufficiently high.

4.2.2 *Practical feedback loop*

Instead of cold damping, we choose to employ a filter based on multiple Lorentzian bandpass filters. In principle, in the presence of only single mechanical mode, one such filter would be sufficient. The mechanical devices however feature multiple out of bandgap modes and the filter can excite some of them at high gain. The strategy in experiment is to start with the single filter and add additional, auxiliary filters to stabilize the troublesome modes as they are identified. Each filter follows approximately the form

$$h(\Omega) = g_{FB}\exp\left(i\Omega\tau - i\phi\right)\left(\frac{\Gamma_{FB}}{\omega_{FB}^2 - \omega^2 - i\Gamma_{FB}\Omega}\right), \tag{4.20}$$

where we have introduced the filter phase ϕ and the delay τ. The filter is centred at frequency ω_{FB} and has bandwidth Γ_{FB}.

The delay is determined by the time it takes to process the signal in FPGA based controller and the total length of the cables. The phase is then tuned such that the total phase of the filter is $\pi/2$. The dominant delay in the feedback chain is the controller that causes approximately 320 nanosecond delay. Based on this number, we calculate the approximate phase and fine tune it until increasing the feedback gain no longer causes significant frequency shift.

4.2.3 *Minimum occupation*

As we have already hinted, under suitable experimental conditions, measurement based control can prepare the mechanical resonator in the quantum ground state. In sideband cooling, we care little about the measurement chain. It only matters that the measurement is able to resolve the zero point fluctuation such that the state of the resonator can be verified. If the system parameters are suitable, the resonator evolves to the ground state without intervention.

In contrast, as we have already stated[14] , feedback cooling requires active measurement of the resonator's state and we only have access to the *inferred* position that contains the measurement imprecision Q_{imp}. Thus it is imperative to minimize the imprecision requiring both strong measurement and a good detection efficiency. It is perhaps most instructive to cast the imprecision as an equivalent phonon occupation. To that end, let us introduce the spectrum of a single phonon excitation at the mechanical frequency

$$\bar{S}_{ZP}(\Omega_m) = \frac{2}{\Gamma_m}. \tag{4.21}$$

The equivalent imprecision phonon number is then found as

$$n_{imp} = \frac{\bar{S}_{imp}}{\bar{S}_{ZP}} = \frac{\Gamma_m}{16\Gamma_{meas}} = \frac{1}{16\eta_D C}, \tag{4.22}$$

where we should remind ourselves of the classical cooperativity $C = 4g^2/\kappa\Gamma_m$. The total *measurement*[15] efficiency η_m can then be cast as

$$\eta_m = \left(16 n_{imp} n_{tot}\right)^{-1}, \tag{4.23}$$

where n_{tot} is the total bath phonon occupation consisting of thermal phonons and both probe and cooling beam quantum

14 Repetita iuvant, also for Latin phrases!

15 Here we stress, that the measurement efficiency is distinct from detection efficiency although the former is in part determined by the latter.

backation. To get a better handle on the parameters that should be optimized, let us write the total phonon number explicitly $n_{tot} = n_{th}\left(1 + C_q^p + C_q^a\right)$ to get

$$\eta_m = \left(\frac{n_{th}(1 + C_q^p + C_q^a)}{\eta_D C}\right)^{-1}, \tag{4.24}$$

$$= \left(\frac{1}{\eta_D C_q} + \frac{1}{\eta_D} + \frac{C_q^a}{\eta_D C_q^p}\right)^{-1}, \tag{4.25}$$

where C_q^a is the quantum cooperativity of the auxiliary beam providing the feedback force. For the moment, let us assume it is weak, that is $C_q^a \approx 0$. In that case, the measurement efficiency becomes

$$\eta_m = \frac{\eta_D}{1 + C_q^{-1}}. \tag{4.26}$$

For optimal control of a single mechanical mode, the minimum occupation is related to the measurement efficiency as

$$n_{min}^{opt} = \frac{1}{2}\left(\sqrt{\frac{1}{\eta_m}} - 1\right). \tag{4.27}$$

Thus, our intuition at the beginning of this chapter has proven correct. Both high detection efficiency determined by cavity outcoupling and losses in the detection chain and high quantum cooperativity are necessary to prepare the mechanical resonator in the ground state.

4.3 THE FEEDBACK EXPERIMENT

Before exploring the feedback cooling results, we will cover both the experimental setup and most important techniques.

For the most part, the optical setup is relatively conventional. We use a single laser source[16] at 1542 nm. The source is protected with an isolator and routed trough a fiber polarization controller (FPC). The beam is first split into the feedback arm and the homodyne detection scheme with a 70-30 splitter. The interferometer is further split into the probe arm and the local oscillator (LO). The LO arm has a variable optical attenuator (VOA) to control the LO power, a fiber stretcher to control the relative phase ϕ between LO and the probe and thus lock the homodyne, and finally, another FPC to optimize the polarization overlap between the probe and the LO. The probe arm has a phase modulator to generate the Pound-Drever-Hall-error signal

16 NKT Koheras Basik E15

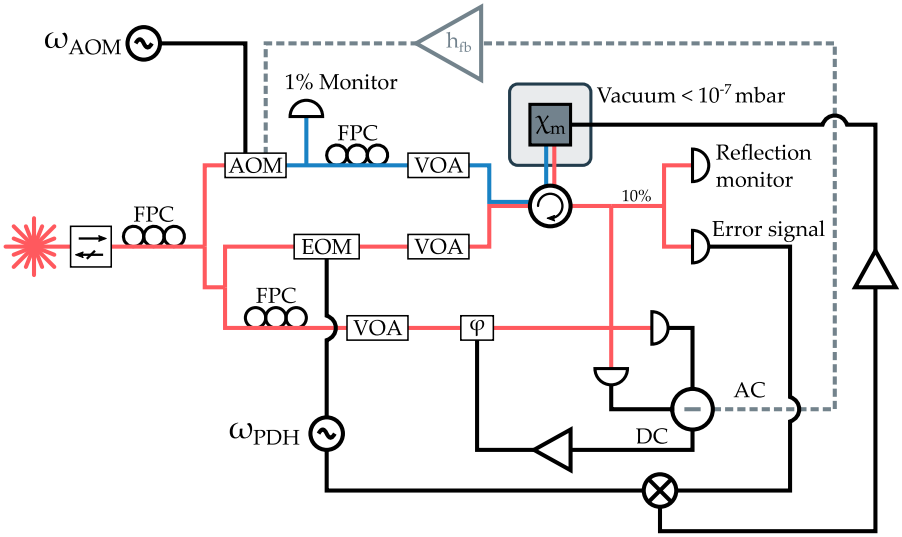

Figure 4.12: The full optical setup consists of a balanced homodyne measurement scheme and and auxiliary feedback beam derived from a single laser source at 1542 nm. The feedback beam is detuned -80 MHz from the probe and LO. Refer to the main text for the detailed description.

for cavity lock and a VOA to control the probe strength. The probe is then combined with the feedback beam.

The feedback arm is routed through a fiber acousto-optic modulator (AOM) that shifts the beam frequency down by $\omega_{AOM} = 80$ MHz. The feedback control is applied via amplitude modulation at the mechanical frequency. The purpose of the shift is then to separate the feedback spectrally from the probe and also provide moderate sideband cooling to stabilize the system. We see approximately 40 dB attenuation of amplitude modulation when the feedback is shifted. After the AOM, there is a VOA after which 1% of the light is diverted to a power meter to monitor the amount of power in the feedback beam. The polarization is again controlled with a FPC to minimize the polarization overlap between the probe and the feedback beam in order to further avoid the contamination of the measurement by the feedback signal.

The feedback beam is combined with the probe beam and routed to the cavity with a circulator that also diverts the reflected beam to detection. 10% of the reflected beam is used to both monitor to reflection and to generate the error signal. The rest is combined with the LO in a variable fiber coupler and measured in a balanced homodyne measurement.

The measurement record is filtered with a Red Pitaya using the IQ module of an an open source software package[99]. The filtered record is used to amplitude modulate the feedback beam

with the AOM to provide the actual feedback force.

4.3.1 *Optomechanical assembly in a fiber cavity*

Integrating a membrane in the cavity is in principle straightforward. However, the cavity length is only approximately 50 µm based on a microscope image and using the known fiber diameter as reference. We wanted to have some distance between the membrane and the flat mirror and thus aimed for separation between 10 and 20 µm. The spacer material thus needed to be thin, UHV compatible and stable. Our initial idea was to use a thin Mylar sheet, but we the assembly proved unstable in vacuum. For unknown reason, when pressure dropped below 10^{-3} mbar, the cavity alignment changed irreversibly such that restoring alignment required venting the chamber and reassembling the cavity. In principle, Mylar should be vacuum compatible, but it might be pliable enough that a pressure gradient would for example shift the membrane tilt.

We found that regular kitchen-grade aluminium foil measured at approximately 15.5 µm thick, was thin enough. Properly cleaned, it was also compatible with the UHV system. With aluminium instead of Mylar, we managed to make assemblies lasting many weeks under vacuum.

As vacuum chamber, we used a repurposed UHV cryostat[17] that could reach vacuum of 10^{-10} mbar. The good vacuum however meant, that the turbo pump was mounted directly to the chamber and the operation of the turbo pump vibrates the cavity such that operating the experiment becomes very challenging. In other experiments, the turbo pump is usually away from the chamber and the connecting vacuum hose is led through a concrete block[18] to isolate the vibrations. This typically completely removes the pump noise from the system. As a consequence, the vacuum quality is somewhat compromised, but for cryogenic experiments, cryo-pumping improves the vacuum significantly.

Our first attempt to mitigate the pump noise was to mount the cavity on a heavy copper base suspended with four springs. The swing did reduce the noise, but at same time, meant that the fiber would have to hang freely for a relatively long distance. In our experience, this translated into amplitude fluctuations in the reflected light.

Instead, we chose to mount the cavity directly on the the cold finger[19] and we added an ion pump to the chamber. The

17 Cryovac Konti

18 Humorously referred to as an impedance mismatcher.

19 The cold finger was the most convenient mounting location. However, despite the name, there is no cooling and the entire system is operated at room

ion pump has no mechanical parts and creates no vibrations but it can only be operated in a good vacuum. Thus, we added a valve between the turbo pump and the chamber such that the chamber is evacuated to approximately 10^{-7} mbar with the usual roughing pump - turbo pump combination. Then the ion pump is turned on and the valve can be closed and the turbo pump turned off. With a Teflon fiber feedthrough [70] and electrical coaxial feedthroughs, pumping only with the ion pump, we reach pressure of approximately $4 \cdot 10^{-8}$ mbar, more then sufficient to reduce the gas damping such that the mechanical Q is no longer limited by it.

Low Mass design

While the fiber cavity investigation was prompted by mirror noise considerations, we soon realized that their small mode waist would allow further engineering of the soft clamped membranes. We covered the optomechanical coupling and the membrane in the middle geometry already in the theory chapter.

The cavity resonance is modulated when the membrane moves in the standing wave. Yet, the membrane does not move as a rigid sheet but rather it has a distinct modeshape. The coupling must then be scaled by the overlap between such mode and the mode function of the optical mode. Additionally, the membrane should be significantly larger to avoid losses and reduced coupling due to clipping. Ideally, we would want to probe the membrane with a point like beam at the point of largest displacement.

The mode waist in the fiber cavity is only a few micrometers. This allows us to reduce the size of the defect. This reduces the effective mass of the resonator increasing coupling by increasing the zero point fluctuation as $g_0 = Gx_{zpf} \propto \sqrt{1/m_{eff}}$ and boosting force sensitivity.

A design dubbed 'Dandelion' with a defect size of only few tens of micrometers, typically 30 µm in the fiber cavity experiment, was developed in our laboratory [100] . The design reduces the effective mass of the membrane compared to the first generation soft clamped design by approximately a factor of ten.

Cavity piezo

While the first generation monolithic cavity proved stable and allowed for feedback cooling runs, in situ tuning of the membrane position in the cavity was not possible. In principle, a widely tunable laser could achieve similar effect, but given the equipment available, this was not an option.

temperature.

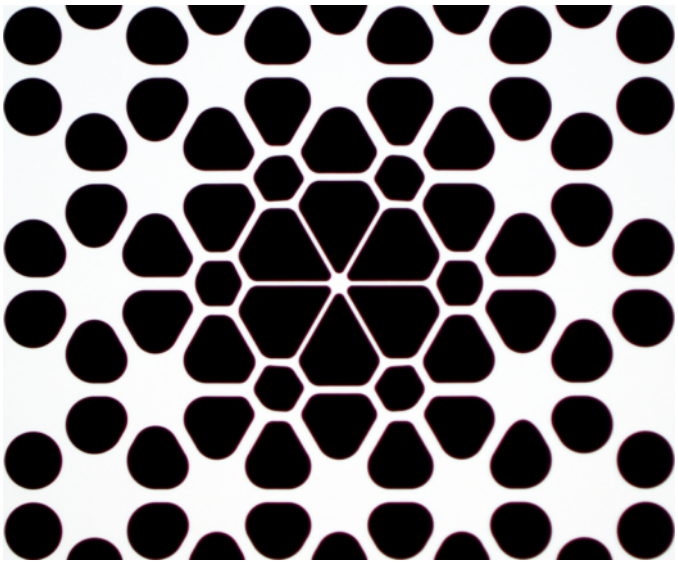

Figure 4.13: An example of a low mass defect membrane. The defect size in the center is only 30 µm in diameter compared to 300 to 500 µm of the first generation soft clamped membrane. The mass of the membrane is reduced boosting force sensitivity and coupling. Adapted from [100]

Instead, we have integrated a ring piezo in the cavity, in a somewhat similar fashion as [44]. The purpose of the piezo is to move the membrane in the standing wave either via bending the membrane frame or via squeezing the aluminium spacers. No matter the exact mechanism, the cavity parameters indeed shift in qualitative agreement with the membrane in the middle model explored earlier. The change in resonance frequency is shown in figure 4.15.

However, we found out, that the introducing the piezo to the cavity seemed to very consistently break some of the tethers in the membrane degrading the mechanical performance significantly. Our suspicion is that this could be due to charging. The fabrication process can create an ununiform charge distribution and the charging from the piezo causes the membrane to break.

To isolate the piezo from the cavity mount, we cover each face of the ring piezo in contact with the membrane of the clamp with Kapton tape. The Kapton take was found to be compatible with good vacuum and was also used to attach the loose fibers and wires to the vacuum insert. The isolated piezo no longer broke the membrane, but it also no longer tuned the membrane position significantly. The Kapton tape is thicker and much softer than the aluminium spacer and thus we suspect that the the tape absorbed most of the piezo expansion. Given the experience, we decided to not explore the piezo tuning further and reverted

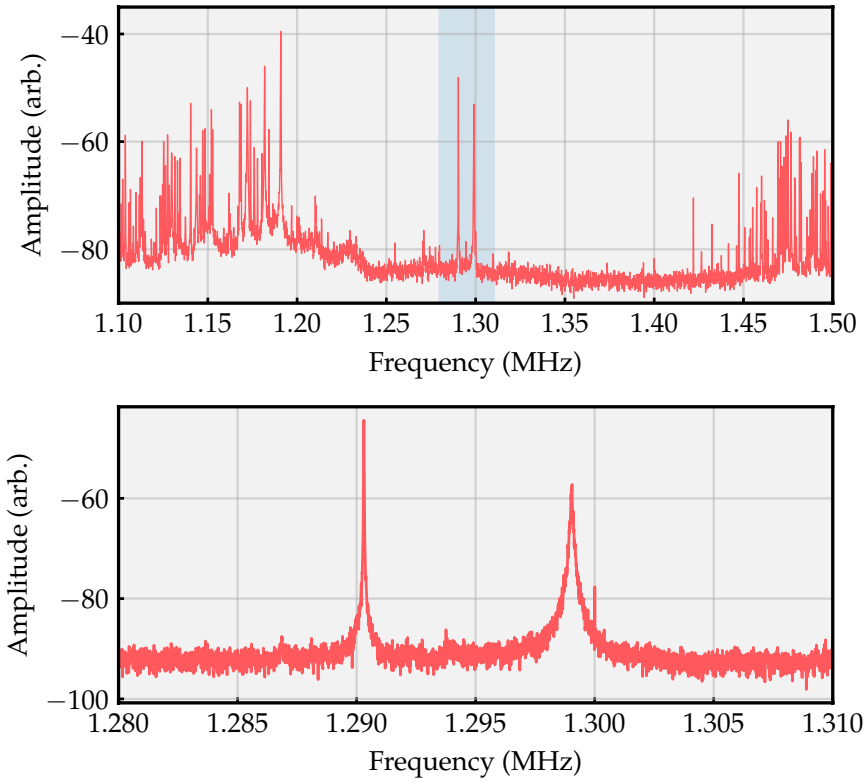

Figure 4.14: The pattern in the membrane opens a bandgap with only the defect modes present. The lower spectrum is a zoom in on the defect modes corresponding the shaded area in the broader spectrum. The defect features two modes, separated by approximately 9 kHz. The mode at $\omega_m^{(1)}/2\pi = 1.299\,\text{MHz}$ is the fundamental and one below it at $\omega_m^{(2)}/2\pi \approx 1.290\,\text{MHz}$. In this spectrum, the fundamental mode is already subject to some sideband cooling.

back to the minimal monolithic cavity design without degrees of freedom.

4.3.2 *Experimental techniques and calibration*

In this section we briefly cover the techniques used to operate the experiment and how to calibrate various parameters of interest.

Pound-Drever-Hall-technique

In the theory section, we simply stated, as is often done in theoretical considerations, that we would have the probing field on resonance with the cavity. However, since the optical wavelengths are of the order of 1 µm, even a small shift in the cavity length or a drift in the laser frequency is enough to move the

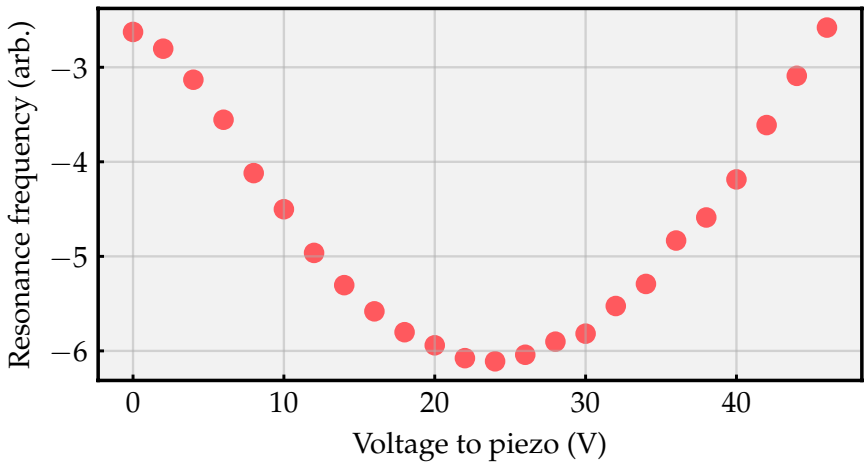

Figure 4.15: The optical resonance changes with increasing travel of the piezo in qualitative agreement with the membrane in the middle model.

probe away from the desired detuning. The typical way around this issues is to use active feedback control to either have the laser follow the shifts in the cavity or tune the cavity length according to the laser frequency. The fundamental principles are the same in either case and the only difference is whether the feedback signal is applied to the laser or to the cavity.

In the case of the fiber cavity, we have included a shear piezo to tune the cavity length. This is equivalent to scanning the cavity frequency and it is a natural lever to feedback on.

As mentioned, for the quantum feedback scheme, we would employ an on resonance probe. However, to lock the cavity, we need a proper error signal. A first guess could be to use the reflected or transmitted power and have the control unit keep them at a set level. Such a scheme works fine, but only for locking the cavity away from resonance. On resonance, any shift in frequency would reduce (increase) the transmitted (reflected) power in a same way *irrespective* of the direction of the shift! Thus, the controller would have only a 50% chance of 'guessing' the direction of the correction correctly and the cavity would inevitably shift out of resonance before any experimental protocols could be attempted.

One widely used method for deriving a proper error signal for on resonance locking is the *Pound-Drever-Hall* -technique [101]. It relies on creating sidebands on the probe beam via phase modulation at frequency ω_{PDH} and measuring the reflected signal from the cavity. The error signal is derived by demodulating the reflection at the modulation frequency. The resulting error signal features a linear slope across the resonance

with opposite signs on the different sides and thus the cavity can be maintained on resonance with the laser. Given the relatively wide cavity and available equipment, we have chosen to operate the lock with 'unresolved' modulation such that the modulation frequency is smaller than the cavity linewidth, $\omega_{mod} < \kappa$. In such case, the error signal is approximately

$$E_{PDH} \approx 2\sqrt{P_c P_{SB}} \frac{d|F(\Delta)|^2}{d\Delta} \Delta, \tag{4.28}$$

where P_c and P_{SB} are powers in the carrier and sideband respectively and $F(\Delta)$ is the reflection coefficient, defined as the ratio between incoming and reflected fields. For a symmetric cavity with mirror reflectivity r, it can be written as

$$F(\Delta_{FSR}) = \frac{r\left(\exp\left(i\Delta_{FSR}\right) - 1\right)}{1 - r^2 \exp\left(i\Delta_{FSR}\right)}, \tag{4.29}$$

where we have written the detuning as Δ_{FSR} to remind ourselves, that in this formulation, it is in units of free spectral range $\omega_{FSR} = \pi c/L$. The error signal takes different values at different sides of the cavity, as shown in figure 4.16.

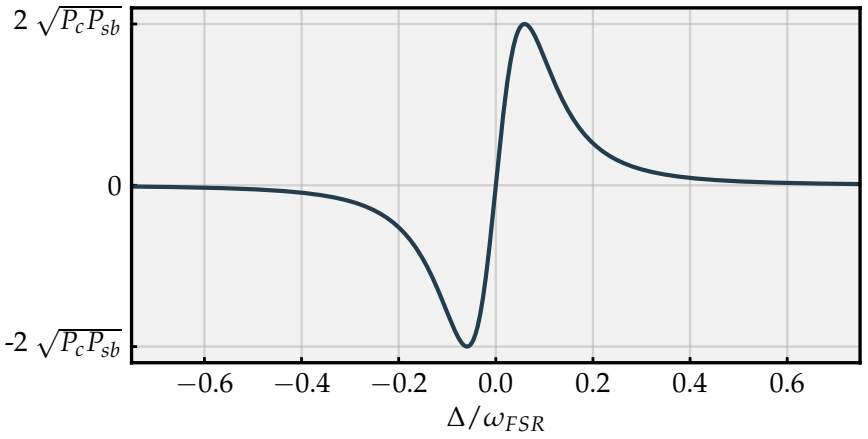

Figure 4.16: The PDH error signa in the slow modulation regime is linear accross the cavity resonance allowing for reliable on resonance lock. The height of the signal is determined by the product of the power in the carrier and the power in the sideband with the maximum found when $P_c = P_{SB}$. Here, we the error signal is shown for a symmetric cavity with both mirrors having reflectivity $r = 0.95$.

In the experiment, we modulate the probe beam typically at frequency between 60 and 80 MHz. However, frequencies near 80 MHz interfere with the feedback beam causing noise in the reflected signal. In principle, this is only an aesthetic problem

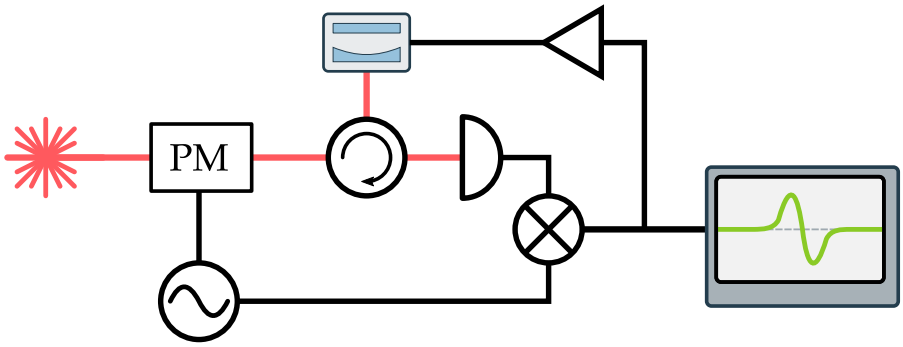

Figure 4.17: Implementation of the PDH locking scheme. The probe laser is phase modulated at frequency ω_{mod} and we measure the reflected amplitude. The photocurrent is demodulated with a signal derived from the the same source as the modulation. This brings the desired error signal to DC where it can be fed to a PI controller to lock the cavity to the laser.

if the frequency is sufficiently far away from the mechanical frequency. Modulation and demodulation signals are generated with the same function generator using two channels and the relative phase between the channels is optimized already at the generator. The photocurrent from the detector[20] is demodulated with a mixer[21]. The output of the mixer is amplified and filtered[22] and a PI controller[23] together with a homebuilt low noise amplifier is used to control the cavity length.

Quantifying fiber imperfections

The are often minor imperfections in the fiber mirror such as angle between the fiber core axis and the fiber face, off centred indentation or asymmetry. Because of the imperfections, fraction of the light from the cavity is scattered to modes other than the fiber mode. To quantify the fraction of cavity light coupling back to the fiber mode, we use an approach where we compare a fiber mirror to a more ideal reflector[102].

First, we measured reflected power from the cavity P_f via a circulator. Then, the cavity was replaced with a retroreflector and the reflected power P_{rr} was recorded. Then, the fraction of light scattered the modes other than the fiber mode is the ratio of these to powers

$$\alpha = \frac{P_f}{P_{rr}}. \tag{4.30}$$

20 Thorlabs PDA05CF2
21 Minicircuits ZP-3+
22 Stanford research SR560
23 New focus LB1005-S

The mechanism for scattering is similar for both the prompt reflection and the cavity output. Hence, only a fraction $\sqrt{\alpha}$ of the cavity light is routed to the fiber mode and makes its way to the detector. For the particular fiber mirror forming one half of the cavity, we measured combined value including losses in the fiber $\alpha L^2 = 0.42$.

Mirror transmissivities

To verify the transmissivities of the mirror coatings, we peformed a comparatively crude measurement where we recorded the incident light on each mirror and measured the transmitted light. The fiber mirror required an additional step in order to measure the incident light on the fiber mirror. Simply measuring power at the input of the fiber would underestimate due to losses in fiber splices or at the input coupling. Thus, we first measured the light transmitted through the fiber and then cut the mirrored fiber after the splice to the connecting fiber to measure the power in the fiber. The measurements yielded $T_{exo} = 250$ ppm and $T_f = 2140$ ppm, significantly higher than specified. Based on the measured transmissivities, we expect the cavity to have approximately 3000 finesse.

Cavity linewidth calibration

Cavity linewidth κ is an important parameter in the optomechanical model. In principle it could be estimated from the knowledge of the mirror coatings or even from knowing the speed at which the frequency is swept across the resonance, but in practice such considerations are both unnecessary and inaccurate. Instead, we will modulate the probe beam at frequency $\omega_{mod} \gg \kappa$ creating sidebands around the carrier at $\pm\omega_{mod}$. When the cavity length is swept across the resonance, we see three reflection dips, two corresponding to the sidebands and one corresponding to the carrier. Based on the distance between the carrier dip and the sideband dip, the time axis is converted into frequency.

Fiber cavities present an additional subtlety compared to typical free space ones. Any observed light reflected from the cavity must travel via the fiber mode and thus is subject to spatial filtering [103]. As a consequence, the cavity reflection is no longer a simple Lorentzian, but also contains a dispersive term. The normalized reflected power is thus

$$P_{out}(\nu) = 1 - \mathcal{L}\left(\frac{1}{1+\nu^2} - \mathcal{A}\frac{\nu}{1+\nu^2}\right), \tag{4.31}$$

where we have introduced normalized detuning $\nu = 2\Delta/\kappa$, the cavity dip depth $\mathcal{L}$ and the asymmetry parameter $\mathcal{A}$ determining

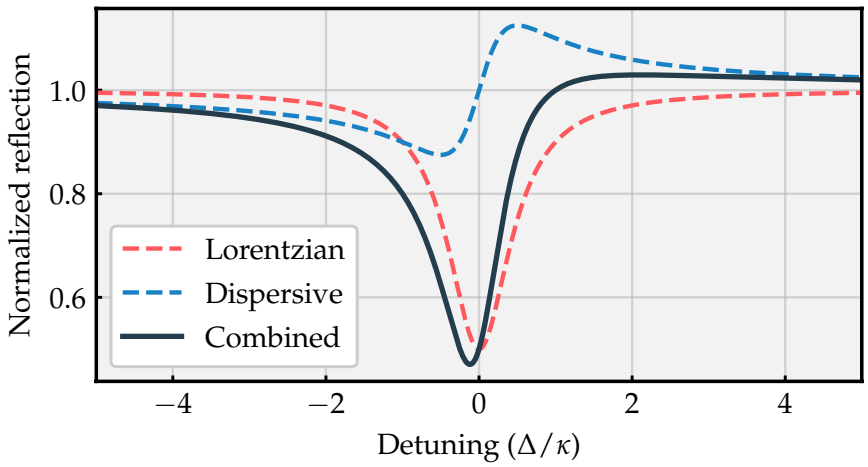

Figure 4.18: The cavity reflection via a fiber mirror is a conbination of a Lorentzian and a dispersive feature.

the relative strength of the dispersive feature. The model fits the measured reflection well, as seen in figure 4.19 and yields optical linewidth of $\kappa/2\pi = 343.8 \pm 11.9$ MHz.

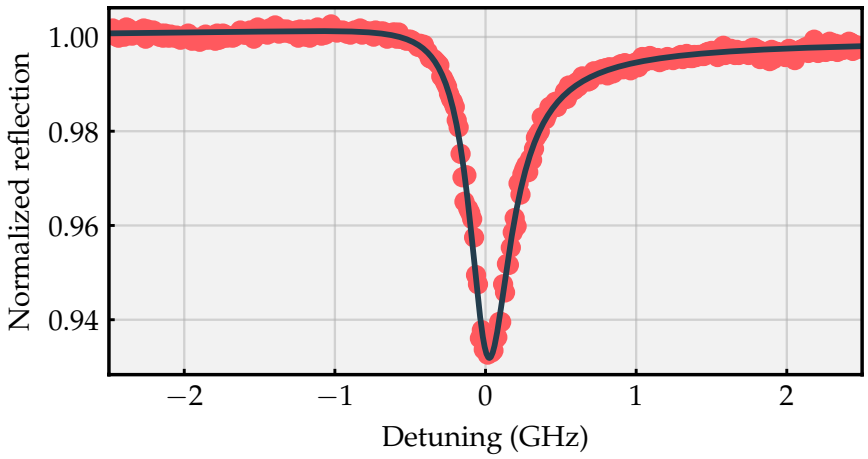

Figure 4.19: The linewidth of the optical cavity is found via a simple fit. Phase modulation at $\omega_{MOD} \gg \kappa$ is used to create frequency markers and the cavity length is swept over the resonance. The asymmetric lineshape is a feature of the fiber cavity. The cavity linewidth is approximately 343.8 MHz. In the figure, the sidebands are visible at ± 2 GHz.

Cavity length measurement

In principle, the cavity length does not enter the optomechanical model describing the experiment. However, it is useful figure

to know in order to translate the measured cavity linewidth to optical finesse that can be compared to the expected value obtained with the mirror transmissivities. Finesse can be interpreted as the average number of round trips a photon makes in a cavity before exiting via one of the ports. It connects to the cavity length and losses as

$$\mathcal{F} \approx \frac{2\pi}{T_1 + T_2 + T_L}, \mathcal{F} = \frac{c}{2L\kappa}, \tag{4.32}$$

where T_1 and T_2 are the transmissivities of the cavity mirrors, T_L the loss rate and L the cavity length.

As a first approximation, we estimatee the cavity length with a microscope using the known fiber diameter as a measure. Based on the image, the cavity length is between 50-100 µm. For a more accurate length, we measured the free spectral range of the cavity. We used a tunable laser to find the approximate wavelength of two adjacent resonances at $\lambda_1 = 1542.38\,\text{nm}$ and $\lambda_2 = 155.78\,\text{nm}$. A useful trick is to employ two lasers. The cavity length is swept such that the cavity resonance is found. Keeping the original laser on and still sweeping the cavity length, a tunable laser is routed to the cavity and the wavelength is tuned until the same resonance is found at a different wavelength. The laser is then further tuned until the resonances coincide. Using the definition of FRS in equation 2.9, we find

$$\frac{1}{\lambda_1} - \frac{1}{\lambda_2} = \frac{c}{2L}. \tag{4.33}$$

Solving for the cavity length, we find $L = 96.7\,\mu\text{m}$.

Optomechanical coupling

In principle, the optomechanical coupling is unnecessary to determine the final occupation. However, it is necessary to determine the quantum cooperativy and where the system stands with respect to the mirror noise. For the fiber cavity setup, the most convenient way to characterize the coupling is to consider the frequency shift arising from dynamical backation. In the unresolved sideband limit where $\kappa \gg \omega_m$, the frequency shift simplifies to

$$\delta\omega_m(\Delta) = g_0^2 n_{cav} \left(\frac{2\Delta}{\left(\frac{\kappa}{2}\right)^2 + \Delta^2} \right), \tag{4.34}$$

where Δ is the detuning of the beam and κ the linewidth of the optical cavity. For most realizations of the fiber cavity we have measured linewidths between 200 Mhz and 1 GHz. With

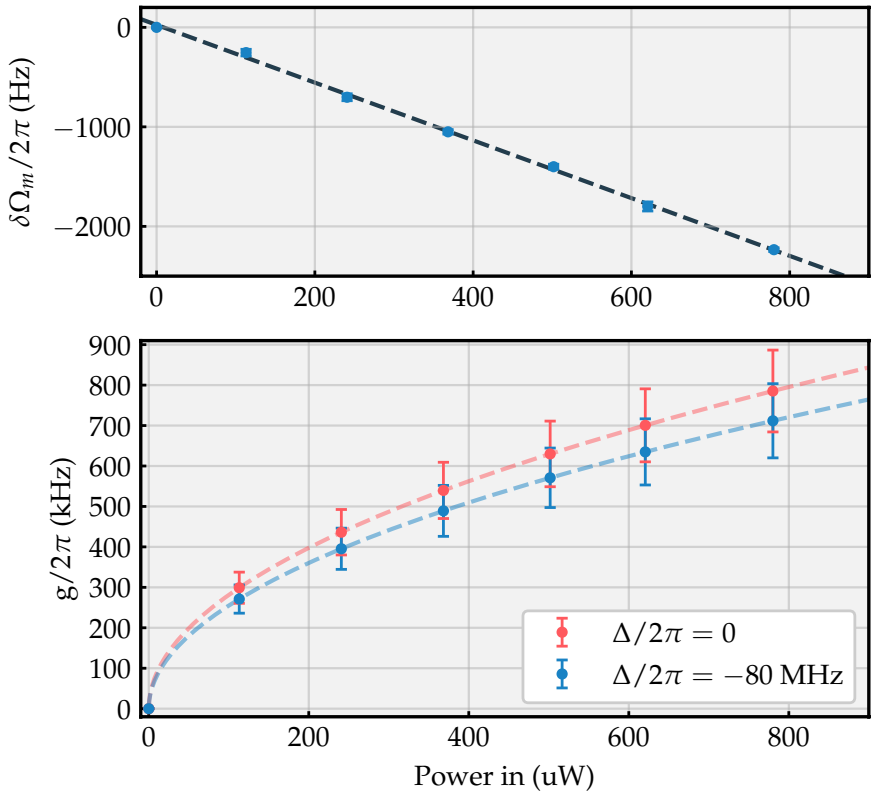

Figure 4.20: In the unresolved sideband regime, a detuned beam shifts the cavity frequency linearly and the magnitude of the shift is proportional to the field enhanced optomechanical coupling g that is in turn proportional to the intracavity photon number that in turn depends on the input light field. We record the frequency shift for different optical powers and with the detuning and the cavity linewidth known, the coupling can be extracted with a straightforward linear fit. The frequency shift (upper graph) shows a clear linear relation to the input power of the detuned field measured at the input of the cavity fiber. Based on the shift, we infer the corresponding coupling. With a detuning of the same order of magnitude as the cavity linewidth, we must take into account, that the probe beam on resonance results into higher intracavity photon number and hence a larger coupling g. In the lower plot, the blue dots and the curve and the dots correspond to data and fits based on the acquired data and the red dots and line include a correction for on resonance driving.

mechanical resonance frequency at most 1.5 MHz, the cavity is extremely unresolved and the above approximation very good.

In practice, we lock a weak probe beam on resonance with a cavity. Then, an AOM is used to derive another beam from the same laser source detuned -80 MHz from the probe and we measure the frequency shift versus intracavity power derived from knowledge of the input power to the cavity and cavity

linewidth. It is possible, that the probe already causes a shift due to nonzero detuning, but since the probe power is kept constant, the linear relation still holds but with a constant offset, such that the total frequency shift compared to the intrinsic mechanical frequency is $\delta\omega_m' = \delta\omega_m^{(probe)} + \delta\omega_m^{(c)}$.

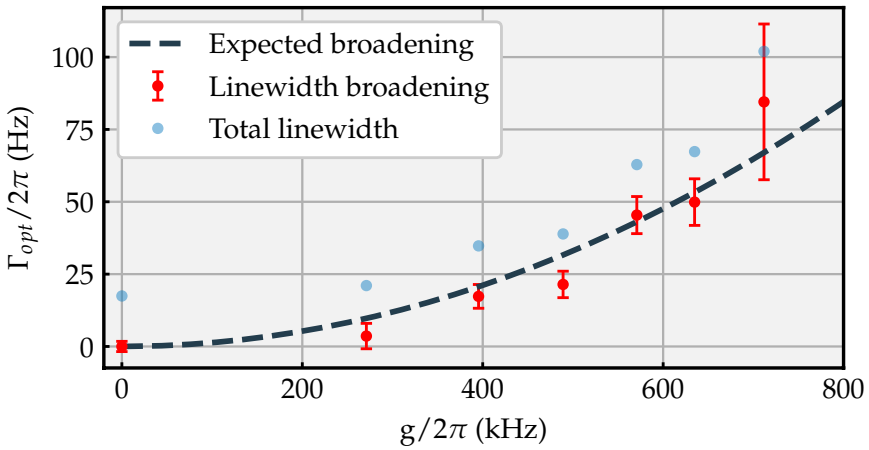

Figure 4.21: The linewidth of the mechanical resonance follows the prediction of the dynamical backaction model. The dashed line is the expected broadening given the coupling inferred from the frequency shift. Each point corresponds to average of five linewidths at a given coupling. There is a good agreement between the predicted increase and the measured linewidth. It should be noted that the probe beam is likely slightly red detuned and thus already cools the mode somewhat.

In principle, an even more 'black box' measurement can be made, where we simply connect the measured input power to the observed frequency shift and the field enhanced coupling g such that the conversion factor accounts for all the losses between the input fiber and the cavity. In fact, for the feedback protocol and calibration of the results, there is no need to know the single photon coupling and we can make use of the more accurately known[24] field enhanced coupling. An example of one such characterization is shown in figure 4.20. The shift is indeed linear as the model predicts. Based on the measurement, with the experimentally relevant probe power, the field enhanced optomechanical coupling is $g/2\pi \approx 650\,\mathrm{kHz}$.

It is important to keep in mind, that it is still g_0 that determines the effect of mirror noise. The mirror noise couples to the output phase via similar optomechanical coupling and thus the proportionality of the it and the membrane motion stays

24 Measuring g requires only knowledge of the cavity linewidth and the detuning of the cooling beam both of which are known very accurately.

constant for all intracavity powers. In order to determine the single photon coupling, we estimate the losses in the fiber and the cavity coupling efficiency to find $g_0/2\pi \approx 2360\,\mathrm{hz}$.

Mechanical linewidth

Typical soft clamped resonators feature linewidths of only a few millihertz and thus well below the bandwidth of most practical spectrum analyzers. The typical characterization routine instead involves exciting the membrane motion well above thermal energy level either via optical driving or mechanical excitation with a piezo. The excitation is then turned off, and the resonator is left to decay freely. Fitting the decay trace with an exponential $\exp(-\Gamma_m t)$ then yields the mechanical linewidth. Typically, the measurements are done in a dedicated interferometer, where an entire wafer, typically around 20 membranes, can be characterized simultaneously without venting the chamber inbetween.

Without baking, the interferometer reaches vacuum of approximately $3 \cdot 10^{-7}$ mbar. This pressure still limits the quality factor of membranes somewhat. Based on measuring the effect of pressure to the quality factor, we would expect an approximately 10% boost in Q in the better, below 10^{-7} mbar vacuum achieved in the fiber cavity UHV chamber.

Homodyne spectrum

The spectrum analyser measures the mechanical spectrum, but in voltage units. To connect the measured spectrum to the motion of the membrane, there needs to be a conversion factor between voltage and position[25]. In the fiber cavity experiment, we choose to exploit two features of the system. First, there is absolute certainty on the bath temperature. In cryogenic environments in liquid helium flow cryostats, despite the temperature sensor on the cold finger reading approximately 4 K, we have often seen, that the membrane thermalizes to only 10 K. In room temperature, however, the membrane has essentially unlimited time to thermalize to the room temperature and is thus taken to be at 300 K. Second, the mechanical linewidth is very accurately known and thus, we know the thermal occupation of the mechanical resonator with very little uncertainty. Then, integral over the measured spectrum should correspond to the thermal occupation and the conversion factor is found.

In practice, there are a couple fine points that should be accounted for when calibrating the spectra. First of all, we wish to do the calibration with the exact experimental setup we wish to use during the feedback cooling runs and this necessitates

25 Either in meters or in units of zero point fluctuation.

a strong probe. As we recall from chapter 2, the bath has a contribution from the quantum backation. Thus, the thermal occupation becomes

$$n_{th}^{QBA} = n_{th}\,(1 + C_q)\,. \tag{4.35}$$

The second complication is due to the the feedback cooing beam that also *sideband* cools the mechanics. The optical spring is found from the cooled mechanical peak. We may further approximate $\Gamma_{opt} \approx \Gamma_{om}$, where Γ_{om} is the sideband cooled linewidth, since the initial mechanical linewidth is typically around 10 mHz, and therefore much smaller than the broadened peak, typically at tens of Hz. With sideband cooling and accounting for the quantum backation of the probe, we find the mechanical occupation to be

$$n_{SB} = \frac{n_{th}^{QBA}\Gamma_m}{\Gamma_{opt}} + n_{min}^{SB}, \tag{4.36}$$

where n_{min}^{SB} is the already familiar sideband cooling limit

$$n_{min}^{SB} = \left(\frac{\frac{\kappa^2}{4} + (\Delta - \omega_m)^2}{\frac{\kappa^2}{4} + (\Delta + \omega_m)^2} - 1\right)^{-1}, \tag{4.37}$$

which accounts for the QBA of the cooling beam.

With the occupation known, the calibration is a simple matter of finding a constant K such that

$$\int K\bar{S}_{VV}(\Omega)\frac{d\Omega}{2\pi} = \int \bar{S}_{QQ}(\Omega)\frac{d\Omega}{2\pi} = 2n_{SB} + 1. \tag{4.38}$$

Interferometer visibility

To measure and optimize the visibility of the interferometer, we set the signal arm and LO power to the same value and block one port of the balanced detector. The maximum and minimum measured voltages then relate to the visibility as

$$\mathcal{V} = \frac{V_{max} - V_{min}}{V_{max} - V_{min}}, \tag{4.39}$$

where V_{max} and V_{min} are the maximum and minimum voltages respectively.

Detection efficiency

In the theoretical background of feedback control, we saw that is of critical importance to extract as much information as possible per unit of backation, i.e. to have as high measurement efficiency

as possible. The *measurement* efficiency η_m depends on the *detection* efficiency η_D that in turn is a measure of what portion of the measured light comes from the cavity. In the case of the fiber cavity, the total detection efficiency is

$$\eta_D = \varepsilon \cdot \eta_c \cdot \sqrt{\alpha} \cdot L \cdot \mathcal{V} \cdot P_{QE}, \tag{4.40}$$

where ε is the cavity mode matching, η_c the outcoupling efficiency, α the parameter accounting for an unideal fiber mirror, L the combined losses in the path from the cavity to the detector, $\mathcal{V}$ the interferometer visibility and finally P_{QE} the quantum efficiency of the detector. We use the manufacturer number for the quantum efficiency and measure other quantities independently. For some of the parameters, we only measure the product of two or more individual parameters. The measured values are shown in table 4.1.

Outcoupling efficiency	$\eta_c \cdot \epsilon$	0.04
Visibility	$\mathcal{V}$	0.9
Fiber losses	$\sqrt{\alpha} \cdot L$	0.42
Quantum efficiecny	P_{QE}	0.8

Table 4.1: Individual decomposition of detection efficiency.

The total detection efficiency of the detection chain is thus

$$\eta_D = 1.21\%. \tag{4.41}$$

Assuming $C_q = 1$, this corresponds optimal control occupation floor of $n_{min}^{opt} \approx 6.0$. With a large cooperativity, the limit becomes $n_{min}^{opt} \approx 4.1$. It is thus obvious, that in order to prepare the resonator in below unity occupation, the detection efficiency must be improved. Luckily, relatively straightforward steps are possible.

First, based on the mirror coatings, we expect that the outcoupling efficiency through the fiber mirror would be up to 89%. To have the effective outcoupling $\eta_c' = \varepsilon\eta_c$ approach this value, mode matching needs to be improved. Low mode matching efficiency is not intrinsic property of the fiber mirrors and values more than $\varepsilon \geqslant 0.75$ are within reach by improving the optical cavity alignment. Alternatively, choosing a more ideal fiber mirror can improve the mode matching.

Improving mode matching to 0.8 would, without any other improvements, improve detection efficiency to 22%. With $C_q = 1$, the optimal control limit becomes $n_{min}^{opt} = 1.01$, just barely above unity. Increasing quantum cooperativity further would then allow for below unity occupation. Choosing a better fiber and

improving losses in splices and feedthroughs should allow for increasing the detection efficiency up to 30% without any other modifications in the cavity assembly. However, significantly improving the cavity alignment will likely require finer positioning stage than the one used previously but otherwise, the alignment procedure should stay relatively intact.

4.4 FEEDBACK COOLING CLOSE TO THE QUANTUM GROUND SATE

We use a single main filter, centred at $\omega_{FB}/2\pi = 1.34\,\text{MHz}$ with linewidth $\Gamma_{FB}/2\pi = 77.86\,\text{kHz}$. As the electronic gain of the filter is increase, the mechanical peak flattens and broadens, as seen in figure 4.22. The mechanical frequency also shifts with increasing gain. This is due to unideal phase such that the filter function is not purely imaginary. In addition to the main filter, we employ an auxiliary filter at $\omega_{FB}^{aux}/2\pi = 1.195\,\text{MHz}$ with linewidth $\Gamma_{FB}^{aux}/2\pi = 9.716\,\text{kHz}$ to stabilize an out of bandgap mode that the main filter excites.

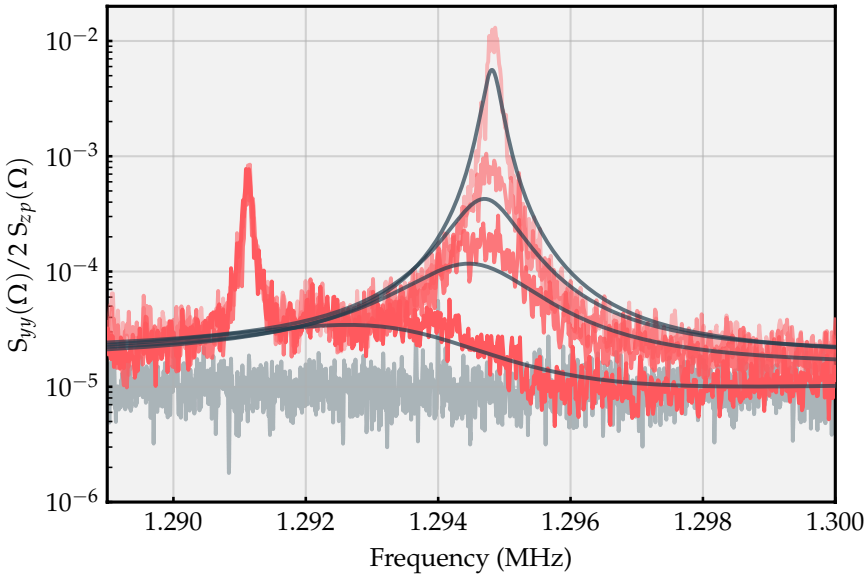

Figure 4.22: The mechanical mode broadens and flattens, that is becomes cooler as the feedback gain is increased from light to dark red. The gray spectrum corresponds to the shot noise level and the solid charcoal lines are fits. 'The peak around 1.291 MHz is very likely a spurious mechanical mode.

In the experiment, the probe quantum cooperativity is $C_q^p = 0.1$ and the corresponding optimal control limit $n_{min}^{opt} = 14.4$. The electronic gain of the main filter is increased until we reached

a mechanical instability that we were unable to stabilize with additional auxiliary filters. The spectrum with the lowest occupation is shown in figure 4.23 and the occupation as a function electronic gain in figure 4.24.

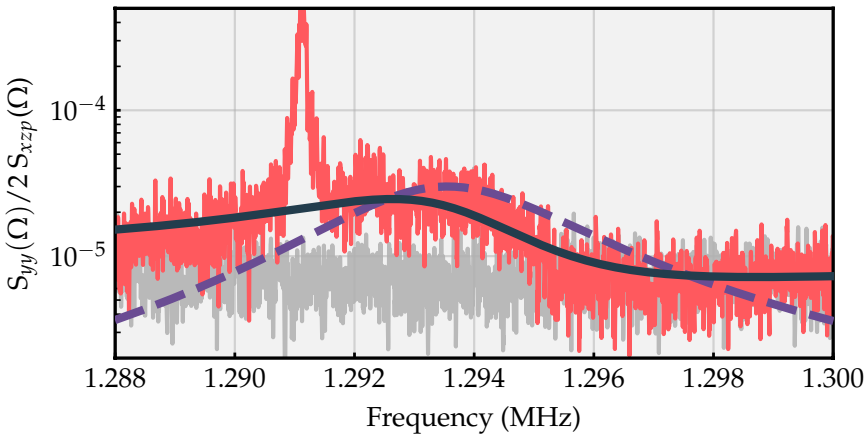

Figure 4.23: The lowest occupation reached is approximately $n_{min} = 20.3 \pm 0.5$. The red spectrum correspond to the measured mechanical spectrum, S_{yy}. The dark gray line is fitted S_{yy} and the dashed purple line is the inferred mechanical motion S_{xx}. The light gray line corresponds to the shot noise level.

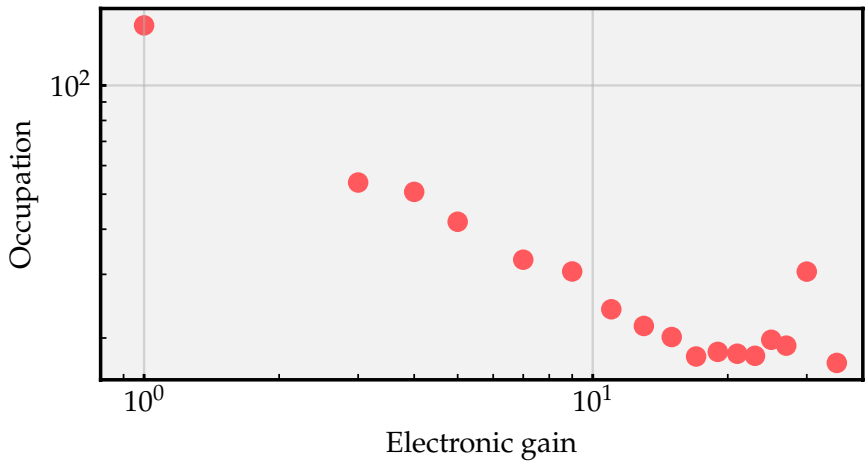

Figure 4.24: The occupation falls with increasing gain until the imprecision starts dominating.

4.4.1 *Limiting factors*

The initial experiment was limited by the low detection efficiency. Even with C_q approaching infinity, the experiment would be unable to cool the resonator's mode to below unity occupation. In fact, the lowest occupation achieved is already close to the optimal control limit. Possible reason for excess occupation include technical noise such as laser noise, unideal filter or mirror phase noise. Detection efficiency is most limited by mode matching and increasing it should improve detection efficiency enough to make ground state cooling feasible, assuming other noises do not prove to be a limiting factor.

The low mass membrane design in the fiber cavity also exhibited high enough coupling to allow for $C_q > 1$ with enough intracavity power. We have experimentally confirmed that operating at such power is possible without onset of bistability, but due to power budget and equipment limitations, we chose to work at a lower C_q for the cooling experiment.

Although likely unnecessary for the next iteration, further improvements could be found with higher optical finesse. Recently, fiber based optomechanical cavities have been demonstrated with Finesse up to 165000 [104]. Smaller optical linewidth would increase quantum cooperativity given that other system parameters stay constant. Alternatively, a longer fiber-fiber cavity would allow for easier sample exchange and, at the same time, reduce optical linewidth. Fiber cavities up to 1.5 mm in length have been demonstrated [87], more than enough to fit the 400 to 500 µm thick silicon frame of our membranes.

5 CONCLUDING REMARKS

In the previous sections, we have covered two room temperature experiments. First, in a proof or principle experiment, we have demonstrated an integrated optomechanical transducer in a clinical MRI scanner. The performance of the first generation device was not on par with state of the art electronic amplifiers, but as a lightweight optical device, it could enable operation in a high magnetic field or in a multi-coil-setup. The most important improvement would be individual vacuum packaging of the device such that it could function as a truly stand-alone device. Other avenues would include investigating wireless biasing and targeting telecom wavelengths.

Second, we have build a compact, low phase noise cavity that together with a low mass soft-clamped membrane enables quantum optomechanical experiments at room temperature. Based on the measured coupling, reaching $C_q > 1$ requires field enhanced coupling of $g/2\pi \approx 2\,\mathrm{MHz}$. We verified that the optomechanical system operates stably at the required intracavity power. We further cooled the resonator's mode to $n_{min} \approx 20.3$ phonons at $C_q = 0.1$.

For the first generation optomechanical cavity, the final occupation was limited by low detection efficiency. More specifically, the detection efficiency suffered from poor mode matching between the cavity mode and the fiber mirror. Poor mode matching is not an intrinsic property of the fiber mirrors and hence, the detection efficiency could be boosted in subsequent cavity assemblies. With improved mode matching and reduced losses, the achievable detection efficiency allows for cooling the resonator to below unity occupation without other modifications to the system, barring other noise sources.

These experiments present steps towards realizing optomechanical *technologies* both for biomecical applications and for the nascent quantum internet.

BIBLIOGRAPHY

[1] J.C. Maxwell. *A Treatise on Electricity and Magnetism*. Clarendon Press, 1873.

[2] William Crookes. "XV. On attraction and repulsion resulting from radiation". In: *Philosophical Transactions of the Royal Society of London* 164 (1874), pp. 501–527. DOI: 10.1098/rstl.1874.0015. eprint: https://royalsocietypublishing.org/doi/pdf/10.1098/rstl.1874.0015. URL: https://royalsocietypublishing.org/doi/abs/10.1098/rstl.1874.0015.

[3] P.N. Lebedev. "Experimental Examination of Light Pressure". In: *Annalen der Physik* 6.433 (1901).

[4] E. F. Nichols and G. F. Hull. "A Preliminary Communication on the Pressure of Heat and Light Radiation". In: *Phys. Rev. (Series I)* 13 (5 1901), pp. 307–320. DOI: 10.1103/PhysRevSeriesI.13.307. URL: https://link.aps.org/doi/10.1103/PhysRevSeriesI.13.307.

[5] A. Ashkin. "Acceleration and Trapping of Particles by Radiation Pressure". In: *Phys. Rev. Lett.* 24 (4 1970), pp. 156–159. DOI: 10.1103/PhysRevLett.24.156. URL: https://link.aps.org/doi/10.1103/PhysRevLett.24.156.

[6] V.B. Braginsky and A.B. Manukin. "Ponderomotive effects of electromagnetic radiation". In: *J. Exptl. Theoret. Phys.* (1967).

[7] V.B. Braginsky, A.B. Manukin, and M. Yu. Tikhonov. "Investigation of dissipative ponderomotive". In: *J. Exptl. Theoret. Phys.* (1970).

[8] B. P. Abbott et al. "Observation of Gravitational Waves from a Binary Black Hole Merger". In: *Phys. Rev. Lett.* 116 (6 2016), p. 061102. DOI: 10.1103/PhysRevLett.116.061102. URL: https://link.aps.org/doi/10.1103/PhysRevLett.116.061102.

[9] F Acernese et al. "Advanced Virgo: a second-generation interferometric gravitational wave detector". In: *Classical and Quantum Gravity* 32.2 (2014), p. 024001. DOI: 10.1088/0264-9381/32/2/024001. URL: https://doi.org/10.1088/0264-9381/32/2/024001.

[10] T. P. Purdy, R. W. Peterson, and C. A. Regal. "Observation of Radiation Pressure Shot Noise on a Macroscopic Object". In: *Science* 339.6121 (2013), pp. 801–804. ISSN: 0036-8075. DOI: 10.1126/science.1231282. eprint: https://science.sciencemag.org/content/339/6121/801.full.pdf. URL: https://science.sciencemag.org/content/339/6121/801.

[11] M. Underwood et al. "Measurement of the motional sidebands of a nanogram-scale oscillator in the quantum regime". In: *Phys. Rev. A* 92 (6 2015), p. 061801. DOI: 10.1103/PhysRevA.92.061801. URL: https://link.aps.org/doi/10.1103/PhysRevA.92.061801.

[12] J. D. Teufel et al. "Sideband cooling of micromechanical motion to the quantum ground state". In: *Nature* 475.7356 (2011), pp. 359–363. ISSN: 1476-4687. DOI: 10.1038/nature10261. URL: https://doi.org/10.1038/nature10261.

[13] Jasper Chan et al. "Laser cooling of a nanomechanical oscillator into its quantum ground state". In: *Nature* 478.7367 (2011), pp. 89–92. ISSN: 1476-4687. DOI: 10.1038/nature10461. URL: https://doi.org/10.1038/nature10461.

[14] Massimiliano Rossi et al. "Measurement-based quantum control of mechanical motion". In: *Nature* 563.7729 (2018), pp. 53–58. ISSN: 1476-4687. DOI: 10.1038/s41586-018-0643-8. URL: https://doi.org/10.1038/s41586-018-0643-8.

[15] Yannick Seis et al. *Ground State Cooling of an UltracoherentElectromechanical System*. 2021. arXiv: 2107.05552 [quant-ph].

[16] T. P. Purdy et al. "Strong Optomechanical Squeezing of Light". In: *Phys. Rev. X* 3 (3 2013), p. 031012. DOI: 10.1103/PhysRevX.3.031012. URL: https://link.aps.org/doi/10.1103/PhysRevX.3.031012.

[17] S. Barzanjeh et al. "Stationary entangled radiation from micromechanical motion". In: *Nature* 570.7762 (2019), pp. 480–483. ISSN: 1476-4687. DOI: 10.1038/s41586-019-1320-2. URL: https://doi.org/10.1038/s41586-019-1320-2.

[18] Junxin Chen et al. "Entanglement of propagating optical modes via a mechanical interface". In: *Nature Communications* 11.1 (2020), p. 943. ISSN: 2041-1723. DOI: 10.1038/s41467-020-14768-1. URL: https://doi.org/10.1038/s41467-020-14768-1.

[19] C. F. Ockeloen-Korppi et al. "Stabilized entanglement of massive mechanical oscillators". In: *Nature* 556.7702 (2018), pp. 478–482. ISSN: 1476-4687. DOI: 10.1038/s41586-018-0038-x. URL: https://doi.org/10.1038/s41586-018-0038-x.

[20] Ralf Riedinger et al. "Remote quantum entanglement between two micromechanical oscillators". In: *Nature* 556.7702 (2018), pp. 473–477. ISSN: 1476-4687. DOI: 10.1038/s41586-018-0036-z. URL: https://doi.org/10.1038/s41586-018-0036-z.

[21] T. Palomaki et al. "Entangling Mechanical Motion with Microwave Fields". In: *Science* 342 (2013), pp. 710–713. ISSN: 0036-8075. DOI: 10.1126/science.1244563. URL: http://www.sciencemag.org/cgi/doi/10.1126/science.1244563.

[22] M. Bahrami et al. "Proposal for a Noninterferometric Test of Collapse Models in Optomechanical Systems". In: *Phys. Rev. Lett.* 112 (21 2014), p. 210404. DOI: 10.1103/PhysRevLett.112.210404. URL: https://link.aps.org/doi/10.1103/PhysRevLett.112.210404.

[23] William Marshall et al. "Towards Quantum Superpositions of a Mirror". In: *Phys. Rev. Lett.* 91 (13 2003), p. 130401. DOI: 10.1103/PhysRevLett.91.130401. URL: https://link.aps.org/doi/10.1103/PhysRevLett.91.130401.

[24] Alberto Beccari et al. *Strained crystalline nanomechanical resonators with ultralow dissipation*. 2021. arXiv: 2107.02124 [cond-mat.mes-hall].

[25] H. J. Kimble. "The quantum internet". In: *Nature* 453.7198 (2008), pp. 1023–1030. ISSN: 1476-4687. DOI: 10.1038/nature07127. URL: https://doi.org/10.1038/nature07127.

[26] *QphoX*. https://qphox.eu/. Accessed 22.08.2021.

[27] Andreas Wallucks et al. "A quantum memory at telecom wavelengths". In: *Nature Physics* 16.7 (2020), pp. 772–777. ISSN: 1745-2481. DOI: 10.1038/s41567-020-0891-z. URL: https://doi.org/10.1038/s41567-020-0891-z.

[28] Anders Simonsen. "Sensitive electro-optical transduction through resonant electro- and optomechanics". PhD thesis. University of Copenhagen, 2019.

[29] Markus Aspelmeyer, Tobias J. Kippenberg, and Florian Marquardt. "Cavity optomechanics". In: *Rev Mod Phys* 86 (4 2014), pp. 1391–1452. DOI: 10.1103/RevModPhys.86.1391. URL: https://link.aps.org/doi/10.1103/RevModPhys.86.1391.

[30] Warwick Bowen and Gerard Milburn. *Quantum Optomechanics*. CRC Press, 2015.

[31] Nicholas Nassim Taleb. *Skin in the Game*. Penguin Random House LLC., 2017.

[32] R. W. Andrews et al. "Bidirectional and efficient conversion between microwave and optical light". In: *Nature Physics* 10.4 (2014), pp. 321–326. ISSN: 1745-2481. DOI: 10.1038/nphys2911. URL: https://doi.org/10.1038/nphys2911.

[33] A. P. Higginbotham et al. "Harnessing electro-optic correlations in an efficient mechanical converter". In: *Nature Physics* 14.10 (2018), pp. 1038–1042. ISSN: 1745-2481. DOI: 10.1038/s41567-018-0210-0. URL: https://doi.org/10.1038/s41567-018-0210-0.

[34] Moritz Forsch et al. "Microwave-to-optics conversion using a mechanical oscillator in its quantum ground state". In: *Nature Physics* 16.1 (2020), pp. 69–74. ISSN: 1745-2481. DOI: 10.1038/s41567-019-0673-7. URL: https://doi.org/10.1038/s41567-019-0673-7.

[35] G. Arnold et al. "Converting microwave and telecom photons with a silicon photonic nanomechanical interface". In: *Nature Communications* 11.1 (2020), p. 4460. ISSN: 2041-1723. DOI: 10.1038/s41467-020-18269-z. URL: https://doi.org/10.1038/s41467-020-18269-z.

[36] Mohammad Mirhosseini et al. "Superconducting qubit to optical photon transduction". In: *Nature* 588.7839 (2020), pp. 599–603. ISSN: 1476-4687. DOI: 10.1038/s41586-020-3038-6. URL: https://doi.org/10.1038/s41586-020-3038-6.

[37] Simon Hönl et al. *Microwave-to-optical conversion with a gallium phosphide photonic crystal cavity*. 2021. arXiv: 2105.13242 [physics.optics].

[38] William Hease et al. "Bidirectional Electro-Optic Wavelength Conversion in the Quantum Ground State". In: *PRX Quantum* 1 (2 2020), p. 020315. DOI: 10.1103/PRXQuantum.1.020315. URL: https://link.aps.org/doi/10.1103/PRXQuantum.1.020315.

[39] Rishabh Sahu et al. *Quantum-enabled interface between microwave and telecom light*. 2021. arXiv: 2107.08303 [quant-ph].

[40] I. C. Rodrigues, D. Bothner, and G. A. Steele. "Coupling microwave photons to a mechanical resonator using quantum interference". In: *Nature Communications* 10.1 (2019), p. 5359. ISSN: 2041-1723. DOI: 10.1038/s41467-019-12964-2. URL: https://doi.org/10.1038/s41467-019-12964-2.

[41] D.J. Griffiths. *Introduction to quantum mechanics*. Pearson Education, 2005.

[42] Jeremy B. Clark et al. "Sideband cooling beyond the quantum backaction limit with squeezed light". In: *Nature* 541.7636 (2017), pp. 191–195. ISSN: 1476-4687. DOI: 10.1038/nature20604. URL: https://doi.org/10.1038/nature20604.

[43] J. D. Thompson et al. "Strong dispersive coupling of a high-finesse cavity to a micromechanical membrane". In: *Nature* 452.7183 (2008), pp. 72–75. ISSN: 1476-4687. DOI: 10.1038/nature06715. URL: https://doi.org/10.1038/nature06715.

[44] Vincent Dumont et al. "Flexure-tuned membrane-at-the-edge optomechanical system". In: *Opt. Express* 27.18 (2019), pp. 25731–25748. DOI: 10.1364/OE.27.025731. URL: http://www.opticsexpress.org/abstract.cfm?URI=oe-27-18-25731.

[45] A M Jayich et al. "Dispersive optomechanics: a membrane inside a cavity". In: *New Journal of Physics* 10.9 (2008), p. 095008. DOI: 10.1088/1367-2630/10/9/095008. URL: https://doi.org/10.1088/1367-2630/10/9/095008.

[46] A. W. Leissa. *Vibration of Plates*. NASA, 1969.

[47] S Schmid, L. G. Villanueva, and M. L. Roukes. *Fundamentals of Nanomechanical Resonators*. Springer, Cham, 2016.

[48] James Millen et al. "Optomechanics with levitated particles". In: *Reports on Progress in Physics* 83.2 (2020), p. 026401. DOI: 10.1088/1361-6633/ab6100. URL: https://doi.org/10.1088/1361-6633/ab6100.

[49] Yeghishe Tsaturyan et al. "Demonstration of suppressed phonon tunneling losses in phononic bandgap shielded membrane resonators for high-Q optomechanics". In: *Opt. Express* 22.6 (2014), pp. 6810–6821. DOI: 10.1364/OE.22.006810. URL: http://www.opticsexpress.org/abstract.cfm?URI=oe-22-6-6810.

[50] P.-L. Yu et al. "A phononic bandgap shield for high-Q membrane microresonators". In: *Applied Physics Letters* 104.2 (2014), p. 023510. DOI: 10.1063/1.4862031. eprint: https://doi.org/10.1063/1.4862031. URL: https://doi.org/10.1063/1.4862031.

[51] Gregory S. MacCabe et al. "Nano-acoustic resonator with ultralong phonon lifetime". In: *Science* 370.6518 (2020), pp. 840–843. ISSN: 0036-8075. DOI: 10.1126/science.abc7312. eprint: https://science.sciencemag.org/content/370/6518/840.full.pdf. URL: https://science.sciencemag.org/content/370/6518/840.

[52] Y. Tsaturyan et al. "Ultracoherent nanomechanical resonators via soft clamping and dissipation dilution". In: *Nature Nanotechnology* 12.8 (2017), pp. 776–783. ISSN: 1748-3395. DOI: 10.1038/nnano.2017.101. URL: https://doi.org/10.1038/nnano.2017.101.

[53] A. H. Ghadimi et al. "Elastic strain engineering for ultralow mechanical dissipation". In: *Science* 360.6390 (2018), pp. 764–768. ISSN: 0036-8075. DOI: 10.1126/science.aar6939. eprint: https://science.sciencemag.org/content/360/6390/764.full.pdf. URL: https://science.sciencemag.org/content/360/6390/764.

[54] Anders Simonsen et al. "Sensitive optomechanical transduction of electric and magnetic signals to the optical domain". In: *Opt. Express* 27.13 (2019), pp. 18561–18578. DOI: 10.1364/OE.27.018561. URL: http://www.opticsexpress.org/abstract.cfm?URI=oe-27-13-18561.

[55] A. Simonsen et al. "Magnetic resonance imaging with optical preamplification and detection". In: *Scientific Reports* 9.1 (2019), p. 18173. ISSN: 2045-2322. DOI: 10.1038/s41598-019-54200-3. URL: https://doi.org/10.1038/s41598-019-54200-3.

[56] Frank Arute et al. "Quantum supremacy using a programmable superconducting processor". In: *Nature* 574.7779 (2019), pp. 505–510. ISSN: 1476-4687. DOI: 10.1038/s41586-019-1666-5. URL: https://doi.org/10.1038/s41586-019-1666-5.

[57] E. Pednault et al. *On "Quantum Supremacy"*. IBM. 2019. URL: https://www.ibm.com/blogs/research/2019/10/on-quantum-supremacy/.

[58] T. Staudacher et al. "Nuclear Magnetic Resonance Spectroscopy on a (5-Nanometer)3 Sample Volume". In: *Science* 339.6119 (2013), pp. 561–563. ISSN: 0036-8075. DOI: 10.1126/science.1231675. eprint: https://science.

sciencemag.org/content/339/6119/561.full.pdf. URL: https://science.sciencemag.org/content/339/6119/561.

[59] H. J. Mamin et al. "Nanoscale Nuclear Magnetic Resonance with a Nitrogen-Vacancy Spin Sensor". In: *Science* 339.6119 (2013), pp. 557–560. ISSN: 0036-8075. DOI: 10.1126/science.1231540. eprint: https://science.sciencemag.org/content/339/6119/557.full.pdf. URL: https://science.sciencemag.org/content/339/6119/557.

[60] C. L. Degen et al. "Nanoscale magnetic resonance imaging". In: *Proceedings of the National Academy of Sciences* 106.5 (2009), pp. 1313–1317. ISSN: 0027-8424. DOI: 10.1073/pnas.0812068106. eprint: https://www.pnas.org/content/106/5/1313.full.pdf. URL: https://www.pnas.org/content/106/5/1313.

[61] U. Grob et al. "Magnetic Resonance Force Microscopy with a One-Dimensional Resolution of 0.9 Nanometers". In: *Nano Lett.* 19.11 (Nov. 2019), pp. 7935–7940. ISSN: 1530-6984. DOI: 10.1021/acs.nanolett.9b03048. URL: https://doi.org/10.1021/acs.nanolett.9b03048.

[62] I.M. Savukov, S.J. Seltzer, and M.V. Romalis. "Detection of NMR signals with a radio-frequency atomic magnetometer". In: *Journal of Magnetic Resonance* 185.2 (2007), pp. 214–220. ISSN: 1090-7807. DOI: https://doi.org/10.1016/j.jmr.2006.12.012. URL: https://www.sciencedirect.com/science/article/pii/S1090780706004101.

[63] I.M. Savukov et al. "MRI with an atomic magnetometer suitable for practical imaging applications". In: *Journal of Magnetic Resonance* 199.2 (2009), pp. 188–191. ISSN: 1090-7807. DOI: https://doi.org/10.1016/j.jmr.2009.04.012. URL: https://www.sciencedirect.com/science/article/pii/S1090780709001074.

[64] J. M. Taylor et al. "Laser Cooling and Optical Detection of Excitations in a LC Electrical Circuit". In: *Phys. Rev. Lett.* 107 (27 2011), p. 273601. DOI: 10.1103/PhysRevLett.107.273601. URL: https://link.aps.org/doi/10.1103/PhysRevLett.107.273601.

[65] T. Bagci et al. "Optical detection of radio waves through a nanomechanical transducer". In: *Nature* 507.7490 (2014), pp. 81–85. ISSN: 1476-4687. DOI: 10.1038/nature13029. URL: https://doi.org/10.1038/nature13029.

[66] Kazuyuki Takeda et al. "Electro-mechano-optical detection of nuclear magnetic resonance". In: *Optica* 5.2 (2018), pp. 152–158. DOI: 10.1364/OPTICA.5.000152. URL: http://www.osapublishing.org/optica/abstract.cfm?URI=optica-5-2-152.

[67] Yusuke Tominaga et al. "Studies on NMR-signal up-conversion from radio-frequency to optical regimes using a lightweight nanomembrane transducer". In: *Journal of Magnetic Resonance* 298 (2019), pp. 6–15. ISSN: 1090-7807. DOI: 10.1016/j.jmr.2018.11.003. URL: https://www.sciencedirect.com/science/article/pii/S1090780718303021.

[68] I. Moaddel Haghighi et al. "Sensitivity-Bandwidth Limit in a Multimode Optoelectromechanical Transducer". In: *Phys. Rev. Applied* 9 (3 2018), p. 034031. DOI: 10.1103/PhysRevApplied.9.034031. URL: https://link.aps.org/doi/10.1103/PhysRevApplied.9.034031.

[69] Brian M Dale, Mark A Brown, and Richard C Semelka. *MRI Basic Principles and Applications*. Wiley Blackwell, 2015.

[70] Eric R.I. Abraham and Eric A. Cornell. "Teflon feedthrough for coupling optical fibers into ultrahigh vacuum systems". In: *Appl. Opt.* 37.10 (1998), pp. 1762–1763. DOI: 10.1364/AO.37.001762. URL: http://ao.osa.org/abstract.cfm?URI=ao-37-10-1762.

[71] D. M. Pozar. *Microwave Engineering*. 3rd ed. Wiley, 2004.

[72] Joseph V. Rispoli et al. "Trap Design and Construction for High-Power Multinuclear Magnetic Resonance Experiments". eng. In: *Concepts in magnetic resonance. Part B, Magnetic resonance engineering* 46B.28529464 (Oct. 2016), pp. 162–168. ISSN: 1552-504X. DOI: 10.1002/cmr.b.21345. URL: https://www.ncbi.nlm.nih.gov/pmc/articles/PMC5436609/.

[73] Graham C. Wiggins et al. "96-Channel receive-only head coil for 3 Tesla: Design optimization and evaluation". In: *Magnetic Resonance in Medicine* 62.3 (2009), pp. 754–762. DOI: https://doi.org/10.1002/mrm.22028. eprint: https://onlinelibrary.wiley.com/doi/pdf/10.1002/mrm.22028. URL: https://onlinelibrary.wiley.com/doi/abs/10.1002/mrm.22028.

[74] T. Menke et al. "Reconfigurable re-entrant cavity for wireless coupling to an electro-optomechanical device". In: *Review of Scientific Instruments* 88.9 (2017), p. 094701. DOI:

10.1063/1.5000973. eprint: https://doi.org/10.1063/1.5000973. URL: https://doi.org/10.1063/1.5000973.

[75] V. Sudhir et al. "Quantum Correlations of Light from a Room-Temperature Mechanical Oscillator". In: *Phys. Rev. X* 7 (3 2017), p. 031055. DOI: 10.1103/PhysRevX.7.031055. URL: https://link.aps.org/doi/10.1103/PhysRevX.7.031055.

[76] Uroš Delić et al. "Cooling of a levitated nanoparticle to the motional quantum ground state". In: *Science* 367.6480 (Feb. 2020), p. 892. DOI: 10.1126/science.aba3993. URL: http://science.sciencemag.org/content/367/6480/892.abstract.

[77] Lorenzo Magrini et al. "Real-time optimal quantum control of mechanical motion at room temperature". In: (2021). arXiv: 2012.15188 [quant-ph].

[78] Jingkun Guo, Richard Norte, and Simon Gröblacher. "Feedback Cooling of a Room Temperature Mechanical Oscillator close to its Motional Ground State". In: *Phys. Rev. Lett.* 123 (22 2019), p. 223602. DOI: 10.1103/PhysRevLett.123.223602. URL: https://link.aps.org/doi/10.1103/PhysRevLett.123.223602.

[79] Chris Whittle et al. "Approaching the motional ground state of a 10-kg object". In: *Science* 372.6548 (2021), pp. 1333–1336. ISSN: 0036-8075. DOI: 10.1126/science.abh2634. eprint: https://science.sciencemag.org/content/372/6548/1333.full.pdf. URL: https://science.sciencemag.org/content/372/6548/1333.

[80] D Hunger et al. "A fiber Fabry–Perot cavity with high finesse". In: *New Journal of Physics* 12.6 (2010), p. 065038. DOI: 10.1088/1367-2630/12/6/065038. URL: https://doi.org/10.1088/1367-2630/12/6/065038.

[81] D. Hunger et al. "Laser micro-fabrication of concave, low-roughness features in silica". In: *AIP Advances* 2.1 (2012), p. 012119. DOI: 10.1063/1.3679721. eprint: https://doi.org/10.1063/1.3679721. URL: https://doi.org/10.1063/1.3679721.

[82] Yves Colombe et al. "Strong atom-field coupling for Bose-Einstein condensates in an optical cavity on a chip". In: *Nature* 450.7167 (Nov. 2007), pp. 272–276. ISSN: 1476-4687. URL: https://doi.org/10.1038/nature06331.

[83] N. E. Flowers-Jacobs et al. "Fiber-cavity-based optomechanical device". In: *Applied Physics Letters* 101.22 (2012), p. 221109. DOI: 10.1063/1.4768779. eprint: https://doi.org/10.1063/1.4768779. URL: https://doi.org/10.1063/1.4768779.

[84] S. Stapfner et al. "Cavity-enhanced optical detection of carbon nanotube Brownian motion". In: *Applied Physics Letters* 102.15 (2013), p. 151910. DOI: 10.1063/1.4802746. eprint: https://doi.org/10.1063/1.4802746. URL: https://doi.org/10.1063/1.4802746.

[85] Ivan Favero et al. "Fluctuating nanomechanical system in a high finesse optical microcavity". In: *Opt. Express* 17.15 (2009), pp. 12813–12820. DOI: 10.1364/OE.17.012813. URL: http://www.opticsexpress.org/abstract.cfm?URI=oe-17-15-12813.

[86] A D Kashkanova et al. "Optomechanics in superfluid helium coupled to a fiber-based cavity". In: *Journal of Optics* 19.3 (2017), p. 034001. DOI: 10.1088/2040-8986/aa551e. URL: https://doi.org/10.1088/2040-8986/aa551e.

[87] Konstantin Ott et al. "Millimeter-long fiber Fabry-Perot cavities". In: *Opt. Express* 24.9 (2016), pp. 9839–9853. DOI: 10.1364/OE.24.009839. URL: http://www.opticsexpress.org/abstract.cfm?URI=oe-24-9-9839.

[88] Yeghishe Tsaturyan. "Ultracoherent soft-clamped mechanical resonators for quantum cavity optomechanics". PhD thesis. University of Copenhagen, 2019.

[89] M. L. Gorodetksy et al. "Determination of the vacuum optomechanical coupling rate using frequency noise calibration". In: *Opt. Express* 18.22 (2010), pp. 23236–23246. DOI: 10.1364/OE.18.023236. URL: http://www.osapublishing.org/oe/abstract.cfm?URI=oe-18-22-23236.

[90] Werner Heisenberg. *The physical principles of the quantum theory*. Dover publications, 1950.

[91] Stefano Mancini, David Vitali, and Paolo Tombesi. "Optomechanical Cooling of a Macroscopic Oscillator by Homodyne Feedback". In: *Phys. Rev. Lett.* 80 (4 1998), pp. 688–691. DOI: 10.1103/PhysRevLett.80.688. URL: https://link.aps.org/doi/10.1103/PhysRevLett.80.688.

[92] P. F. Cohadon, A. Heidmann, and M. Pinard. "Cooling of a Mirror by Radiation Pressure". In: *Phys. Rev. Lett.* 83 (16 1999), pp. 3174–3177. DOI: 10.1103/PhysRevLett.83.3174. URL: https://link.aps.org/doi/10.1103/PhysRevLett.83.3174.

[93] A. Kubanek et al. "Photon-by-photon feedback control of a single-atom trajectory". In: *Nature* 462.7275 (2009), pp. 898–901. ISSN: 1476-4687. DOI: 10.1038/nature08563. URL: https://doi.org/10.1038/nature08563.

[94] Pavel Bushev et al. "Feedback Cooling of a Single Trapped Ion". In: *Phys. Rev. Lett.* 96 (4 2006), p. 043003. DOI: 10.1103/PhysRevLett.96.043003. URL: https://link.aps.org/doi/10.1103/PhysRevLett.96.043003.

[95] Vijay Jain et al. "Direct Measurement of Photon Recoil from a Levitated Nanoparticle". In: *Phys. Rev. Lett.* 116 (24 2016), p. 243601. DOI: 10.1103/PhysRevLett.116.243601. URL: https://link.aps.org/doi/10.1103/PhysRevLett.116.243601.

[96] Dustin Kleckner and Dirk Bouwmeester. "Sub-kelvin optical cooling of a micromechanical resonator". In: *Nature* 444.7115 (2006), pp. 75–78. ISSN: 1476-4687. DOI: 10.1038/nature05231. URL: https://doi.org/10.1038/nature05231.

[97] M. Poggio et al. "Feedback Cooling of a Cantilever's Fundamental Mode below 5 mK". In: *Phys. Rev. Lett.* 99 (1 2007), p. 017201. DOI: 10.1103/PhysRevLett.99.017201. URL: https://link.aps.org/doi/10.1103/PhysRevLett.99.017201.

[98] B Abbott et al. "Observation of a kilogram-scale oscillator near its quantum ground state". In: *New Journal of Physics* 11.7 (2009), p. 073032. DOI: 10.1088/1367-2630/11/7/073032. URL: https://doi.org/10.1088/1367-2630/11/7/073032.

[99] L. Neuhaus et al. "PyRPL (Python Red Pitaya Lockbox) — An open-source software package for FPGA-controlled quantum optics experiments". In: *2017 Conference on Lasers and Electro-Optics Europe European Quantum Electronics Conference (CLEO/Europe-EQEC)*. 2017, pp. 1–1. DOI: 10.1109/CLEOE-EQEC.2017.8087380.

[100] David Hälg et al. "Membrane-Based Scanning Force Microscopy". In: *Phys. Rev. Applied* 15 (2 2021), p. L021001. DOI: 10.1103/PhysRevApplied.15.L021001. URL: https://link.aps.org/doi/10.1103/PhysRevApplied.15.L021001.

[101] Eric D. Black. "An introduction to Pound-Drever-Hall laser frequency stabilization". In: *American Journal of Physics* 69.1 (Dec. 2000), pp. 79–87. ISSN: 0002-9505. DOI: 10.1119/1.1286663. URL: https://doi.org/10.1119/1.1286663.

[102] A. Kashkanova. "Optomechanics with Superfluid Helium". PhD thesis. Yale University, 2017.

[103] J. Gallego et al. "High-finesse fiber Fabry-Perot cavities: stabilization and mode matching analysis". In: *Applied Physics B* 122.3 (2016), p. 47. ISSN: 1432-0649. DOI: 10.1007/s00340-015-6281-z. URL: https://doi.org/10.1007/s00340-015-6281-z.

[104] Felix Rochau et al. "Dynamical Backaction in an Ultrahigh-Finesse Fiber-Based Microcavity". In: *Phys. Rev. Applied* 16 (1 2021), p. 014013. DOI: 10.1103/PhysRevApplied.16.014013. URL: https://link.aps.org/doi/10.1103/PhysRevApplied.16.014013.